Laser Ablation-Inductively Coupled Plasma-Mass Spectrometry Imaging in Biology

Philip A. Doble,[1*] Raquel Gonzalez de Vega,[1] David P. Bishop,[1] Dominic J. Hare[1,2] and David Clases[1]

[1] Atomic Medicine Initiative, University of Technology Sydney, Broadway, New South Wales 2007, Australia

[2] School of BioSciences, University of Melbourne, Parkville, Victoria 3052, Australia

[*] philip.doble@uts.edu.au

ABSTRACT

Elemental imaging gives insight into the fundamental chemical makeup of living organisms. Every cell on Earth is comprised of a complex and dynamic mixture of the chemical elements that define structure and function. Many disease states feature a disturbance in elemental homeostasis and understanding how, and most importantly where, has driven the development of laser ablation-inductively coupled plasma-mass spectrometry (LA-ICP-MS) as the principal elemental imaging technique for biologists. This review provides an outline of ICP-MS technology, laser ablation cell designs, imaging workflows and methods of quantification. Detailed examples of imaging applications including analyses of cancers, elemental uptake and accumulation, plant bioimaging, nanomaterials in the environment, exposure science and neuroscience are presented and discussed. Recent incorporation of immunohistochemical workflows for imaging biomolecules, complementary and multimodal imaging techniques and image processing methods are also reviewed.

CONTENTS

Abbreviations and acronyms

6-OHDA	6-hydroxydopamine
Ab	antibody
AD	Alzheimer's disease
AES	atomic emission spectroscopy
ALS	amyotrophic lateral sclerosis
Aβ	amyloid
BSA	bovine serum albumin
CRC	collision/reaction cell
CRM	certified reference material
CSV	cell surface vimentin
CT	computed tomography
CZE	capillary zone electrophoresis
DA	dopamine
DAB	3,3'-diaminobenzidine
DC	direct current
DCI	dual concentric injector
DCIS	ductal carcinoma in-situ
DESI	desorption electrospray ionization
DMD	Duchenne muscular dystrophy
DMSA	meso-2,3-dimercaptosuccinic acid
DOTA	1,4,7,10-tetraazacyclododecane-1,4,7,10-tetraacetic acid
DTTA	diethylenetriaminetetraacetic acid
ECD	extracellular domain
EDX	energy-dispersive X-ray
ESA	electrostatic analyzer
FFPE	formalin-fixed paraffin-embedded
FISH	fluorescence *in situ* hybridization
FPN	ferroportin
FWHM	full width at half maximum
H&E	hematoxylin and eosin
HIPEC	heated intraoperative chemotherapy
ICP-MS	inductively coupled plasma-mass spectrometry
ID	isotope dilution
IF	immunofluorescence
IHC	immunohistochemistry
IMC	imaging mass cytometry
ICP	inductively coupled plasma
IS	internal standard
ISH	*in situ* hybridization
KED	kinetic energy discrimination
L-2-tellurienylalanine	TePhe
LA-ICP-MS	laser ablation-inductively coupled plasma-mass spectrometry
LC	liquid chromatography
LIBS	laser-induced plasma spectroscopy
LOD	limit of detection
MALDI	matrix-assisted laser desorption/ionization
m/z	mass-to-charge
MC	multi-collector

MeCAT	metal coded affinity tag
MFH	magnetic fluid hyperthermia
MIP	microwave induced plasma
MMP-11	matrix metalloproteinase 11
MPTP	1-methyl-4-phenyl-1,2,3,6-tetrahydropyridine
Mregs	regulatory macrophages
MRI	magnetic resonance imaging
MRS	magnetic particle spectroscopy
MS	multiple sclerosis
MS/MS	triple quadrupole or tandem mass spectrometry
MSI	mass spectrometry imaging
MT	metallothionein
MT1-MMP	membrane type-1 matrix metalloproteinase
NP	nanoparticle
OCT	organic cation transporter
PCA	principal component analysis
PD	Parkinson's disease
PET	positron emission tomography
PFA	paraformaldehyde
PIXE	proton-induced X-ray emission
PMMA	polymethylmethacrylate
PTFE	polytetrafluoroethylene
Q	quadrupole
QMS	quadrupole mass spectrometry
RF	radio frequency
ROS	reactive oxygen species
RT	room temperature
SDS-PAGE	sodium dodecyl sulphate–polyacrylamide gel electrophoresis
SEMs	secondary electron multipliers
SF	sector-field
SIMS	secondary-ion mass spectrometry
SNc	substantia nigra pars compacta
SNr	substantia nigra pars reticulata
SOD	superoxide dismutase
SP	single particle
SPADE	spanning-tree progression analysis
T1D	type 1 diabetes
TEM	transmission electron microscopy
TH	tyrosine hydroxylase
TOF	time of flight
XRF	x-ray fluorescence

1. INTRODUCTION

Laser ablation-inductively coupled plasma-mass spectrometry (LA-ICP-MS) imaging employs a high-energy laser beam to sample a biological specimen prior to introduction to an ICP-MS. The high temperature plasma atomizes and ionizes the sample's constituent elements from which high-resolution maps may be constructed by traversing the laser beam across the sample section. LA-ICP-MS imaging has numerous applications in diverse areas of investigation such as neuroscience, environmental exposure to toxic elements, and basic mechanistic biology, and is a platform technology in the field of Metallomics, which may be defined as the study of the metallome. The definition of the metallome is still under debate and consists of various chemical entities such metalloproteins, investigations of metal-based drugs, and perhaps incorporation of essential inorganic elements such as selenium, phosphorus or iodine, amongst others.[1] Bioinorganic analyses are no longer the sole focus of application as incorporation of immunohistochemical workflows has extended LA-ICP-MS imaging to the investigation of biomolecules by employing metal-tagged antibodies. LA-ICP-MS applications have been driven by development of technology and innovative methods that probe the microchemical environment of biological matrices to investigate the complex interplay of metals, enzymes, proteins, and other elements and molecules in biological processes within relatively large anatomical structures, and more recently, at cellular and sub-cellular levels.

The first bio-images were constructed by Wang *et al.*[2] in their often-overlooked study in 1994 (Figure 1A). Here, an Nd:YAG laser coupled to a quadrupole ICP-MS was used to construct images of fish scales, rat kidney cross sections and a pig femur. This was followed by Feldmann *et al.*[3] in 2002, where a series of fresh wet animal organs were directly analyzed via laser line scanning for various elements using an in-house designed cryogenically cooled laser ablation cell. The authors demonstrated LA-ICP-MS produced highly sensitive and repeatable quantification of elements in soft tissues. Kindness *et al.*[4] expanded this line scanning concept in 2003 to construct an elemental contour map of sheep liver (Figure 1B).

In the quarter century since Wang's report, where images were constructed with a spatial resolution of 30 μm that is still commonly described today, LA-ICP-MS imaging has rapidly

grown in capability and uptake in the biological sciences. This review discusses the rise of LA-ICP-MS imaging specifically in biology and is designed to present to the reader a comprehensive overview of technological innovations in instrumentation and applications. The review begins with detailed discussions of ICP-MS instrumentation, covering the history of the technology and compares various configurations including time of flight, quadrupole, sector field and tandem mass spectrometers. A brief history of laser ablation cell development then follows, beginning with rudimentary early designs right through to modern commercial offerings that have been optimized for imaging applications. Imaging workflows are then presented covering important topics such as experimental design, considerations of imaging parameters, and methods of quantification. Applications of LA-ICP-MS imaging are reviewed encompassing diverse areas of study. These include imaging animal models and human cancers for novel biomarker discovery, drug penetration studies, and elucidation of basic elemental homeostasis. Uptake and accumulation of elements to investigate the interaction of natural and anthropogenic pollutants within organisms, plant bioimaging, nanomaterials in the environment, exposure science and neuroscience are also covered. Approaches for biomolecular imaging via incorporation of immunohistochemical labelling techniques are then presented, followed by examination of image processing methods for anatomical segmentation, feature selection and three-dimensional reconstructions. Complementary bio-imaging techniques suitable for multimodal imaging are also reviewed and a projection of the likely future of the technology discussed.

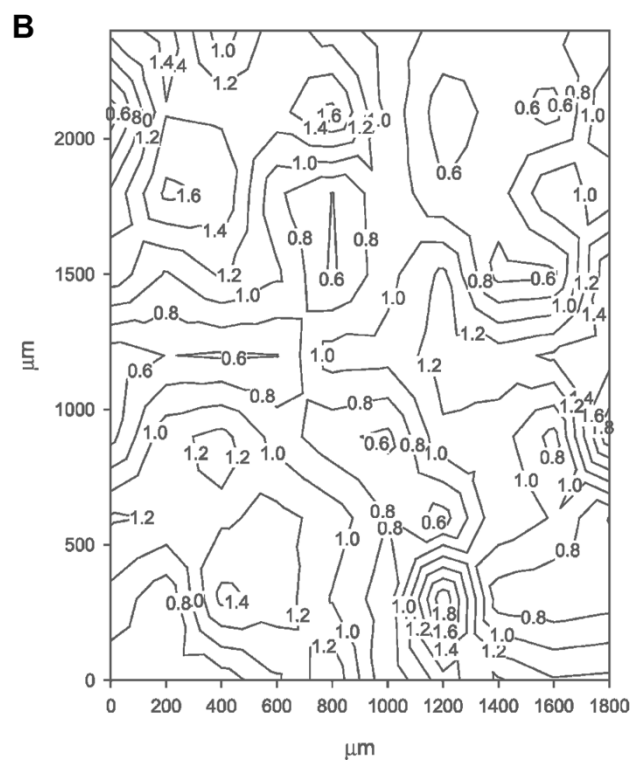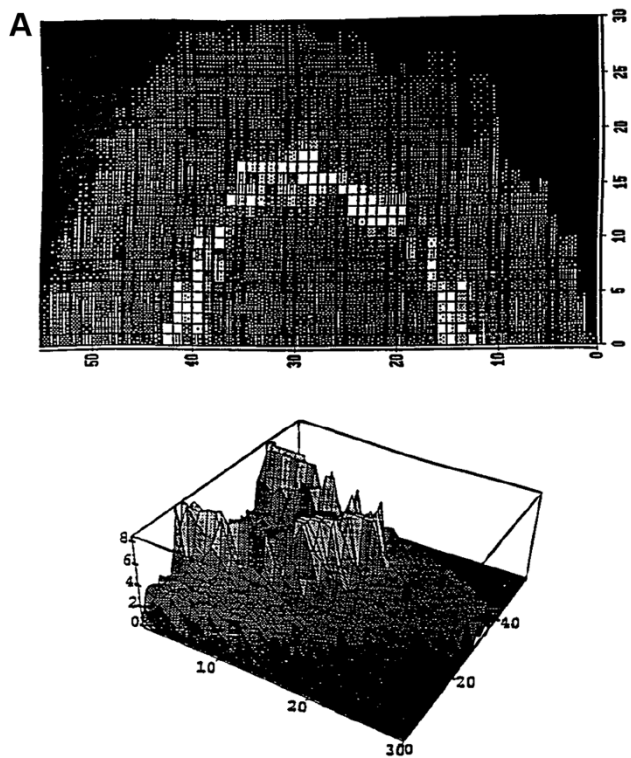**Figure 1:** First bio images produced using LA-ICP-MS. A) 88Sr/48Ca ratio images in fish scale. Reproduced with permission from Ref.[2]. Copyright 1994 SAGE Publications. B) Topography-style quantitative map of Cu distribution in a sheep liver section. Reproduced with permission from Ref.[4]. Copyright 2003 Oxford University Press.

2.   INDUCTIVELY COUPLED PLASMA-MASS SPECTROMERTY

2.1.   A Brief History of Inductively Coupled Plasma – Mass Spectrometry (ICP-MS)

Technological advances have driven gradual performance improvements of ICP-MS over the last four decades. Introduction of technologies such as the collision/reaction cell (CRC), sector field, tandem and time of flight mass spectrometers, rapid detection systems and enhanced statistical algorithms provide dedicated multi-elemental detection for most elements of the periodic table with large dynamic ranges, robustness and high sensitivity. The ICP was commercially introduced in the early 1970s after Greenfield *et al.*[5] and Wendt and Fassel[6] examined ICP as a source for atomic emission spectroscopy, which was rapidly adopted by research laboratories.[7-9] After initial experiments on arc discharge plasmas and its potential as ion sources for mass spectrometry by Gray,[10, 11] high temperature ICP and microwave induced plasma (MIP) ion sources of approximately 6000 K were proposed for mass spectrometry using a quadrupole mass analyzer for the analysis of aerosols generated via solution nebulization or laser ablation (British Patent 1371 104, 1971). In 1980 Houk *et al.* proposed a comprehensive framework for ICP-MS for trace element analysis,[12] followed by the commercialization of two ICP-MS platforms in 1983 (Perkin-Elmer SCIEX: ELAN 250 at Pitcon 1983) and 1984 (VG Instruments: VG Plasma Quad at Pitcon 1984).[13, 14] Over the following years, ICP-MS matured to become the method of choice for trace element analysis across multiple disciplines and kept pace with important technological and method development milestones.[15]

The hard ionization source of the Ar plasma annihilates all molecular information, obscuring the "molecular history" of the targeted analytes. While this can be exploited, for example, for species independent quantification strategies, it complicates speciation analyses and the investigation of elemental distributions.[16] Hyphenation with separation techniques such as liquid chromatography (LC) or discrete sampling of solids by laser ablation conserves retention time or spatial information as species-specific parameters. These techniques provided new perspectives on the role of metals, metalloids, and other inorganic species in biological systems. ICP-MS and associated hyphenated techniques operate at the interdisciplinary interface of several scientific fields including medicine, nanotechnology,

environmental and life sciences in both research and for routine analyses.[15, 16] As one of the most versatile element-specific detection systems, ICP-MS underpins investigations of "metallomics as an integrated biometal science" introduced by Haraguchi in 2003.[17] This technology has transformed our understanding of the role of trace and minor elements and their species in biological systems. Even after four decades, new applications and instrumental advances are frequently reported, continually expanding the scope of ICP-MS. As of 2020, some 20 vendors offer commercial platforms with different sample interface configurations and detection modalities.

An ICP as ion source design has high ionization efficiencies and initial designs have not been significantly modified despite the large choice of commercial offerings. Most commonly, ICPs are generated in torches with a Fassel design consisting of three concentric glass tubes with distinct Ar gas flows required for cooling, sustaining the plasma, aerosol transport and plasma injection. The torch may be grounded with a Pt shield to mitigate the deterioration of the interface and to counteract the "pinch effect" which can cause kinetic energy broadening, secondary discharges and the generation of ions with multiple charges.[18] Several high energy radio frequency (RF) generator/coil designs allow impedance matching and high-power transfer efficiency for robust elemental analysis in complex matrices. As such, stable RF powered magnetic fields at either 27 or 40 MHz accelerate electrons to kinetic energies where Ar atoms are ionized (15.67 eV) via electron impact.[19] Target analytes are ionized with the same mechanism, or via charge transfer or penning ionization with Ar ions/atoms. The ionization efficiency depends on the plasma temperature, ion density and the first ionization potential of the targeted element and can be calculated by solving the Saha ionization equation.[20] For most elements the ionization degree is above 90%.[18]

After ionization, positively charged ions are extracted into a high vacuum region. The sensitivity in ICP-MS is dependent on low pressures which increase the mean free path of analytes to support ion transmission. The most common arrangement involves the operation of a multi-staged vacuum interface where the extracted ion beam is shaped by sampler and skimmer cones and transported stepwise from ambient pressures into a high vacuum region.[21] The adiabatic expansion into the vacuum induces mass discrimination due to mass dependent diffusion coefficients. This nozzle effect results in higher ion transmissions for

heavy masses.[22] A similar phenomenon occurs from space charge effects, where coulomb repulsion centers heavy masses in the ion beam and increasingly eliminates low mass ions.[23] After extraction, the ion beam is directed along a curved path to eliminate neutral particles and photons before ions are transported to the mass analyzer, where they are separated according to their mass-to-charge (m/z) ratios.[24] For the detection of ionized masses, secondary electron multiplier and Faraday cups are frequently employed for a large linear dynamic range of up to 12 orders of magnitude and offer detections rates of up to several kHz. Modern instruments operate a dual-stage electron multiplier in which signals can be detected via pulse counting or monitored in an analogue mode when exceeding a certain threshold. For trace analyses, detectors operate in a pulse counting mode for maximum signal amplification. It is also necessary to consider that during the signal amplification, detectors are blind (dead time approx. 20-40 ns) which can impact the analysis (e.g., isotope ratio measurements) but can be compensated by software or manually if counting rates are sufficiently high.[25]

Three major classes of mass analyzers are currently employed in ICP-MS: quadrupole, sector-field, and time-of-flight. The quadrupole-(Q) based analyzer was the first used for ICP-MS and is the workhorse in industry and research due to its low cost of purchase and maintenance, as well as robust operation. This is particularly clear when comparing the number of peer-reviewed articles operating ICP-MS by detector type; ICP-QMS systems have produced around 10 times the research output of sector-field (SF), time of flight (TOF) and triple quadrupole (MS/MS) mass analyzers. Today, 85% of ICP-MS studies employ a single quadrupole mass analyzer design and only 15% comprise of TOF, SF or tandem mass spectrometry.

The CRC was developed in the late 1990s and allowed single quadrupole mass analyzers to be used for applications where polyatomic interferences previously rendered them unsuitable. This new technology may use various gases and acquisition modes to remove interfering species by chemical reactions and/or kinetic energy discrimination (KED).[26] The introduction of ICP-MS/MS in 2012 improved mitigation of polyatomic interferences and set a new benchmark by reducing the background noise for elements traditionally difficult for ICP-QMS.[27, 28]

While the CRC and tandem mass spectrometry for ICP-MS improved the "chemical resolution", SF-based instruments improved the mass resolution and were developed in the early 90s.[29] SF systems offer adjustable resolutions (m/Δm) of up to approximately 10,000 (10% signal height) and improved sensitivity and precision. In certain geometries SF-based instruments allow the simultaneous acquisition of several isotopes from a selected mass range monitored with multiple detectors in multi-collector (MC) systems.[30] This rapid and simultaneous acquisition of several masses accelerated the investigation of TOF technology for ICP-MS. Originally developed in the 90s,[31] its potential was harnessed within the past decade and is emerging as promising alternative for LA-ICP-QMS. TOF technology also underpins the growing interest in mass cytometry.[32]

LA-ICP-MS imaging is commonly performed either by continuous scanning or single shot analysis. The most applied method is continuous scanning where the laser is fired at a high repetition rate and the generated aerosol from separate shots are mixed producing a continuous sample stream into the ICP. While this provides higher sensitivity due to higher mass flows, it also limits spatial resolution and consequently image quality, which can partially be corrected using mathematical tools.[33] However, advances in ablation cell design and the development of rapid mass analyzers offering high scanning speeds and multielement detection, moved single shot analysis into greater focus to increase sample throughput and image resolution.[34]

Q, SF and TOF-based LA-ICP-MS platforms each have relative advantages and disadvantages and offer complementary acquisition modes pertinent to various facets of elemental imaging. In the following sections, specific features of these mass analyzers and important examples are discussed with a focus on their impact on LA-ICP-MS imaging and its application in life sciences.

2.2. Quadrupole mass analyzers and collision/reaction cells in LA-ICP-MS

The overwhelming popularity of ICP-QMS can be explained by its simplicity, robustness, and cost-effectiveness. However, there are relative strengths and limitations of ICP-QMS and its

application with laser ablation systems for accurate and precise analyses and for construction of high-quality images. Several factors including shot frequency, dwell time, matrix, sensitivity, spatial and mass resolution, peak measurement protocol, scan speed and spectral interferences can affect the figures of merit and must be considered when designing experiments. The selection of these parameters requires a basic understanding of the operation principle of quadrupole mass spectrometry and how it may be optimized in conjunction with a LA system.

A quadrupole consists of four parallel metal rods and applies distinct combinations of RF and direct current (DC) voltages that filter specific m/z values. Each m/z follows an individual ion trajectory which may be calculated by solving the Mathieu equations.[35] Common to all ICP-QMS instruments, combinations of RF and DC voltages are altered linearly (scan line), and only one combination of RF and DC voltage for each m/z is applied to sequentially measure isotopes of interest via a time resolved "peak hopping" protocol. The set of RF and DC voltages (the equation of the scanning line) specifies the mass resolution and ion transmission for each m/z.[36] In 1996 Niu and Houk examined the fundamentals of ion extraction and transport for different mass analyzers and reported that ion transmission in ICP-QMS was only 0.002-0.0002% of generated ions.[21] In the last two decades, the design of the ICP-QMS has been modified to improve the ion path geometry and vacuum levels to enhance ion transmission and reduce backgrounds, leading to an increase of sensitivity by three orders of magnitude.[37, 38] Clases et al. recently demonstrated the feasibility of operation of the quadrupole with an increased mass band pass mode to improve ion transmission in both hyphenated ICP-MS including LA-ICP-MS.[39] [36, 40] Here, the scan line slope was modified to increase ion transmission at the expense of resolution, to improve limits of detection or to increase spatial resolution (**Figure 2**). However, quadrupoles are usually operated at a fixed (unit) mass resolution to maintain selectivity.
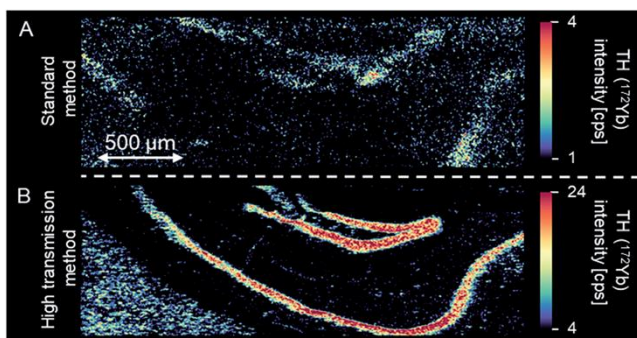
Figure 2: The hippocampal structure was targeted in two consecutive sections of murine brain employing (A); standard method and (B); the high transmission method. Reproduced with permission from Ref. [36]. Copyright 2020 Royal Society of Chemistry.

The lateral resolution of an image and the limit of detection (LOD) are dependent on the number of monitored masses, the dwell time, and the sweep and settling time of the quadrupole. Lear *et al.* investigated signal to noise ratios at various dwell times and concluded that optimal spatial resolution, LODs and scanning speed required a compromise, and in general the scan speed may be maintained at approximately 4 to 5 times the magnitude of the spot size without significant loss of detection sensitivity.[41] Hattendorf *et al.*[42] investigated potential implications for quantitative elemental imaging when pairing low aerosol dispersion cells with multi-isotope analyses and LA-ICP-QMS. Experiments and simulations demonstrated that if wash-out times and quadrupole scanning were situated on a similar timescale, aliasing errors became more pronounced. The authors used signal intensity averaging to eliminate systematic biases and to improve accuracy in quantitative LA-ICP-QMS experiments. Van Elteren *et al.* considered shot frequency, cell wash-out time, and quadrupole synchronization and subsequent image artefacts in high resolution images. The authors demonstrated that desynchronization of dwell time and laser shot frequency may result in significant striations that are clearly visible and not related to plasma fluctuations or Poisson noise.[43] The same authors further investigated beam size, scanning speed, surface/depth concentration, sensitivity, and reproducibility on image quality and possible artefact generation for single and multiple shot analyses.[44] In a follow-up study, they discussed the fine tuning of system wide parameters for high-speed and high-resolution imaging and developed a mathematical model for selection of instrumental conditions to minimize image blur and aliasing while optimizing the signal to noise ratios. The model is integrated in an open-source web-app for newcomers in LA-ICP-MS imaging.[45]

Recent advancements in low-dispersion cells and quadrupole acquisition speed promise potential for rapid acquisition via single shot analysis, yet compared to simultaneously operating mass analyzers, quadrupoles have only partial applicability for fast acquisition due to sequential m/z scanning and limitations in dwell and scanning time. For example, the minimum dwell times for modern quadrupoles typically range below from 0.1 to 1 ms.[34, 44, 46-48]

An area of growth for fast quadrupole acquisition is imaging of nanoparticles (NPs) in biological tissues. NPs are attracting increasing interest in industry and medicine but are also raising concerns due to negative or unknown environmental impacts. Therefore, it is likely that LA-ICP-QMS will be increasingly employed to investigate the function, location, and fate of nanomaterials. Operating LA-ICP-QMS with short integration times in single particle mode allows detection of individual particles for size calibrations and particle counting. Metarapi *et al.*[49] investigated the location and size of AuNPs in plants (**Figure 3**) and differentiated between ionic and particulate Au.
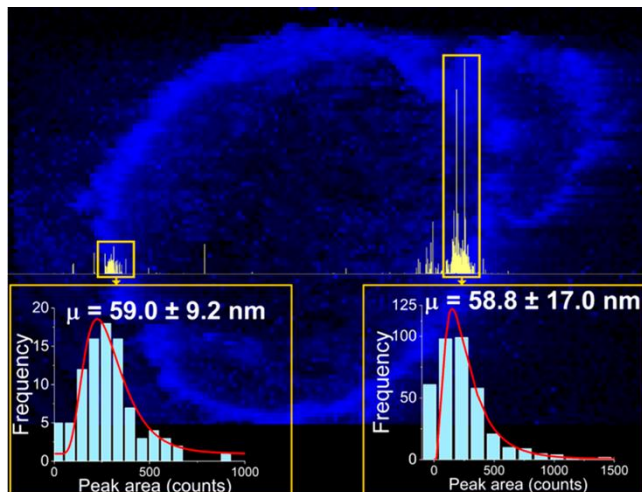
Figure 3: Image of gold distribution in cross section of sunflower grown in a controlled environment with line scan signals recorded every 100 μs. Reproduced from Ref.[49]. Copyright 2019 American Chemical Society.

One significant limitation in LA-ICP-QMS are spectral interferences which disproportionately affect elements in the low and mid mass range, mostly due to argon, carbon, nitrogen, and oxygen-based polyatomic interferences which overlap with most biologically relevant

elements, with few free of some degree of polyatomic interference. Oxygen-derived species are less pronounced in LA-ICP-QMS, where dry plasmas predominantly eliminate water as an oxygen source,[50] though trace amounts of O in Ar may adversely impact LODs.[51] Interferences can partially be mitigated using gas additives to change chemical and physical processes in the plasma. Specifically, N_2 reduces ArO-based interferences and increases sensitivity.[52-54] Alternatively, plasmas can be operated at cool and dry conditions, where the ICP is operated at low RF power and higher nebulizer gas flows.[55, 56] However, the most important method of mitigation of interferences is the CRC.[26, 57] The CRC is a RF-only multipole that is situated directly before the quadrupole and reduces interferences by KED, molecular fragmentation, charge transfer, or chemical reactions to enhance selectivity for increased signal to noise ratios. While the terms collision and reaction are often used interchangeably, reaction cells typically involve a chemical reaction to remove or shift the mass of polyatomic compounds or analytes, and collision cells involve a physical process. For example, in KED, collisions with an inert cell gas cause polyatomic ions with larger cross-sectional areas to lose kinetic energy at a greater rate than single analyte ions due to a higher number of collisions.[58] An electrostatic field can be tuned to eliminate ions with kinetic energies below a threshold to selectively analyze target m/z.[59] He and H_2 are the most common cell gases used for KED to improve the analysis of traditionally difficult elements such as Fe, Cu, Ca, Mn and Zn.[51, 60, 61] The reader can find discussion of several parameters that affect the tuning of KED in a comprehensive model by Yamada[58] and the tutorial review by Tanner *et al.*[26]

Alternatively, the CRC may be filled with various reactive gases for interference attenuation[62, 63] and reactions can be roughly categorized by charge transfer, oxidation, reduction and adduct formation.[64] NH_3, H_2 and O_2 are popular gases for a range of reactions with differing mitigation efficiencies depending on the ionization potentials and chemical affinities of the analytes. It is difficult to predict all factors that induce certain reactions and therefore, CRCs are commonly tuned empirically. In stand-alone ICP-MS, it is relatively straight forward to switch between different acquisition modes and CRC tune settings, however, in LA-ICP-MS sampling occurs too rapidly and requires the CRC to be operated statically. This requires a compromise for sufficient interference attenuation for some elements whilst maintaining sensitivity for others. Wehe *et al.*[65] discussed the feasibility of cell mode switching between individual laser scan lines, or alternatively using a simultaneous LA-split flow coupled to two

ICP-MS instruments (**Figure 4**). The former involved alternative ablation lines on a sample with different tune settings and compensation of skew errors by linear interpolation. However, this latter spilt flow approach required the laser beam spot size to be reduced by half to maintain the lateral resolution, decreasing sensitivity by a factor of four. This, coupled with the requirement for two ICP-MS instruments, renders the method unviable for most laboratories.
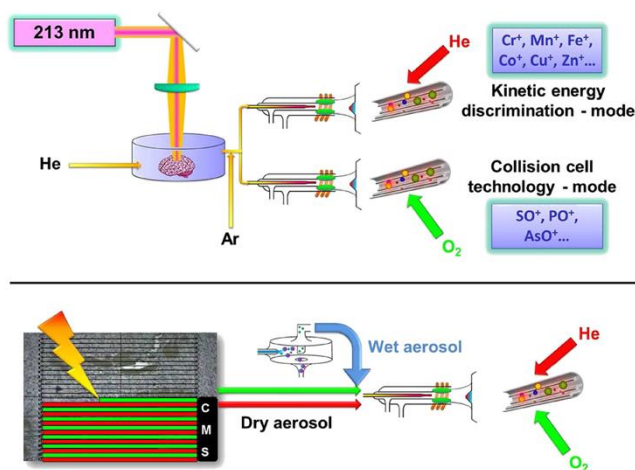

Figure 4: Parallel KED and reaction gas (top) and cell mode switching (bottom) for removal of polyatomic interferences from LA line scans. Reproduced with permission from Ref. [65]. Copyright 2014 Wiley VCH Verlag GmbH & Co. KGaA.

The selectivity of ICP-MS was further improved by the commercial introduction of tandem mass spectrometry (ICP-MS/MS) in 2012 which featured the operation of one additional quadrupole that is positioned before the CRC. Offered by three vendors, this technology can be operated in single quadrupole (SQ) or MS/MS modes. In all cases, the CRC (Q2) functions as a RF-only filter to provide conventional CRC acquisition modes. In SQ mode, the first quadrupole (Q1) (before the CRC) is operated with a larger mass bandpass and the third quadrupole (Q3) at unit mass resolution. The mass bandwidth of Q1 may be manipulated for optimization of analyte transmission and background interferences.[66] In MS/MS mode, both Q1 and Q3 are usually maintained at unit mass resolution. Like ICP-SQMS with a CRC, ICP-MS/MS allows KED and dedicated reactions.[67] However, the additional quadrupole before the CRC limits the transmission of interfering isotopes avoiding undesired reactions, non-spectral interferences, and higher reaction efficiencies.[28]

The first study on ICP-MS/MS for elemental bioimaging was published in 2016 by Bishop *et al.*, who investigated various CRC settings and compared SQ and MS/MS modes. ZN, Se and P were analyzed both on-mass and with a mass shift to investigate elemental distributions in prostate cancer in a murine brain.[66] Clases *et al.* showed that LA-ICP-MS/MS improved the imaging of Gd in biological tissues and were able to correlate the abundances of Gd, Ca and P in skin and brain tissue using oxygen as collision/reaction gas.[36] Tandem mass spectrometry also improved imaging of Fe in soft tissues,[68-70] and Ca and P in bone tissue,[71] and S, Fe, P, La and Gd in human tissues.[72] Thyssen *et al.* analyzed Na, Mg, P, K, Ca, Fe, Cu, Zn and Pb in cocoa beans using LA-ICP-MS/MS, while analyzing P, Ca and Fe with an oxygen mass shift.[73]

2.3. Sector Field and Multi-Collector LA-ICP-MS

An alternative approach to eliminate spectral interferences is to increase mass resolution. Double-focusing magnetic SF-based ICP-MS platforms can operate at three different mass resolutions (low resolution 300, medium resolution 4000, high resolution 10000 m/Δm at 10% signal height) which may resolve polyatomic interferences from the analyte m/z.[74-76] Due to more efficient ion extraction increasing transmission, SF-based instruments equipped with secondary electron multipliers (SEMs) also provide significantly higher sensitivities (up to two orders of magnitude) improving signal to noise ratios and LA imaging performance.[77,30] Interestingly, LA-ICP-SFMS for bioimaging is mainly used for its high sensitivity,[78] rather than the possibility to increase mass resolution. This is most likely related to multi-element analyses and increasing mass resolution compromising the figures of merit for non-interfered elements. Furthermore, in low resolution, the flat top mass peaks increase signal precision and significantly improves isotope ratio analysis compared to quadrupole-based ICP-MS systems.[79] Pisonero *et al.*[80] critically evaluated the potential of a nanosecond LA-ICP-SFMS system to determine elemental distributions within mouse embryonic fibroblast cells (NIH/3T3) and human cervical carcinoma cells (HeLa cells), incubated with gold nanoparticles and Cd-based quantum dots. The authors demonstrated that the system was suitable to measure Au and Cd at a resolution of approximately 2.5 μm (laser spot size) in the cytosol and

nucleus of both cell lines and obtained images that were concordant with those of confocal microscopy.

ICP-SFMS instruments are available in various geometries which offer specific advantages regarding sensitivity and signal acquisition and can be distinguished by the position of the electrostatic analyzer (ESA), the magnetic sector, and by the focal points of ion trajectories. The ESA provides rapid scanning by modifying kinetic energies of the ion beam to analyze a mass window of about 20 amu. Analytes beyond this window require a scan of the magnetic sector, which takes significant time due to hysteresis effects, and is not optimal for rapid sampling as occurs in LA-imaging. Waentig et al.[81] performed LA-ICP-SFMS of elements with large mass differences and recommended sorting elements in two groups for which a magnetic scan was not required. After each line, a magnetic scan was performed to switch between the two groups periodically.

In the Nier Johnson geometry and the Mattauch-Herzog configuration, the magnet is located after the ESA and is operated at a fixed magnetic field strength. For the latter, the ESA and magnetic sector are configured at specific angles that separate the focal points of different m/z which are measured using multiple (multi) collectors/detectors (MC). The number of detectors as well as the mass bandwidth of the magnetic sector are usually limited which restricts the number of isotopes that may be analyzed simultaneously. However, instruments based on spatially resolving semiconductor detectors allow acquisition of the entire mass range (m/z 6-238) and offer an interesting alternative for multielement, high resolution and sensitive LA imaging.[82]

The operation of LA-MC-ICP-MS opened further options for isotope ratio bioimaging. The installation of several detectors after the magnetic sector spatially separates detection of various m/z for simultaneous isotope acquisition. As such, plasma fluctuations, concentration or matrix effects do not have deleterious consequences for the determination of isotope ratios and improved precisions of 0.01-0.05% are possible.[83] The high sensitivity and excellent precision of MC-ICP-MS instruments allow the targeting of isotope ratios as biological markers, especially relevant for imaging of trace elements.[83] As noted in a perspective on isotope ratio analysis in biological tissues by LA-ICP-MS by Urgast and Feldmann in 2013,[84]

this feature of LA-ICP-MS appears extremely attractive for life sciences but is under exploited. High precision analyses allow tracer studies at concentrations which do not alter the metabolism and investigation of isotope fractionation. The same group investigated the feasibility of Zn isotope ratio imaging in tracer studies to locate different Zn metabolism in various anatomical features in rat brain, which can be harnessed to measure trace element kinetics in tissues at a microscale level.[85] The first study to visualize isotope ratios goes back to Woodhead *et al.* who resolved differences in the Sr isotope ratio across a barramundi otolith.[86] Other isotope ratio imaging applications comprise the transgenerational labelling of Ba in fish and the uptake of Zn into wheat grains.[87-89] One interesting application of LA-MC-ICP-MS was shown by Paul *et al.*, who were able to explain the change in the isotope ratios of Sr in fish otolith by its migration pattern.[90] In a similar study, Prohaska *et al.*[91] investigated otoliths to assess habitat use and migration in a river system to reconstruct life histories of fish. As shown in **Figure 5**, a split-stream LA-ICP-MS/MC-ICP-MS set up provided elemental and isotopic imaging from the same sampling spot, where contrasts and deviations in isotope ratios was used to follow the age and habitat of fish. Similarly, Avigliano *et al.* targeted the Sr/Ca and Ba/Ca ratios to provide complementary information on fish migration in the La Plata Basin (South America).[92]
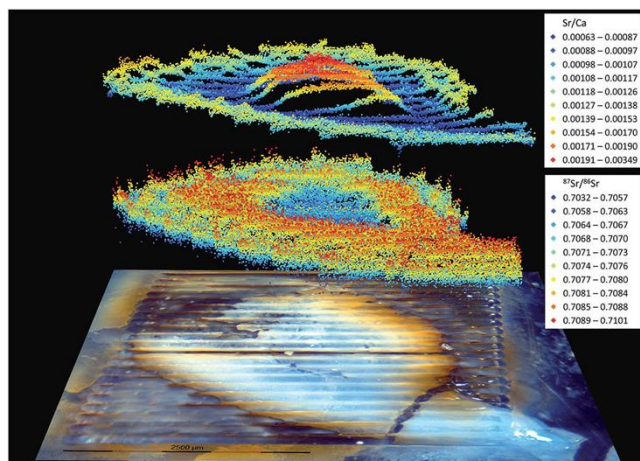
Figure 5: Stacked images of Sr/Ca elemental ratio (upper layer) and ^{87}Sr/^{86}Sr isotope ratio (lower layer) combined with a microscope image of otolith sample after laser ablation. Reproduced from Ref. [91]. Copyright 2016 Royal Society of Chemistry.

Isotope and elemental fractionation in teeth were investigated to interrogate and decipher early hominin traits, describe their habitats and diet and to investigate the uptake of

anthropogenic pollution[83, 93]. Isotope ratios has also been used as pathological marker as shown by Resano *et al.*,[94] who targeted the isotope ratios of Cu in dried urine droplets to diagnose Wilson's disease patients.

2.4.   Time of Flight Analyzers

The simultaneous acquisition of several isotopes offers advantages which are relevant for imaging via LA-ICP-MS. Most ICP-MS instruments employ scanning mass analyzers which operate with dwell times in µs to ms ranges. This limits the number of elements that may be acquired from a transient ion beam and consequently from individual laser shots. This issue instigated the development of the ICP-TOF-MS, which acquires the entire mass range at short integration times. Compared to the scanning of a transient ion beam, TOF technology measures discrete packages of extracted ions in a pulsed acquisition mode for full mass spectrum acquisition at 33, 39.2 or 76.8 kHz.[95-97] Ions are accelerated to equal kinetic energies, which results in different velocities for different m/z. The arrival of ions at the detector is timed and subsequently translated into a mass spectrum. The mass resolution depends on the lengths of the flight path and the focus of the ion package, which both can be increased by reflectrons and ion mirrors. Depending on the ICP-TOF-MS platform, the mass resolution ranges from 900-4000. Direct comparisons between instruments should consider that the usual definition of mass resolution for ICP-TOF-MS and single- or multi-collector instruments are not the same, the latter defines mass resolution at 10% mass peak height, while TOF instruments do so at full width at half maximum (FWHM).[95]

Myers and Hieftje presented the first design and characterization of TOF technology for ICP-MS in 1993.[31] They realized that sensitivity was impacted by non-optimal ion optics and flight paths as well as by the high abundance of Ar$^+$, which caused unwanted saturation of the detector. Other concerns in ICP-TOF-MS were related to large ion numbers causing space charge effects and the broad energy distribution of ions obtained from relatively noisy ICP-sources which limited the duty cycle.[31, 98] Over the years, the detection sensitivity was increased 10 to 1000-fold and ICP-TOF-MS is now suitable for the analysis of trace elements.[99] TOFWERK introduced an instrument that employs a Notch filter to remove abundant matrix ions like Ar$^+$. However, this impacts the sensitivity of neighboring analytes with similar m/z.

Although a large proportion of interfering ions can be removed with the Notch filter, the linear dynamic range is limited to approximately 6 orders of magnitude.[95] Using a CRC instead of a Notch filter (also known as a band-stop filter) reduces the level of interferences where the analysis of ^{40}Ca was feasible. Burger *et al.* used He and H_2 as cell gases for operation of LA-ICP-TOF-MS to target ^{40}Ca and ^{80}Se and improved sensitivities by a factor of 1.5-2 by increasing mass resolution.[99] Hendriks *et al.* reported that the sensitivity of ICP-TOF-MS attained approximately 30% of the sensitivity for ^{238}U compared against an ICP-QMS instrument.[95] Burger *et al.* compared various LA-ICP-TOF-MS configurations and analyzed standard reference materials. They found that accuracy and precision were similar to scanning LA-ICP-QMS and reported that the sensitivity was lower by a factor of between 10 and 150 compared against values reported for quadrupole and sector-field instruments, respectively.[99] The simultaneous acquisition improved the precision of isotope ratio imaging. However, the precision reported here was significantly lower than for MC-ICP-MS. One example of isotopic ratio imaging was reported by Monk and Lev, who investigated the ^{68}Zn/^{66}Zn and ^{65}Cu/^{63}Cu isotope ratios in biological tissues which showed potential for toxicological tracer studies.[100]

Recently, a novel ICP-TOF-MS instrument was released by Nu Instruments for acquisition of m/z between 23 and 238 with 39.2 kHz.[97] In a study by Greenhalgh *et al.*, this instrument was used for fast imaging of asbestos fibers in a mesothelioma model.[101] A CRC was used to monitor interfered elements including ^{28}Si, ^{39}K, ^{40}Ca and ^{56}Fe, and principal component clustering was used to distinguish between different asbestos species in cells.

The CyTOF® instrument has a specialized ICP-TOF-MS design that is becoming increasingly important for clinical applications (see section 5.8). Here, a RF-quadrupole mass filter is used to transmit masses above m/z 80. This design is dedicated to the analysis of heavy elements which are used as labels in immunohistochemistry. Unfortunately, endogenous major, minor and trace elements are precluded from the analysis. The sensitivity of the instrument is comparable to common ICP-QMS instruments and the acquisition is carried out at 76.8 kHz.[32] The combination of LA-ICP-TOF-MS and immunohistochemistry has been applied for rapid and highly multiplexed imaging with sub-cellular resolution. For example, Ijsselsteijn *et al.*[102]

recently reported a 40-marker panel for high dimensional and sub-cellular characterization of cancer microenvironments.

The fast acquisition of ICP-TOF-MS in combination with low dispersion ablation will likely be the instrument of choice for rapid and high-resolution imaging. Fast wash-out cells increase sensitivity and the entire mass spectrum from individual laser pulses may be sampled several times.[34] An LA-ICP-TOF-MS operated with a low dispersion/fast wash-out cell of 10 ms permits detection of 100 laser pulses per second. It is also possible to separate individual signal peaks at pulse repetition rates of up to 200-300Hz with novel cell assemblies.[46] These technology and hardware improvements translate into higher sample throughput, which decreases costs and makes LA-ICP-TOF-MS particularly interesting for high volume analysis in clinical settings and 3D imaging. In direct comparison, LA-ICP-QMS may offer increased figures of merit when scanning a limited number of isotopes, which may be advantageous for trace analyses. In contrast the figures of merit are unaffected when targeting a larger number of isotopes by LA-ICP-TOF-MS due to the constant duty cycle of the TOF mass analyzer.

3.   LASER ABLATION

The first LA-ICP-MS instrument was introduced by Gray in 1985.[103] The laser was a fixed Q-switch mode pulsed ruby rod operated at up to 1 Hz and between 0.3 and 1.5 J per pulse with a visible wavelength of 693 nm. The ICP-MS instrument was an ELAN 250 ICP-MS that had been commercially launched at the Pittsburgh Conference in 1983 by PerkinElmer/MDS Sciex.[104] This modular system was developed for geological applications and was designed for direct sampling of rock specimens using a 1 mm beam for representative sampling of hard surfaces without the need for complex and hazardous digestion. The instrument consisted of a simple cell design that enclosed the sample mounted on rotatable cup for maneuvering perpendicular to the beam. The gas flow was introduced tangentially at the level of the sample with a swirling motion and exited just below the window to a four-port tap to facilitate purging of the sample chamber (**Figure 6**). The setup produced detectable peaks down to 10 ng g^{-1} with total washout of single pulses within approximately 20 s. It was noted that, when compared against solution nebulization, there was a disadvantage for quantitative analysis as counting statistics were insufficient, limiting accurate measurements to narrow mass ranges.

This observation in part influenced manufacturers to develop faster scanning quadrupoles and time of flight instruments and set the scene for instrument development for biological imaging applications.
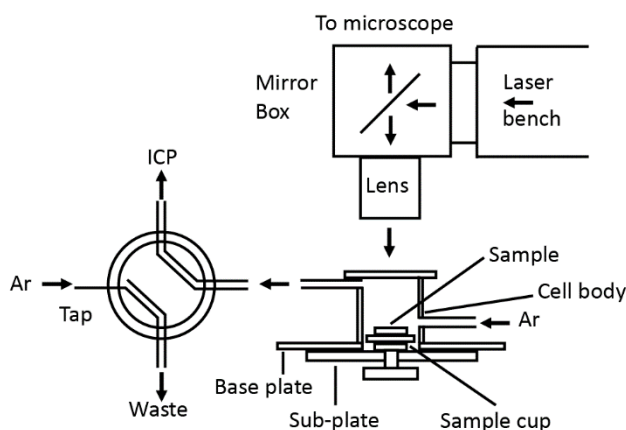

Figure 6: Schematic of the ablation cell used in the first description of LA-ICP-MS. Reproduced with permission from Ref. [103]. Copyright 1985 Royal Society of Chemistry.

3.1.   Laser Ablation Cell Designs

Since the inception of LA-ICP-MS, ablation chambers have undergone continued development by consideration of factors such as aerosol transport efficiencies, transient signal duration, cell geometries and ICP torch configurations to increase spatial resolution and speed of analysis. The desire for improvements has been driven concomitantly by traditional geological applications and the increasing interest in soft tissue imaging. The following brief overview from a selection of representative publications outlines the history of ablation chambers, beginning with rudimentary configurations for solid state sampling of geological materials to modern cells suitable for high resolution imaging applications.

In 1988, Arrowsmith and Hughes[105] considered the overall efficiency of the ablation plume and particle transfer mechanisms to develop the first "two-volume" laser ablation cell (**Figure 7**). The authors placed an ablation cell of $1 - 3$ cm^3 within a pressurized outer box which housed an *x-y-z* stage for sample translation of up to 10 cm x 10 cm. The washout times for single laser pulses improved dramatically to approximately one second with a transport

efficiency of approximately 40%. These configurations formed the basis of many in-house and future commercially designed cells with little development until 2001, when Bleiner and Günther[106] investigated how cell geometry and transfer tube variations affected the transport efficiency of laser-induced aerosols. The cell geometry was not a significant factor for aerosol transport efficiency, however smaller cell volumes decreased the washout time, increased the aerosol density, and decreased dispersion leading to improved signal aspect ratios. Tanner and Günther[107, 108] expanded this observation further with the design of in-torch laser ablation sampling. A sample was placed inside the ICP-MS torch with the laser mounted onto a movable stage and focused through the torch box. This set-up resulted in extremely fast transient signals of 4ms versus 2s in standard configurations and LOD improvements of 100 times. Although imaging was not feasible with this arrangement, it clearly demonstrated that fast wash-out times were desirable for high sensitivity and influenced future designs that were capable of sampling large specimens or multiple targets with minimal dispersion of ablation plumes.
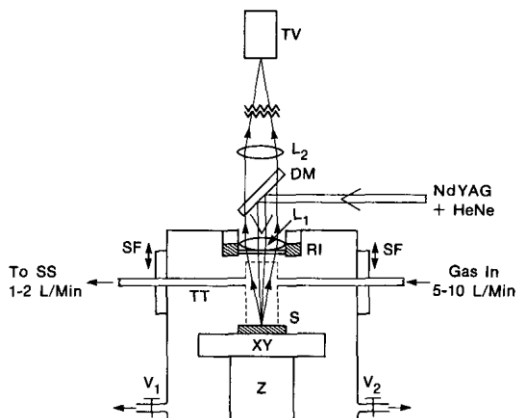
Figure 7: Schematic of first report of a two-volume laser ablation cell. Transfer tube (TT); secondary gas source (SS); sliding flanges (SF); dichroic mirror (DM); ring illuminator (RI); flow control valves (V_1/V_2); lenses (L_1/L_2); sample (S) on *XYZ* translation stage. Adapted with permission from Ref. [105]. Copyright 1988 SAGE Publications.

Liu *et al.*[109] further developed the two-volume arrangement by placing a movable active inner cell inside an external cell that was large enough to accommodate multiple targets or large specimens. The inner cell was connected to a 1 m long 3 mm i.d. transfer line to the ICP-MS instrument and demonstrated improved memory effects compared to similarly large volume

cells whilst maintaining the relatively fast washouts of small volume cells at approximately 400 ms.

Becker *et al.* demonstrated near-field LA-ICP-MS in 2005 using a silver needle and 532 nm Nd:YAG laser for a claimed 150 nm beam diameter.[110] The potential applications foreseen by the authors in nanoimaging have not yet come to pass, not because the work was technically flawed but because reliance on precision experimental setups and in-house produced components (**Figure 8**) are not immediately compatible with transferrable workflows. While the near-field effect, applied to discrete sampling, demonstrated LA-ICP-MS could make equivalent measurements to other nanoscale chemical analysis techniques, it did not demonstrate sufficient improvements over alternatives to justify the delicate experimental setup required when other established workflows could be used (e.g., Pushie *et al.*[111]).
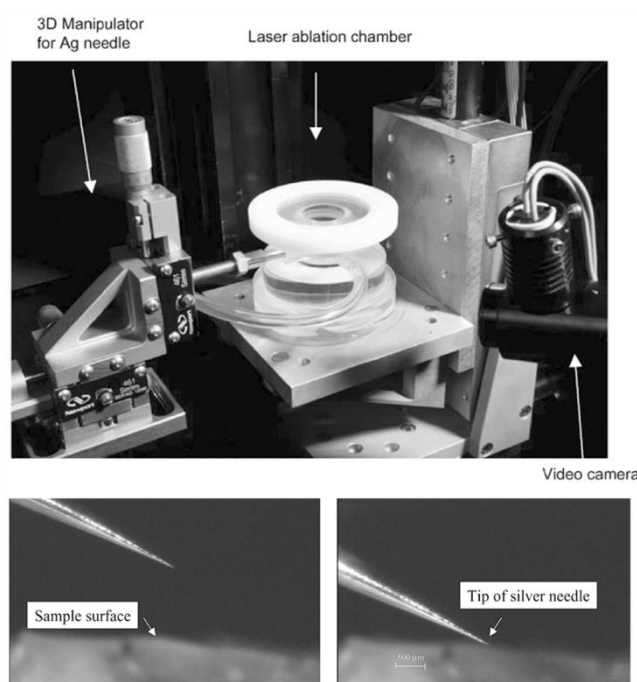
Figure 8: Near-field LA-ICP-MS configuration. A precision *XYZ* manipulator holds a thin-tip (150 nm) silver needle in position inside the Ar-pressurized ablation chamber. Reproduced with permission from Ref. [110]. Copyright 2005 Royal Society of Chemistry.

A significant improvement from these previous designs was introduced by Müller *et al.*[112] in 2008 with a two-volume cell with a large sampling area, a moderate washout of less than 1

second, invariant gas flows around the ablation site, and a computer controlled *xyz* stage. A small 2 cm^3 funnel-shaped cup was fixed with a stainless-steel articulated transfer tube that kept the cup above the sampling target within a gas tight chamber of approximately 380 cm^3. Unlike previous arrangements, the dead volume of the chamber was minimized by placing the *xy* stage outside the sample chamber. An off-axis camera was placed above the chamber to view the entire sample area for convenient setup of ablation experiments, and a light source was placed beneath the chamber for transmitted illumination. This design was the basis for commercial cells still in use today manufactured by Resonetics (Laurin Technic) and Teledyne (HelEx II). In addition to the ablation chamber design, the transfer line has an influence on the dispersion of the ablated aerosol. Accordingly, an Aerosol Rapid Introduction System (ARIS), which consists of a low volume transfer line, is also available for the HelEx II, and has been reported to reduce the washout time to 40 ms.[113]

In 2015, Douglas *et al.* described a fast washout cell specifically designed for acquisition of high-resolution images or high-resolution sampling.[114] The cell consisted of an integrated ablation chamber, transport tubing and an ICP torch that provided a low-volume flow path for resolution of single-shot peaks widths of 1.5 to 4ms. This was equivalent or better than the in-torch ablation described earlier, with the ability to image large sample areas or multiple targets. In a variation of the two-volume concept, fast transient signals were generated via the use of a "sniffer" device at the point of ablation (**Figure 9**). The sniffer was connected to a dual concentric injector (DCI) torch via a fused silica conduit. The DCI was designed to directly inject the ablation plume effluent into the ICP to minimize dispersion or dilutions of the aerosol. The sample tray within the ablation chamber was magnetically coupled to an external *xy* stage with 25 mm × 25mm enabling imaging of moderately sized targets. The jitter and accuracy of the stage were not reported.
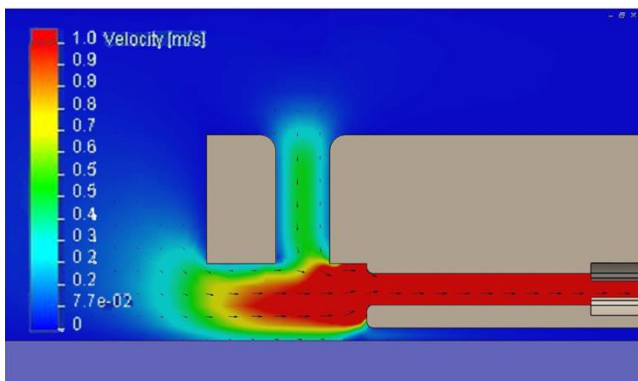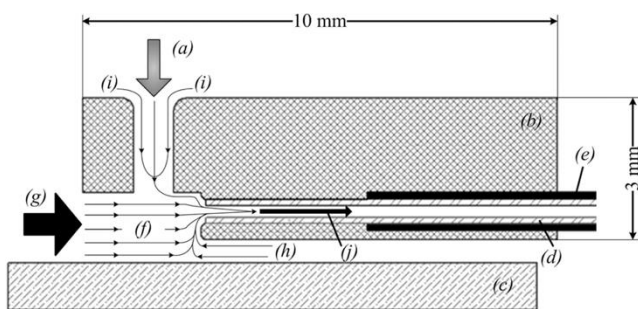
Figure 9: "Sniffer" interface reported by Douglas *et al.*[114] Schematic of device (top) where direction of the laser beam A); "Sniffer" cell body B); sample C); fused silica transport conduit D) fused silica support tube E); microchamber within which the ablation plume is contained F); main bulk of gas flow entering the microchamber G); minor gas flow that enters the microchamber from beneath H); minor gas flow down the laser access port I); laser-induced aerosol direction of travel toward the ICP J). Heat map (bottom) showing computer aided design model of representative local gas velocities in the "sniffer" interface. Reproduced with permission from Ref. [114]. Copyright 2015 American Chemical Society.

In 2013 Günther and colleagues[115] described the development of a low dispersion laser ablation cell based on a tube design that produced single shot aerosol plumes of less than 30 ms. This was applied to the analysis of HER2 cancer biomarkers at approximately 1 μm resolution. This cell design was later applied to LA-ICP-TOF-MS analysis of geological samples by the same group.[116, 117] This tube design was further developed by van Malderen in a series of papers that reported development of a low dispersion ablation cell housed within a "Cobalt" ablation chamber.[46, 118, 119] This layout used a gas-tight chamber within which various configuration of cells could be placed and customized to the need of the user. The fast washout cell configuration comprised of a transfer tube placed above the sample in which a high velocity stream of He was used to capture the ablation aerosol for transfer via

polytetrafluoroethylene (PTFE) tubing to the ICP torch.[119] The sample holder was mounted on a *z* stage and angled at 4° relative to the focal plane to limit opportunities for collision between the sample and the ablation cell. Constant distance between the sample and the focal point was maintained by tracking and autofocusing during line scans (**Figure 10**). The sample holder accommodated large specimens or multiple targets with a volume of up to 100 × 100 × 14 mm^3. The *xy* stage consisted of piezo-based stick-slip linear positioners with a closed loop accuracy of 40 nm. The "Cobalt" cell has been commercialized by Teledyne Cetac Technologies and incorporated into the Iridia™ laser ablation system. The commercial product has a claimed 99% signal washout within 4 ms.
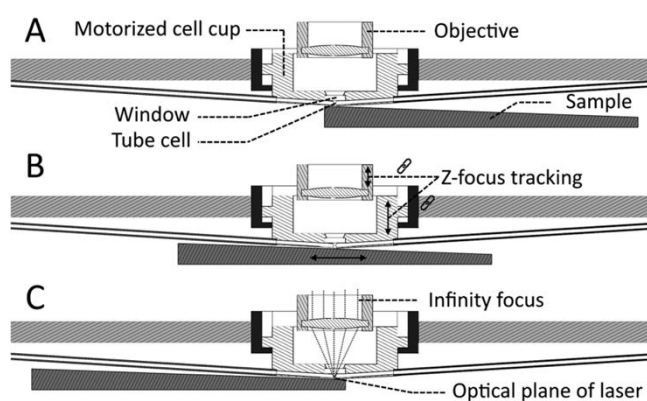
Figure 10: Schematic of the sampling inner cell assembly. In all 3 sample positions (A-C), the distance of the tube cell to the sample surface is maintained during the scan. Reproduced with permission from Ref. [119]. Copyright 2020 American Chemical Society.

Other commercially available "fast" washout cells are available from Elemental Scientific Lasers (ESL). The TwoVol3 cell has a specialized imaging cup combined with the DCI torch with claimed washouts of less than 1 ms. The *xy* stage is designed for large specimens or multiple targets with 100 mm × 100 mm translation and 10 nm accuracy, and a *z*-stage to control the sample surface-to-cup distances. A prototype version of this cell was applied to the analysis of asbestos fibers in cellular models of mesothelioma with a lateral resolution of 3 μm.[101]

4.   QUANTIFICATION

4.1.   Basic considerations and external calibration

Reliable quantification in LA-ICP-MS imaging requires consideration of the matrix dependence of aerosol formation, mass flows, aerosol transport efficiencies, and the potential for signal drift due to plasma fluctuations over the duration of an imaging experiment. Common approaches involve periodic acquisition of matrix matched calibration standards consisting of certified reference materials (CRMs) or laboratory prepared standards. CRMs provide a one-point calibration with a high degree of traceability. However, the accuracy of quantification using CRMs is dependent on the similarity of the CRM and the sample in terms of the analyte concentration and its biochemical and physical properties. The accuracy decreases if the sample analyte concentration is not of a similar magnitude to that of the analyte in the CRM. Some calibration strategies have modified CRMs to better match the sample via manipulation of the concentrations or physical properties. For example, Oseas da Silva and Zezzi Arruda spiked CRM 100 (beech leaves, IRMM), 1575a (tomato leaves) and CRM 281 (rye grass) with S and/or Se at various concentrations for construction of calibration curves for quantitative analysis of sunflower leaves.[120] The procedure involved the homogenization, grounding and pressing of the CRM into pellets, with subsequent digestion and cross-quantification to determine the exact concentration. A similar approach was followed by Wu *et al.* for quantitative imaging of micronutrients in *Elsholtzia splendens* (Shiny Elsholtzia) leaves.[121]

Several other uses of CRMs for the quantification or validation of elemental concentrations in diverse biological tissues have been reported. This includes MACS-1 and 3 (synthetic calcium carbonate) and NIES-022 (otolith) which were used for quantification of elements in otoliths.[122-124] TB-1 (basaltic glass) and SRM 1486 (bone meal) were analyzed to quantify elemental concentrations in Atlantic Salmon (*Salmo salar L.*)[125] and common carp (*Cyprinus carpio*)[126] fish scales. Shells have been quantitatively analyzed employing BCS 393, JLS-1 and GSR-6 (all Limestone).[127] LGC 7112 (pig liver) has been used to determine trace elements in the liver and kidney of sheep and in pig liver.[3, 4] Essential trace elements were mapped and

quantified in rat brain by calibration against pellets of TORT-2 (lobster hepatopancreas), DOLT-2 (dogfish liver), and DORM-2 (fish protein).[128]

The availability and applicability of CRMs are justified in a few cases where the CRM is a near match of the sample, however, most biological CRMs are provided in form of lyophilized powders which are not directly comparable with fresh tissue samples. Nevertheless, dissimilar CRMs have been used to provide high traceability and relative quantification. For example, the NIST Multi-Element Glasses such as SRM 610-614 are popular CRMs used for the quantification of elements in disparate samples like fish scales,[125] otoliths[129-132] feathers,[133] claws,[134, 135] and teeth.[136] The lack of true matrix-matched CRMs motivated the manufacture of laboratory made-tissue standards that match the properties of the sample as closely as possible. Reference tissues are often sourced from the same tissue type of the target species. Tissues are then spiked with a dissolved metal standard and homogenized, pressed into molds and sectioned on a cryotome or microtome at the same thickness as the sample section.[137] The first preparation protocol for matrix-matched tissue standards was presented in 2005 by Becker *et al.*, who homogenized brain samples, spiked various concentrations of Cu, Zn, P and S, and sectioned a set of four standards including one non-spiked homogenized brain tissue that was used for blank correction.[138] The elemental concentrations in the standards were cross quantified with a standard addition approach. Cross-quantification is essential to determine the exact concentration in the standards and is most often performed by digesting and analyzing an aliquot of the standard with stand-alone ICP-MS.[137]

The production of standards that exactly match the samples is a Sisyphean task; native biological tissue is complex, and its properties vary on the nano and microscale.[139] Consequently, artificial standards simply cannot reflect the full spectrum of physical, biological, and chemical features, and at best represent the average characteristics of the sample. When performing calibration and quantification with matrix-matched tissue standards, the following points should be taken into consideration:

- Biological tissues are diverse and heterogeneous. As every organism has an individual genomic content and is exposed to unique environmental influences, chemical and

biological differences are inevitable even if the same tissue from two animals of the same species are obtained. When investigating pathological changes, these differences may become even more pronounced. In other cases, changes may be very subtle.

- The use of animal tissues to produce matrix-matched tissue standards defines the lower calibration limit due to the abundance of essential trace, minor and major elements. This may limit accurate determination of essential elements which are reduced in concentration due a biological or pathological response and certain anatomical features that have a concentration below the tissue's average.

- The homogenization of a tissue changes its integrity and consequently, the ablation and aerosol formation of a standard and a sample will not be entirely comparable. Homogenization is also a delicate process which is difficult to standardize.

- Parameters such as density, hardness, and chemical properties vary on the microscale due to tissues containing various anatomical structures with different biochemical entities. The aerosol formation, size and transport therefore vary across a single sample and cannot fully be simulated with homogenized standards.

- The sectioning of standards induces artefacts which are visible as different tissue thicknesses and surface roughness. On one hand, this may result in inadequate laser focus and on the other hand, thicker areas within a standard may create the impression of higher concentrations.

- Sample and standard preparation which can including thawing, drying, deparaffination, hydration, washing and staining may induce additional artefacts.

- Biological variation is the biggest source of uncertainty. Differences in mean elemental concentration in a cohort introduces error that most likely far outweighs the uncertainty in ablation characteristics.

The use of CRMs or laboratory-made tissue standards always comes with a trade-off concerning traceability, precision, repeatability, and/or accuracy; specialized protocols aiming to provide adequate tissue matches and analyte concentration, texture and composition are often tedious and involve numerous steps limiting repeatability/reproducibility. Simple preparation protocols which aim to provide traceability

and comparability are often not able to mirror the complexity of native biological material. This causes a dilemma for quantification of elemental distributions via LA-ICP-MS and raises the question whether absolute quantification of elements is feasible, or whether it is merely comparable relative to the individual set of standards employed. For most applications absolute concentrations are of subordinate importance as control animals and tissues are usually analyzed when comparing elemental distributions and localized concentrations. Westerhausen *et al.*[140] discussed this dilemma recently: "[…] *is it possible or even desirable to manufacture representative matrix matched standards for absolute quantification? Given that most investigations of biological systems require measurement of changes in elemental concentrations relative to a control sample due to a diseased state or treatment regimens, it is more desirable that standards are easily prepared, robust, and reproducible to provide a consistent response, rather than an absolute amount.*" This philosophy is reflected in many studies where no or only partially matched standards were employed for calibration. For example, numerous studies compare sets of samples and standards made from different tissues and/or species, e.g., chicken breast against mouse brain;[141] bovine breast against human breast;[142] sheep brain against human prostate;[66] mouse brain against mouse heart.[78]

Accordingly, other non-matrix-matched standards and materials that are easier to produce, control and characterize have become increasingly popular. Bonta *et al.* used printed standards on paper with an ink-jet printer.[143] Reifschneider *et al.* proposed egg yolk for the preparation of standards.[144] In its undenatured liquid form, egg yolk was easily spiked with liquid standards, and subsequent controlled denaturation resulted in homogenous solid standards for the quantification of Tm in mouse tissues. The same authors embedded samples in spiked epoxy resins,[145] and Austin *et al.* spin coated spiked polymethylmethacrylate (PMMA) films for the quantification of transition elements in homogenized tissue sections.[146]

The use of hydrocolloid gel-based materials including gelatin[147] and agarose[148] for productions of standards are reported with increasing frequency. These materials can easily be modified and spiked by liquification at elevated temperatures (50-80 °C). Thin films of these gels can be obtained from sectioning,[149] spotting,[147] or filling into defined molds.[140] Šala *et al.* investigated thicknesses and surface distributions of gelatin at various drying and curing conditions to fabricate highly homogenous standards which were suitable for the calibration

of elements in soft biological tissues.[147] Westerhausen *et al.* presented a simple concept for the preparation of mold-prepared gelatin standards.[140] They showed that filling self-made or commercial molds provided precise thickness control for preparation of highly defined and homogenous standards with improved ablation characteristics when compared against standards prepared from native animal tissue. They also compared gelatin extracted from bovine, fish and porcine sources and showed that the background levels of elements varied, allowing selection of gelatin to optimize the calibration of lower concentrations ranges. The background concentrations of gelatin were further decreased in an intermediate step where metal binding resins were mixed with liquified gels and separated using centrifugation, producing standards with very low residual trace elements (**Figure 11**).
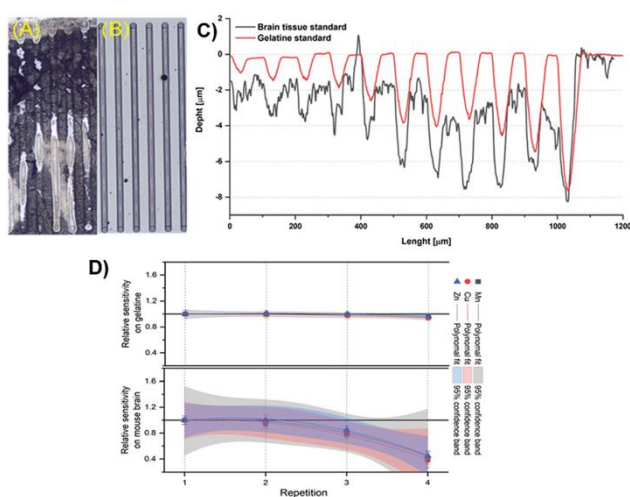
Figure 11: A) Ablated animal tissue and B) gelatin standards. C) Profilometry measurements showed gelatin standards had more consistent ablation characteristics with increasing laser power. D) Gelatin standards also provided more confidence in repeated measurements than animal tissue standards. Reproduced with permission from Ref. [140]. Copyright 2019 Royal Society of Chemistry.

4.2. Internal Standardization and Calibration

Instrumental drifts during long acquisition times, varying tissue thicknesses across a tissue section, spontaneous plasma fluctuation and tedious standard preparation prompted strategies to perform internal standardization and calibration while simplifying standard preparation.

Signal drifts can significantly impact accuracy if not further addressed. For example, Limbeck et al.[150] demonstrated that signal intensity can decrease by up to 25% within 5 hours. Feldmann et al.[3] proposed that a one-point calibration with a CRM using the ^{13}C isotope for signal normalization provided improved accuracy. It was argued that laser energy fluctuation, varying sample thicknesses or the change of the absorption coefficient of the ablated materials could be corrected. Carbon-13 normalization was subsequently investigated and employed in several papers.[121, 151] In contrast to these studies, Todoli and Mermet applied LA-ICP-atomic emission spectroscopy (AES) to demonstrate that carbon forms gaseous species during the ablation process limiting its use as internal standard.[152] Frick and Günther undertook a fundamental study that confirmed this finding.[153] The formation of gaseous C species depended strongly on the matrix and ambient conditions.

Given that other endogenous elements are not homogeneously distributed, novel methods for internal standardization were explored which involved the application of an exogenous standards added to sample aerosol or deposited directly on the tissue sample. For example, Austin et al. proposed thin spin coated PMMA films that were spiked with a metal standard as support material for sample sections. The combined ablation of samples and the PMMA substrate allowed monitoring of the spiked metals for normalization.[146] Similarly, Grijalba et al. used a metal spiked gelatin layer deposited on the sample in combination with matrix-matched standards for the quantification of U in rat kidneys.[154] Konz et al.[76] developed a sputtering protocol to deposit thin (9 ± 1 nm) Au layers on human eye tissue (**Figure 12**). The ^{197}Au signal was used for internal standardization for Mg, Fe and Cu and compared against ^{13}C normalization. They found that the latter resulted in a drastic loss in structural contrast. Gonzalez de Vega et al. also employed this technique for the analysis of Ca, Fe, Cu and Zn in breast cancer tissues.[142] Bonta et al. used the same approach and showed that Au signal normalization mitigated signal drifts between laser scan lines and improved precision by decreasing the standard deviation from 15% to less than 5%.[143]
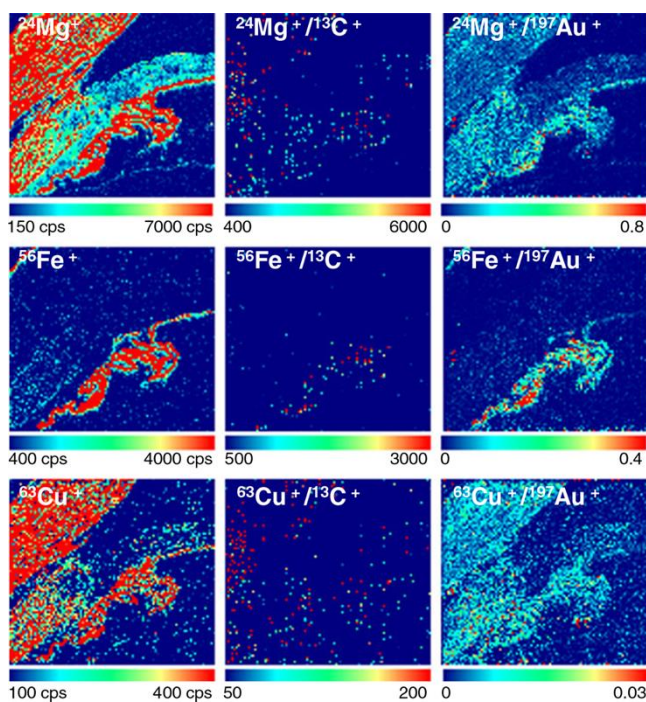
Figure 12: Elemental images of FFPE eye sections with sputter-coated with Au. Left column: Mg, Fe, and Cu images; middle: ^{13}C-normalized; right ^{197}Au-normalized. Reproduced with permission from Ref. [76]. Copyright 2013 Springer.

O'Reilly *et al.* used homogenized sheep brains prepared as matrix-matched standards and immersed in solutions containing Rh as internal standard and varying levels of Fe. Murine brain samples were immersed in the internal standard solution only, which did not cause Fe wash-out effects. Rh appeared to be distributed quite homogeneously and the Rh signal was used for normalization.[155]

The deposition or on-line addition of a known amount of material is attractive for direct standardization and quantification using isotope dilution (ID) approaches. In ID, the sample is spiked with an isotopically enriched standard with known concentration and isotopic abundance. Assuming a natural abundance in the sample, the calculation of elemental concentrations may be calculated according to **Equation 1**, where c is the concentration, m the mass, M the molecular mass, A the isotopic abundance, R_m the measured isotopic ratio and R_{sp} and R_s the isotopic ratios of isotope a and b of the sample (s) or spike (sp). A detailed mathematical deduction and fundamental applications of ID in ICP-MS and LC-ICP-MS has been presented by Rodriguez-Gonzalez *et al.*.[156]

$$c_S = c_{Sp} \frac{m_{Sp}}{m_S} \frac{M_S}{M_{Sp}} \frac{A_b^{Sp}}{A_a^S} \left(\frac{R_m - R_{Sp}}{1 - R_m \cdot R_S} \right)$$

Eq. (1)

If spatial distributions are not of interest and LA-ICP-MS is used as a direct sampling technique, the application of ID is straight forward and the sample and spike can be homogenized before analysis via LA-ICP-MS.[157] However, if the spatial distributions are to be quantified, several additional considerations are required. ID can be categorized into off-line (or, in this case, on-tissue) ID and on-line ID. For on-tissue IDA, the isotopic spike must be deposited homogenously over or under the sample. Homogenous mixing of the sample and spike is assumed upon ablation and isotope ratios are calculated and translated into a concentration for each pixel. Success of this method requires that the spike be deposited with a high degree of homogeneity otherwise systematic errors may be introduced leading to apparent image artefacts, or incorrect quantification. Similarly, on-tissue ID will produce errors if the aerosols are not mixed homogenously or if the aerosol of the spike and sample have different properties such as varying particle size. It is therefore essential to ensure that the deposited spike layer and the sample have similar physical and biochemical characteristics. Regardless, intrinsic effects such as micrometer scaled variations in density or different biochemical structures (e.g., muscle fibers compared against fatty tissue) will always produce different aerosols across the sample and should be considered irrespective of the quantification method.

Moraleja *et al.*[158] used a commercial ink-jet printer for deposition of isotopically enriched spikes onto tissues for ID quantification of Pt-based cytostatic agents in whole murine kidney. Feng *et al.* deposited and dried isotopically enriched solutions directly on the tissue using a hydrophobic containment barrier for the quantification of Fe, Cu and Zn in Alzheimer models of murine brains.[159] Thieleke and Vogt quantified Pb in biological samples and reference materials using isotopically enriched spiked polymers.[160] A sandwich-like structure with three 5-10 μm layers containing a penetration marker (Li), enriched isotope (^{204}Pb) and a correction marker (Bi), and the sample (Pb) was mounted onto a polyester substrate (**Figure 13**).
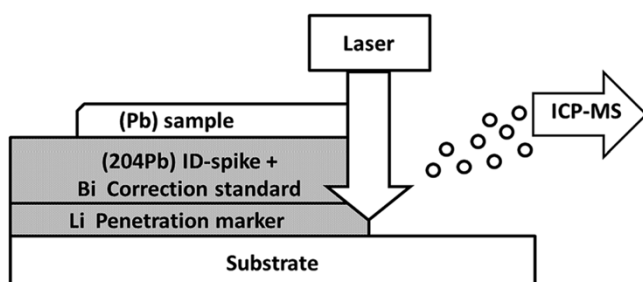
Figure 13: Three-layered arrangement for ID quantification of Pb in biological samples using reference material spikes. Reproduced with permission from Ref. [160]. Copyright 2016 Royal Society of Chemistry.

On-line ID requires a nebulized isotopically enriched spike that is mixed with the sample aerosol. This concept arose from on-line ID for LC-ICP-MS, where transient signals are quantified using a "post-column" spike, however, applying this approach to LA-ICP-MS requires further consideration as using aerosols from two sources complicates the calculation of mass fractions in **Equation 1**. Fernandez *et al.* determined the mass fraction by parallel analysis of a CRM with a known concentration[161] and applied the method to the quantification of powdered samples. Using a customized reference material, Bauer *et al.*[162] followed a similar strategy for the spatially resolved quantification of Pt in biological tissue. Pickhardt *et al.*[163] mounted a microflow nebulizer in the ablation cell which mixed the dry sample aerosol with a wet isotopically enriched standard. The same group used a similar set up, where the aerosol was first generated with a micro-concentric nebulizer, dried via membrane desolvation and added to the carrier gas for the quantification of noble metal nanoclusters.[164] Douglas *et al.*[165] investigated the uncertainty for the analysis of biological tissue and developed a method to directly determine mass flows for ID. Clases *et al.*[166] used a gelatin-based standard material for the calculation of mass fractions and applied on-line ID for the spatial quantification of tyrosine hydroxylase (TH) in the substantia nigra of murine brains and compared it with external calibration. Metal-coded antibodies (anti-TH) were used as proxy for TH, repurposed from the isotopically enriched lanthanides used as metal tags for mass cytometry. As such, on-line isotope dilution was performed with conventional standards for ICP-MS in a reverse ID approach.[166]

5. APPLICATIONS

A basic search of publication databases for the term "LA-ICP-MS" returns around 1,000 papers per year over the last half decade, dozens of which include examples of bioimaging. Pozebon and colleagues have published two reviews of LA-ICP-MS imaging applications in the biological sciences, and the interested reader is directed to these works for a complementary summary of works to 2017.[167, 168]

5.1. Cancer

The annual economic burden of cancer in the USA is estimated to exceed $160 billion with significant research efforts undertaken to improve the prevention, diagnosis, treatment, and prognosis of cancers. The pathology of cancer involves genomic mutations that cause a malignant growth and uncontrolled division of cells. Trace elements are involved in numerous biochemical reactions and act as co-factors for many enzymes and are required for stabilization of cellular structures and maintenance of the genome. Zn has been linked to the proliferation and activation of immune cells[169] and may have a role for indirect initiation and progression of cancer.[170] Fe is necessary for early tumor development, survival and proliferation of neoplastic cells, and promotion of metastases.[171] There is a strong connection between Cu and tumor development as Cu enrichment has been observed in stage I multiple myeloma, acute lymphoblastic leukemia, lung, cervical, and breast cancers.[172] Metal mediated production of reactive oxygen species (ROS), particularly Fe^{2+} and Cu^{2+}, has been well known for many years. Although ROS are necessary for normal functioning of cells, they can be increased by dysregulation of metal homeostasis or insult from exogenous elements leading to Fenton type chemistry to induce the production of hydrogen peroxide, superoxide, and hydroxyl radicals. When biological systems deviate from normal cellular controls, ROS can cause cascading destructive processes that damage proteins, lipids, nucleic acids and other biomolecules, ultimately leading to tumorigenesis.[173]

Platinum-based compounds are at the foundation of metal-containing chemotherapeutics and are indicated for the treatment of a variety of cancers including cervical, ovarian, testicular, prostate and lung cancers, as well as a host of others. The interest in the

therapeutic potential continues unabated since the introduction of cisplatin in 1969[174] driven by the desire to develop chemotherapeutics that have less toxicity and greater efficacy of treatments.[175]

Despite the interest in understanding the role of trace elements in cancer etiology, ranging from the fundamental mechanistic effects of trace elements, the production of metal mediated ROS, and the potential of metal-containing chemotherapeutics, LA-ICP-MS imaging of cancers is underutilized. Applications of LA-ICP-MS imaging cover four main areas: metals and their relationship with underlying pathogenesis of cancer, the discovery of biomarkers, demarcation and stratification of tumors, and investigations of metal containing chemotherapeutics.

Becker *et al.*[176] induced growth of undifferentiated malignant glioma via stereotaxically guided injection of F98 cells into the right hemisphere of a rat brain in the region of the caudate putamen. After 18 days the brains were harvested and imaged by LA-ICP-MS. The Cu distribution within the tumor periphery was approximately half (1.8 µg g^{-1}) of the healthy tissue in the left hemisphere, with local areas of enrichment within the center of tumor, comparable to levels in healthy tissue. A similar distribution for Zn was also observed. A deficit of S, and an abundance of P was also measured within the tumor. Cu and Zn depletion was also observed in a follow-up study that imaged human sections of glioblastoma multiforme.[177] No explanation was provided for the consistent absence of Cu and Zn.

Hsieh *et al.*[178] investigated the spatial distribution of endogenous elements and exogenous Gd and Fe after treatment of a prostatic cancer mouse model with magnetic fluid hyperthermia (MFH). MFH typically involves injection of magnetic particles directly into a tumor with application of an external alternating current to induce rotation and heating of the particles. The authors injected Gd-doped iron oxide into the tumor and constructed two-dimensional heat maps of Gd and Fe following LA-ICP-MS analysis. The heat maps correlated with necrotic tissue, demonstrating that the nanoparticles were stable and the treatment effectively induced cell death proportional to the concentration of the particles. Endogenous P, S and Zn were of lower concentration in the necrotic area, whilst copper was markedly increased. The authors speculated that MFH induced hypoxic stress that generated free

radicals leading to upregulation of the Cu-containing catalytic free radical remover, ceruloplasmin, in the inflamed areas.

Riesop et al.[179] observed that bulk analyses of Zn in cancer breast tissues were generally higher than normal tissue and hypothesized that Zn may be a suitable biomarker for breast carcinoma gradings. Three grades of ductal carcinoma in-situ (DCIS) ranging from grade 1 to 3 were quantitative imaged by LA-ICP-MS. Grade 1 DCIS represents slow growing neoplasms that more closely resemble normal breast cells, whereas grade 3 grow more quickly and have varied size and shape of cell nuclei. The authors reported that Zn levels were strongly associated with cancer grading. Grade 1 tumors had Zn concentrations ranging between 8.3 to 8.5 mg kg^{-1}, Grade 2 between 12.1 and 12.4 mg kg^{-1}, and Grade 3 between 17.3 and 17.9 mg kg^{-1}. The authors concluded that Zn was a potential biomarker that was useful to augment contemporary histological staining for grade determination.

González de Vega et al.[142] surveyed the concentrations of Ca, Fe, Cu and Zn in breast cancer samples to test the hypothesis that essential elements may have diagnostic and prognostic value. The authors constructed elemental images of tumorous and normal tissue areas and reported that the tumors were enriched in all the measured trace elements. The authors concluded that method was suitable for detailed altered metabolism investigations that would be useful in clinical research.

Doble and Miklos[180] investigated the relationship between Mn concentrations in seven different tumors and the relative sensitivity of radiation treatment. Radiation treatment underpins approximately 40% of all cancer cures either alone or in combination with surgery, chemotherapy, and immunotherapy. Despite decades of research that has focused on genomics and enzymological repair of DNA, and free radical scavenging enzymes such as the superoxide dismutases, the underlying biological mechanisms of radio resistance remained elusive. Based on literature observations that *Lactobacillus plantarum* lacking superoxide dismutase activity could efficiently scavenge superoxide radicals,[181] and subsequent findings that this scavenging activity was due to millimole concentrations of Mn^{2+} bound to small molecular components within the cell,[182] the authors hypothesized that some cells in human tumors may be protected from radiation induced ROS damage by small molecular weight

complexes of Mn. Commercially available microarrays of seven tumors (brain, melanoma, mesothelium, lung, prostate, breast, and testis) representing clinically inferred radioresistant, variably resistant, and radiosensitive tumors, respectively, were quantitatively imaged for Mn, Fe, Cu, and Zn. The elemental images were compared against H&E photomicrographs and regions of interest examined. **Figure 14** shows measured Mn data and light micrographs from 53 microarray dots of classical seminoma, and glioblastoma, representing the bookends of the radiosensitive – radioresistant spectrum.[180] Seminoma is known to be radiosensitive with an approximately 98% survival rate after five years and low medians of Mn. Glioblastoma, one of the deadliest brain cancers, and a known clinically inferred radioresistant tumor, had high median Mn levels with a very poor survival rate after 5 years. This association of Mn levels within the tumor and inferred clinical radioresistance / sensitivity, and 5-year survival rates, was consistent across all tumors except for lung cancer. Although small cell lung cancer is initially radiosensitive, the 5-year survival rate is approximately 10%. This anomaly was explained by lung cancer typically not showing significant symptoms until late-stage disease, increasing the likelihood of metastasis. Examination of Fe, Cu and Zn showed no such associations. The authors concluded that Mn concentration is the apex predictor for determining likely response of tumor to radiation therapy and a beneficial diagnostic to stratify patients into groups who likely benefit from radiation treatment, and those who would not.
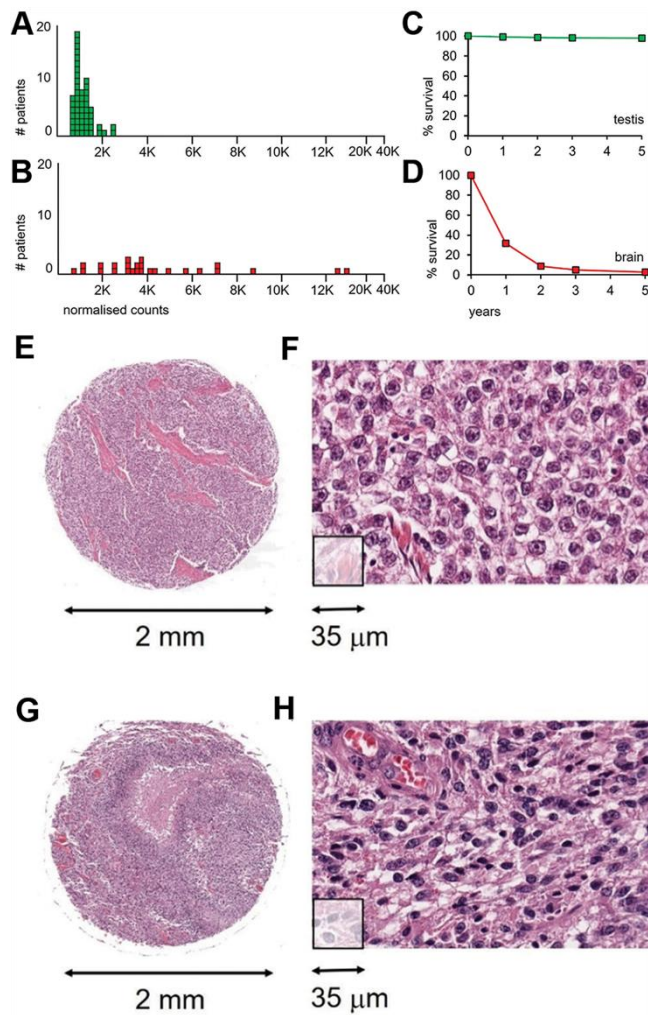
Figure 14: Median Mn levels in tumor sections from patients with cancers of the testis and of the brain and their survival curves. (A) Mn levels from each of 53 classical seminoma patients (green boxes); (B) 26 glioblastoma patients (red boxes). Overall survival curves over a 5-year period for patients with (C) classical seminomas (testis); and (D) glioblastomas. Generic examples of the morphologies of classical seminoma and glioblastoma. (E-F), low and high-power images from patient #47, a 55-year-old male with a classical seminoma showing characteristic collagen streaks throughout the tumor (pink), (E). (G-H), 40-year-old male with glioblastoma showing characteristic abnormal blood vessels and areas of necrosis, visible as the large pink area in (G). Adapted with permission from Ref. [180]. Licensed under CC BY 4.0.

Hare *et al.*[183] measured the spatial distribution of P, S, and Zn in metastatic melanoma in lymph node biopsies. Zn and S were depleted in the tumorous regions, consistent with the observations by Becker *et al.*[176] In contrast, P was depleted in the metastatic melanoma

compared with normal tissue. The authors noted that the tumor could be easily distinguished from the healthy tissue by overlaying the hematoxylin and eosin (H&E) micrograph and the P image. The authors found that the P/S ratio provided another perspective of the tumor boundary, with a gradient increase into apparently uninvolved lymphoid tissue that reflected changes in biochemistry likely representing a response to the tumor.

Zhang et al.[184] further developed the investigation of tumor boundaries by quantification of membrane type-1 matrix metalloproteinase (MT1-MMP) in primary tumors to assess the likelihood of regional lymph node invasion and remote metastasis. MT1-MMP is a promising biomarker to monitor tumor cell invasion as it degrades the extra-cellular matrix whilst concomitantly activating further degradation biomolecules such as pro-MMP-2, as well as promoting angiogenesis. The authors manufactured peptide-coated Au clusters with intrinsic red fluorescence that selectively bound to MT1-MMP in a xenograft lung carcinoma model, and lung and renal human carcinomas, allowing visualization of MT1-MMP by optical fluorescence and quantification by LA-ICP-MS imaging using Au as a proxy. The specificity of the peptide-coated Au clusters was compared against standard immunofluorescence (IF) using anti-MT1-MMP and an HRP-conjugated secondary antibody. Representative IF and elemental images of lung carcinomas are shown in (**Figure 15**). In all three patients, there was concordance of the green anti-MT1-MMP and red Au-peptide areas which segmented tumors and normal tissue, validating that the Au-peptides selectively bound MT1-MMP. Counts of positive MT1-MMP pixels were easily identified in Patients 1 and 2, however in Patient 3 the IF images were ambiguous with no clear positive signals. In contrast the elemental image clearly showed areas of positive Au signal indicating expression of MT1-MMP that identified small tumors, that were not apparent with the IF images. Statistical counting of positive MT1-MMP across 20 random sections for each patient demonstrated superior data dispersion and sensitivity when compared against the IF images. The authors concluded that LA-ICP-MS imaging was capable of detection of small tumors distant from the primary tumor, allowing early diagnosis of primary tumor invasion and / or metastasis, and that the method was suitable to guide treatment regimens if used in clinical settings.
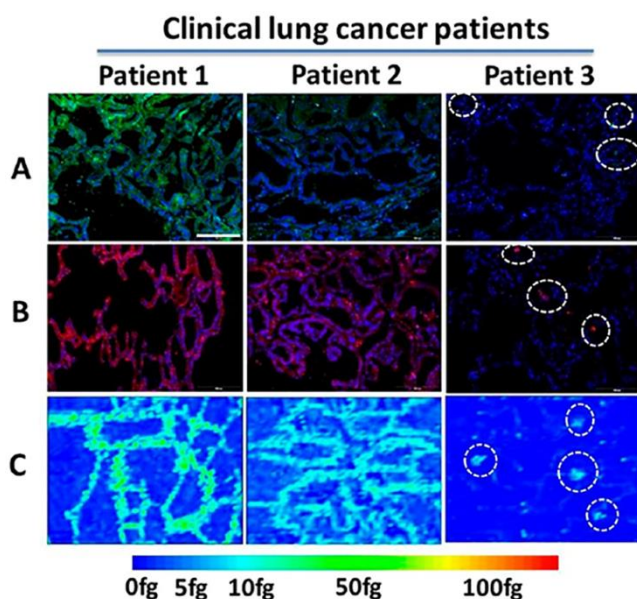
Figure 15: Immunofluorescence (A, B) and LA-ICP-MS (C) images of clinical lung adenocarcinoma patient primary tumor tissues labelled with AuNPs. Reproduced with permission from Ref. [184]. Copyright 2018 American Chemical Society.

González de Vega et al.[185] examined matrix metalloproteinase 11 (MMP-11) by using Au-labelled anti-MMP11 as a proxy for the expression of MMP-11 within metastatic and non-metastatic tumors. The images indicated that the concentrations of MMP-11 were higher in tumors that had metastasized, with more heterogeneity and a larger number of hotspots then non-metastatic tumors, further demonstrating the usefulness of LA-ICP-MS imaging for clinical evaluations. Costas-Rodríguez et al.[186] applied elemental bioimaging using a SF-MC-ICP-MS to measure ^{63}Cu and ^{65}Cu isotope fractionation in a human neuroblastoma cell line. The authors imaged individual cells that showed undifferentiated proliferating and differentiated neuron-like cells were enriched in the ^{63}Cu isotope and was proportional to intracellular Cu content. The Cu isotopic composition was heavier in neuron-like cells than the undifferentiated cells, however the difference was not significant at longer incubation times. The authors concluded that Cu isotopic analysis was suitable for investigations of Cu metabolism at a (sub)-cellular levels. Zoriy et al.[187] applied elemental bio-imaging to the measurement of Pt, Cu, Zn in a murine kidney after administration of cisplatin. The method was the first to show the feasibility of LA-ICP-MS imaging to potentially investigate dose related and cumulative nephrotoxicity, which affects approximately of 20 to 30 % of patients undergoing cisplatin therapy.[188] The highest Pt concentrations were found in the medulla,

moderate levels were in the inner cortex, and decreased progressively to the periphery of the kidney. Copper was enriched in the glomeruli, whilst Zn was enriched in the tubule of the inner cortex. The authors demonstrated that the method was suitable to track the distribution of Pt at therapeutic dosages within the kidney, and potentially the disturbance of Zn and Cu concentrations after treatment.

Bianga et al.[189] evaluated the complementarity of matrix-assisted laser desorption/ionization (MALDI) and elemental bioimaging for the detection of Pt chemotherapeutics in colorectal and ovarian peritoneal carcinomatosis after heated intraoperative chemotherapy (HIPEC). HIPEC treats residual tumors after surgical resection via application of heated anti-cancer drugs for 30 to 60 minutes. Four tumor samples were surgically removed before and after oxaliplatin and cisplatin HIPEC applied at concentrations of 460 and 75 mg/m^2, respectively. The tumors removed before treatment were used as controls and the post-treatment samples were imaged to measure the penetration of the drug into the cancerous tissue. The MALDI and corresponding LA-ICP-MS images of oxaliplatin were concordant, showing poor penetration of the drug into both tumors. The elemental images clearly showed that Pt distribution was confined to the periphery, and MALDI showed colocalization of monomethionine conjugates of the drug. In contrast, MALDI did not detect any known cisplatin molecules, however, the elemental image confirmed the presence of Pt throughout both tumors, demonstrating effective penetration of the drug. The authors concluded the dual imaging method was useful for understanding the dose relationship and efficacy of treatments in the clinic. Carlier et al.[190] further investigated HIPEC administration of cisplatin using synchrotron x-ray fluorescence (XRF) and LA-ICP-MS imaging to measure the Pt distribution and penetration in a xenograft model of ovarian cancer following intraperitoneal chemoperfusion. LA-ICP-MS imaging demonstrated that hyperthermic (40-41 °C) application resulted in up to up to 5-fold higher concentrations of Pt throughput the tumor, whilst XRF showed deeper penetration of Pt, when compared to chemoperfusion at body temperature. The study concluded that both imaging methods were suitable to determine the penetration depth and distribution of Pt-based drug delivery which may lead to improvements in treatment regimens and successful outcomes.

Egger *et al.*[191] investigated extravasation of oxaliplatin and cisplatin in muscle, nerve, connective and fat tissues following intravenous or central access administration in patients undergoing Pt-based chemotherapy. The authors imaged various tissue sections that were resected from each patient around the location of the port of administration, necrotic skin and soft tissue areas, and a necrotic cubital region of the left forearm. The first patient required immediate surgical intervention on the day of cisplatin extravasation with three sections containing subcutaneous fat and connective tissue, whilst the fourth section contained parts of the pectoralis muscle. The connective tissue had the highest concentrations of Pt, followed by muscle and then fatty tissues. The second patient required surgical intervention 4 weeks post extravasation due to ulceration. A specimen of a subcutaneous necrotic area was obtained near the location of the ulcer and consisted of fat and connective tissues. As before, Pt was detected in the connective tissue at a higher concentration than the fat cells. A second specimen consisting of a cutaneous nerve and connective tissues was also imaged. The connective tissue had five times the amount of Pt when compared against the nerve fibers, which was consistent with the patient being free of clinical signs of neurotoxicity. The authors report that the amount of Pt in fat tissues was most likely underestimated due to cutting artefacts induced in the fatty areas of the specimens resulting in lower cell densities or no tissue and concluded that LA-ICP-MS imaging was desirable to correlate histologic alterations with the amount of drug.

Theiner *et al.*[192] followed with bioimaging of the Pt distribution of conventional and novel Pt-based drugs in murine colon cancer CT-26 models over two weeks of repetitive treatment. The spatial distribution of five drugs, satraplatin, oxaliplatin and three experimental candidates (compounds 1,2 and 3), was determined in the tumors and kidneys of the models treated with each of the drugs at days 4,7,11 and 14. The LA-ICP-MS images clearly showed the differing concentrations of Pt within the tumors and between the administered chemotherapeutics. Consistent with the findings of Egger *et al.*,[191] Pt concentrations were higher in all samples in the tissue surrounding the tumor, especially in areas of loose connective tissue sparsely infiltrated by tumor cells and muscle. Adjacent to the enriched areas were solid tumors with substantially less Pt in relative proportions of compound 2 < satraplatin < oxaliplatin < compound 1 < compound 3. Interrogation of the kidneys of each mouse showed distributions that was consistent with the findings by Zoriy *et al.*,[187] that

satraplatin and oxaliplatin had 8- to 10-times higher Pt levels in the cortex and corticomedullary region than in the medulla. However, there was no correlation of nephrotoxicity and Pt distributions indicating that cell damage such as tubular necrosis cannot be due to Pt alone, and therefore caution should be used when considering renal toxicity based solely on platinum accumulation. The authors concluded that the method was effective to quantify Pt in tumor and kidney sections for comparison against H&E determined histological structures and was suitable to track the efficiency of delivery of novel drugs at early preclinical stages and was essential for lead compound selection.

Lum et al.[193] synthesized two chemically distinct Pt complexes (Pt1 and Pt2) and used a combination of ICP-MS bulk analysis and LA-ICP-MS imaging to determine the relative bioavailability of the complexes compared against cisplatin in various organs following intraperitoneal injection in mice. The animals were euthanized 24-hrs post administration and representative samples of brain, heart, lung, liver, kidney, and testis were bulk analyzed for Pt by digestion and ICP-MS analysis, whilst the kidney and the liver were imaged by LA-ICP-MS to examine the spatial distributions of Pt. Cisplatin was determined to be cytotoxic to nasopharyx cancer cells and normal lung cells, Pt-1 to nasopharyx cancer cells, liver cancer cells, normal keratinocyte cells and normal lung cells, and Pt-2 was nontoxic to all cells investigated. The general premise was to investigate the fate of platinum under the assumption that accumulation is undesirable due to toxicity of non-target organs such as the liver and kidney. Whilst there may be some merit in this hypothesis, Theiner et al.[192] later demonstrated that nephrotoxicity was not proportional to Pt load. Nevertheless, the results indicated that all Pt complexes decreased in concentration order of liver > kidney > lung > testis > heart > brain. In general, the relative concentrations Pt was highest for Pt-2, followed by cisplatin, and then Pt-1. This result confirms that Pt-load is a poor measure of cytotoxicity as Pt-2 was not toxic to all the test cells yet delivered the highest Pt burden. Imaging of representative sections of kidney and liver showed the same trend of concentrations for each complex to that as the bulk analysis, and again showed that higher concentrations of Pt were present in the kidney cortex.

Hucke et al.[194] used integrated proteomic workflows and LA-ICP-MS imaging to investigate the nephrotoxicity of cisplatin following low-dose chronic administration in mice. The authors

hypothesized that organic cation transporters (OCTs) were active modulators of cell signaling and demonstrated that OCT knock-out mice were partially protected from cisplatin induced nephrotoxicity. The authors also found that Pt distributions mainly accumulated in the cortex in the kidney, and that Pt was still detectable 4 weeks after administration of cisplatin (**Figure 16**). The images revealed that the platinum concentrations within the kidney were approximately the same in both the wildtype and knockout mice at the same time intervals, whilst the proteomic analysis showed that genetic deletion of OCT regulated the expression of several genes associated with inflammation and fibrosis, as well as a strong down regulation of the S100 calcium-binding family of proteins, which are known to protect from vascular inflammation and calcification. These findings demonstrated OCT-dependent protein-networks play a significant role in cisplatin-induced nephrotoxicity, and as cautioned previously by Theiner *et al.*,[192] Pt concentrations are not necessarily a good indication of the potential for nephrotoxicity.
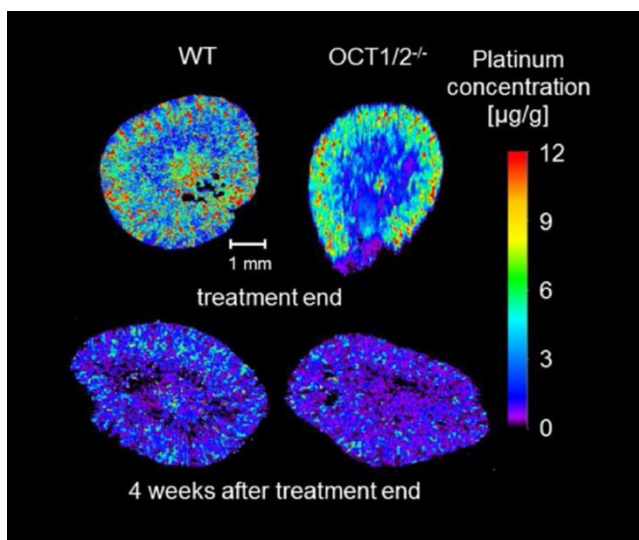
Figure 16: Platinum distribution in kidney slices from WT and *OCT1/2[-/-]* mice at the end and 4 weeks after the end of chronic CDDP treatment, as measured by LA-ICP-MS. CDDP accumulates mainly in the kidney cortex. Reproduced with permission from Ref. [194]. Copyright 2019 Springer.

Niehoff *et al.*[195] investigated the potential of LA-ICP-MS imaging to monitor the penetration of Pt-based chemotherapeutics in tumor spheroids. Tumor spheroids are three-dimensional cell cultures that more closely mimic *in vivo* tumors than the common two-dimensional cell

monolayers and are useful for preliminary investigations of new compounds prior to animal experimentation. The tumor spheroids consisting of bile duct carcinoma (TFK-1) cells were incubated with Pt(II)acetylacetonate, cisplatin and the palladium tagged photosensitizer 5,10,15,20 tetrakis(3-hydroxyphenyl)porphyrin (mTHPP) for 6 and/or 24 hours and then sliced and imaged by LA-ICP-MS. The Pt distribution following incubation with Pt(II)acetylacetonate was homogeneous within the interior of the spheroids at 1.1 μg g^{-1} Pt at 6 hours and increased to 2.0 μg g^{-1} Pt at 24 hours. Within the outer proliferation zone of the spheroid the concentrations were significantly higher at 6.9 and 37.2 μg g^{-1} Pt at 6 and 24 hours, respectively. In the case of cisplatin, the distribution was more homogeneous throughout the tumor, with no obvious concentration increase in the proliferating zone, but rather a tendency to accumulate proportionally with cell density with an average concentration of 0.6 to 0.9 μg g^{-1}. The uniform distribution of cisplatin was attributed to its hydrophilic nature. The tumor spheroid was incubated with the photosensitizer mTHPP with two formulations, dissolved and incorporated into poly(lactic-co-glycolic acid) (PLGA) nano-particles. The dissolved formulation accumulated in the outer layer of the spheroid, whereas the nanoparticles prevented crystallization of the hydrophobic photosensitizer leading to a more homogeneous distribution within the proliferating zones, suggesting that the PLGA formulation may have improved outcomes than the dissolved compound alone.

Theiner *et al.*[196] also applied elemental bio-imaging to the analysis of HCT116 colon cancer tumor spheroids following incubation with oxaliplatin. The authors used an oversampling and image deconvolution processing method to construct 2.5 μm^2 high-resolution images,[197] together with a low dispersion laser ablation cell to increase the acquisition speed. As before, Pt was observed to accumulate at the periphery of the spheroid, and substantially in the necrotic core, indicating that the drug or its metabolites had completely penetrated the spheroid. Construction of a Pt/P image normalized the distribution of Pt with respect to cell density and revealed three distinct regions, high ratios in the rim of proliferating cells and in the necrotic core, and lower ratios in the quiescent middle layer. Klose *et al.*[198] used LA-ICP-MS imaging to investigate the distribution of isosteric Os and Ru anticancer agents in liver, kidneys, muscles and tumors of murine CT-26 colon carcinoma tumor models after a single administration of 15 mg kg^{-1} of each drug. Bulk ICP-MS analysis showed that osmium and

ruthenium accumulated predominantly in the liver, followed by the kidney. Lung, blood and tumor samples contained lower and similar amounts of each metal, whilst muscle tissue did not accumulate significant amounts of each drug. The concentrations of the metals determined from bio-imaging of each organ were in general agreement with the bulk analysis. However, the distributions offered further insights. The distribution of Ru in the liver ranged from 3.7 to 27 μg g^{-1} and was homogeneously distributed, whereas Os was in the range of 1.1–22 μg g^{-1} and was concentrated on the outer rim of the organ with a small number of hotspots in the center. Consistent with observations of Pt-based chemotherapeutics, both metals were higher in the cortex then in the medulla of the kidney. The Ru compound penetrated deeper into the tumor then the Os compound. Although the results were preliminary, this study demonstrated the utility of LA-ICP-MS imaging for investigations of novel metal-based chemotherapeutics.

5.2.   Elemental Uptake and Accumulation

The physiological function of all life is dependent on the availability of essential major, minor, and trace elements. Twenty-eight elements are confirmed as essential for life, with the most recent addition following the discovery that Br is essential for assembly of collagen IV scaffolds in animal tissue in 2014.[199] Essential elements typically remain in fairly narrow concentration ranges to maintain homeostasis and a deficiency or an excess can lead to acute and chronic diseases. Numerous non-essential elements may also be found in biological organisms due to environmental exposure, medical applications, and dietary intake. Certain non-essential elements are potentially toxic, and their physiological effects depend on various factors including concentration, chemical species, and their location within an organism. Regardless of whether essential or non-essential, the absorption of elements is a delicate process that ultimately may impact physiological functions if uncontrolled. Specifically, the uptake, transport, distribution and bioaccumulation of elemental species across biological membranes and interfaces, their impact on metabolic pathways and interaction with endogenous structures is required to understand pathologies and to predict and obviate risks.[200] Different intrinsic chemical and physical parameters like size and polarity as well as the affinity to endogenous structures impact the toxicity of an elemental species. For

example, non-polar compounds like small organotin, -mercury and -lead species can penetrate hydrophobic barriers including skin, cell membranes or the blood-brain-barrier and accumulate in lipid-rich anatomical structures, including the brain, where many adverse effects are encountered.[201] Inorganic metal ions, however, may be taken up by non-selective metal ion transporters and their toxicity is often either linked to the inhibition of proteins and consequently a metabolic disruption, DNA interaction or to the formation of reactive oxygen species increasing oxidative stress.

LA-ICP-MS imaging is well-suited to quantify endogenous and exogenous elements across a wide concentration range and conditions, while also providing data on the spatial distribution in various anatomical structures, and to investigate the interaction of natural and anthropogenic pollutants within organisms. For example, both natural and anthropogenic Hg undergoes species transformations which increases environmental mobility enabling access to various ecosystems.[202] Organomercury compounds are generated from biomethylation during bioaccumulation of Hg, and eventually may impact (human) health due to the consumption of food.[203] Barst *et al.*[204] used LA-ICP-MS imaging to study colocalization of Hg and macrophage centers on immune responses in spotted gar fish (*Lepisosteus oculatus*) and concluded that Hg deposits caused damage to tissue architecture (**Figure 17**). Niehoff *et al.*[205] studied the dietary uptake of three Hg species using *Drosophilia melanogaster*. Here, the authors encountered the challenge of standard preparation due to the high volatility of Hg compounds, which was solved by manufacturing gelatin standards spiked with meso-2,3-dimercaptosuccinic acid (DMSA) for Hg complexation and immobilization. LA-ICP-MS imaging showed that all Hg species bioaccumulated within the organism and confirmed that small non-polar Hg compounds were accumulated and retained at significantly higher rates and may cross biological protective barriers like the blood-brain barrier. Pamphlett *et al.* recently reported a study employing autometallography and LA-ICP-MS imaging to measure Hg in breast cancer samples. In 55% of the cases, Hg was present in intraductal and some luminal epithelial cells of normal breast lobules and in 23% of the investigated carcinomas.[206] The same authors conducted another study on age-related Hg accumulation and found that the concentration increased in anterior pituitary cells with age which may be a factor influencing the decline in growth hormone levels found in advancing age.[207]
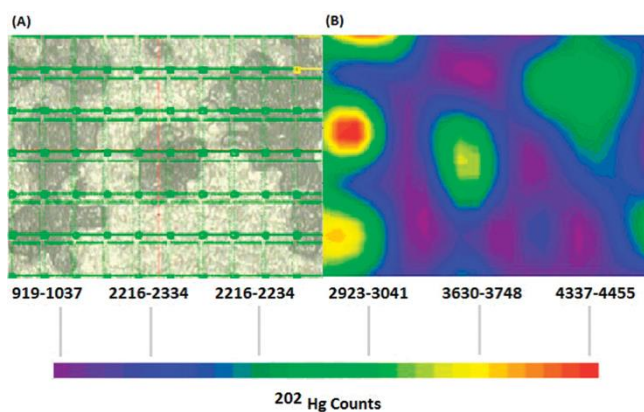
Figure 17: A) Image of fish tissue section before ablation with overlaid raster pattern. B) 3D contour map of ^{202}Hg distribution. Reproduced with permission from Ref. [204]. Copyright 2011 American Chemical Society.

Other than integration of immunohistochemical workflows employing elemental tags as proxies to survey the location and abundance of large biomolecules like proteins, LA-ICP-MS is not able to provide species information, and multimodal techniques and/or complementary techniques such as liquid chromatography (LC)-ICP-MS, are required to estimate toxicological impacts. For example, the uptake and bioaccumulation of As is very different for organic and inorganic forms. Unlike other metal/metalloid-organic species, organic As compounds are far less toxic than their inorganic counterparts but readily bioaccumulate in lipid-rich layers of organisms. Niehoff *et al.*[208] analyzed the uptake and biodistribution of arsenolipids, which are naturally abundant in fish, invertebrates and algae and may bioaccumulate across the food chain. The authors combined elemental and molecular imaging (MALDI-MS) which allowed quantitative As imaging and species identification in *Drosophila melanogaster* (**Figure 18**).

Figure 18: MALDI-MS image of arsenolipid AsHC (*m/z* 333.2193; left), LA-ICP-MS image of As (as ^{75}As; middle), and brightfield microscopy image (right) of the same adult fruit fly

(*Drosophila melanogaster)* section. Reproduced with permission from Ref. [208]. Copyright 2016 American Chemical Society.
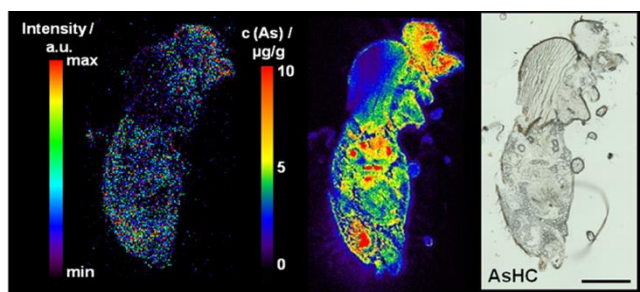
Two dominant routes of exposure for exogeneous and endogenous elements are ingestion and inhalation. LA-ICP-MS has been employed to investigate the source and route of exposure, the metabolic pathways as well as pathogenesis of infections. For example, Eijkelkamp *et al.*[209] applied elemental imaging among other methods to study the role of dietary Zn during bacterial infection (*Streptococcus pneumoniae*) in murine lung tissues and concluded that Zn had a major role in antimicrobial defenses. Hare *et al.*[210] studied the fate of the actinide elements Th, U and Pu in human tissues. They were able to resolve the quantitative distribution of radioactive elements including lymph nodes and lung samples as part of a study investigating natural and occupational exposures. They hypothesized that the route of exposure that resulted in long term retention over several decades was likely to be the inhalation of insoluble refractory oxide particles. In a recent study by Greenhalgh *et al.*,[101] LA-ICP-TOF-MS was employed to target a range of asbestos fibers in a malignant mesothelioma model. The multi-elemental detection of the TOF allowed simultaneous acquisition of several elements for construction of a principal component analysis (PCA) model for fiber identification. Pornwilard *et al.*[211] investigated the elemental distributions of various endogenous and exogeneous elements including S, Mn, Fe, Cu, Zn, Cd, Cr, Cd, Ag, Sn, Hg and Pb in fibrotic and cirrhotic livers. Compared to control liver tissues, elements were diversely distributed in fibrotic liver resulting in significant metal deposits. They further found that total Fe and Cu in diseased liver was significantly higher. Togao *et al.*[212] investigated the toxicological effects of Pb in contaminated drinking water and studied the retention and distribution of Pb in the kidney, liver and brain in a mouse model finding accumulations in the thalamus, hypothalamus and hippocampus. Yamagishi *et al.*[213] investigated the location of Cd in rat placenta. Besides dietary intake of toxic elements, further exposure routes may have to be considered. For example, Mercan *et al.*[214] investigated Pb in children outerwear by LA-ICP-MS, which may cause toxic accumulation due to permanent exposure.

The bioaccumulation and magnification raised major concerns and initiated research on the entry of elements to the food chain, especially from smaller organisms as models to test elemental uptake and toxicological effects. Numerous studies were based on a handful of

species chosen for practical and ethical reasons. It is noteworthy that these standard models have limitations and often cannot mirror the full complexity and biochemistry in higher organisms.[215] Nevertheless, data on the uptake, local concentration and spatial distribution of elements in model organisms provide invaluable information with LA-ICP-MS imaging applied to determine numerous elements in typical models including *Arabidopsis thaliana*,[216] *Drosophila melanogaster*,[205, 208] *Caenorhabditis elegans*,[217, 218] *Danio rerio* embryos,[219, 220] *Daphnia magna*,[221] *Nassarius reticulatussnails*,[222] and various cell lines.[223]

5.3.   Plant Bioimaging

Plants and fungi are important for dietary intake of major essential elements. However, the uptake and accumulation of soil-bound and dissolved non-essential, potentially toxic elements and their introduction into the food chain bear a risk to human health and has been studied intensively. For nutritional considerations, spatially resolved data are less important than speciation data which mainly dictate the toxicological impact after ingestion. Here, LC-ICP-MS emerged as one major technique to provide a detailed and quantitative perspective on elemental species and concentrations. However, to understand the uptake mechanisms of essential and toxic elements and consequences regarding phytotoxicity, LA-ICP-MS imaging is essential and has been applied frequently. Compared to the analysis of soft animal tissues, sample preparation of plants is more tedious, often requiring embedding and sectioning, matrix-matching, and dry samples, if no cryogenic cell is employed. Nevertheless, the development of new sample preparation methods with novel dehydration and embedding procedures prior to sectioning[216, 224, 225] as well as novel approaches for quantification[226] have opened new perspectives and possibilities for LA-ICP-MS.

Narewski *et al.*[227] were the first to apply LA-ICP-MS to the determination of major, minor and trace elements in bark samples of Scots pine, (*Pinus sylvestris L.*) to evaluate the anthropogenic pollution burden in the environment. They presented an innovative approach for matrix-matched standardization and calibration by pressing different bark layers containing varying elemental concentrations into pellets. Additionally, they used the ^{13}C signal for internal standardization. In 2008, Becker *et al.*[228] employed LA-ICP-MS for the elemental imaging in plants where the distributions of Cd, Cu, Fe, Mg, Mn, Pb, Pt, Rh, and Zn were

mapped in tobacco leaves. Here, matrix matched standards were used to quantify each of the elements with ^{13}C as internal standard to mitigate the variability of sample heterogeneity and water content. Several studies followed focusing on uptake and distribution of toxic elements.[229-231] In recent years, LA-ICP-MS imaging was employed for studies dedicated to investigate biofortification,[232] priming,[233] the accumulation of essential elements via tracer analysis,[234] forest pathology,[225] 3D elemental distribution[235] (**Figure 19**) and fertilization.[236] Here, internal standardization using S or C signals and the fabrication of spiked pressed certified standards became a common practice for reliable quantification. **Table 1** lists a collection of studies that used LA-ICP-MS to investigate the accumulation of both essential and toxic elements in plants or mushrooms. Investigated elements, the standardization approach, application and instrumental information are listed, respectively.
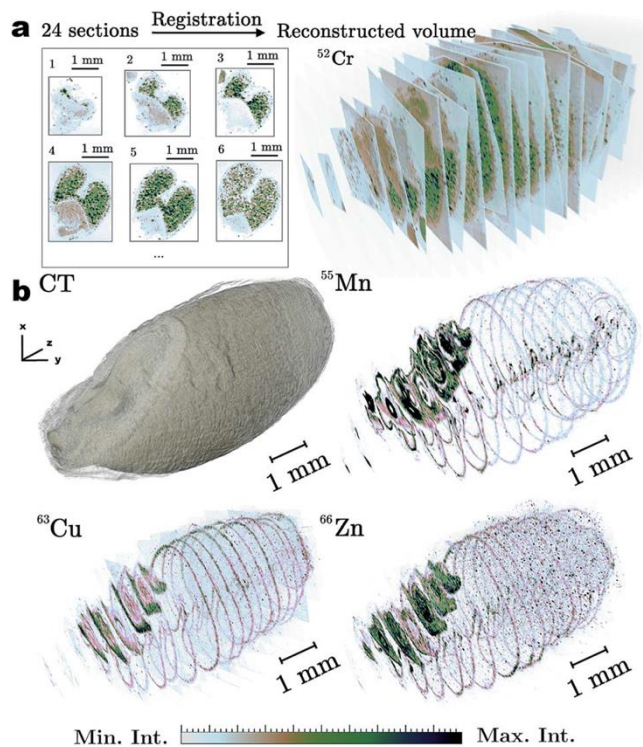
Figure 19: 3D reconstruction of elements in stacked images from rye grass (*Secale cereale)* (A) and bread wheat (*Triticum aestivum*) (B) grains, with reference computerized tomography (CT) image. Reproduced with permission from Ref. [235]. Copyright 2017 Royal Society of Chemistry.

Table 1: Examples of LA-ICP-MS imaging of botanical materials.

Elements and sample type	Quantification approach	Notes	Reference
Al, Ca, Cd, Ce, Cr, Cu, Fe, Mn, P, Pb, S, Ti and Zn in tree bark (*Pinus sylvestris L.*)	[13]C was used as internal standard, SRM 1575 (pine needles), SRM 1515 (apple leaves), SRM 1547 (peach leaves) and SRM 1573a (tomato leaves) were tested. Different bark layers containing different elemental levels were pressed to pellets and analyzed for reliable quantification.	Tree barks were analyzed to estimate the pollution burden caused by anthropogenic sources.	Narewski *et al.*[227] 2000
Cd, Cu, Fe, Mg, Mn, Pb, Pt, Rh, and Zn in tobacco leaves (*Nicotiana tabaccum*)	[13]C was used as internal standard, matrix-matched standards were prepared from dried and spiked tobacco leaves. Standards were fixed on glass using glutaraldehyde.	Quantitative analysis of distributions of toxic and essential elements in thin sections of leaves, shoots, and roots.	Becker *et al.*[228] 2008
Ag and Cu in sunflowers (*Helianthus annuus*)	-	The uptake and biodistribution from contaminated soil were investigated. LIBS was used as complementary and comparative technique.	Galiová *et al.*[237] 2008

Pb, Mg and Cu in sunflower leaves (*Helianthus annuus*)	-	The metal accumulation in sunflower leaves was investigated. LA-ICP-MS was compared to LIBS, AAS and TLC regarding its suitability to perform (multi-) elemental mapping.	Kaiser *et al.*[229] 2009
K, Mg, Mn, P, S, and B in mint (*Elsholtzia splendens*)	[13]C was used as internal standard, SRM 1515 (apple leaves) was dried, ground and pressed for standard calibration.	A [65]Cu tracer was used to investigate the accumulation of copper and other essential elements in leaves. Results were evaluated regarding stress levels and indicated Cu uptake via the petiole and main veins of leaves.	Wu *et al.*[234] 2009
Cu, Pb, Sb and Zn in hay-scented fern (*Dennstaedtia punctilobula*)	[13]C was used as internal standard.	Zn and Cu are concentrated in fronds while Pb and Sb are primarily located in rhizomes. Although Pb and Sb possess different physical properties, the levels of Pb and Sb showed high correlation suggesting similar uptake and transport properties.	Koelmel and Amarasiriwardena[231] 2012
Mg, P, K, Mo, Mn, Fe, Cy, Zn, Rb, Sr, Mo, and Ba in peanut seed (*Arachis hypogaea*)	[12]C was used as internal standard.	The accumulation of 11 elements was studied in the radicle of peanut seed. The authors discussed the accumulation of Mo in the embryonic root of the peanut seed which may have an effect on the plant's yield.	Zhu *et al.*[238] 2012

59

Mg, P, S, K, Ca, Mn, Fe, Cu, Zn, and Al in Sitka spruce (*Picea sitchensis*)	[13]C was used as internal standard.	LA-ICP-MS is presented for use in forest pathology. Elements were analyzed in bark after wounding. A large volume ablation chamber was installed to accommodate samples. Mg, P and K accumulated in a boundary zone between lesions; and healthy tissue distributions were time dependent.	Siebold *et aofl.*[225] 2012
K, Mg, P, S, Cd, Fe, Mn, Zn, and Ca in Syrian bean-caper (*Zygophyllum fabago)*	-	The accumulation of Cd and Zn was investigated in leaves by LA-ICP-MS and micro-PIXE. Cd accumulated in the vicinity of vascular bundles bound to S-containing compounds. The plant's response was investigated using a physiological, proteomic and metabolite approach.	Lefrevre *et al.*[239] 2013
Cd, Cu, Pb and Zn in peas (*Pisum sativum*)	Spiked NIST SRM 1515 (apple leaves) [34]S and ^{13}C were compared as potential internal standards. [34]S was assessed as more reliable.	Cd was evenly distributed while Pb was accumulated mostly in the epidermis and exodermis. Pb was transported towards the endoderm and small amounts translocated to the stele. Zn and Cu were mostly present in the stele.	Hanć *et al.*[230] 2014
K, P, Mg, S, C, Mn, Cu, Zn, Ni and Cd in Alpine Pennycress	[13]C was used as internal standard.	The hyperaccumulation of four different ecotypes was varied. Zn was stored in a different way than Ni	Callahan *et al.*[240] 2015

(*Noccaea caerulescens*)		and Cu. This may be utilized in biofortification experiments.	
Gd in duckweed (*Lemna minor*), cress (*Lepidium sativum*), filamentous algae (*Zygnema*), and water flea (*Daphnia magna*)	-	The uptake of Gd-based contrast agents by plants was investigated by LA-ICP-SFMS. These contrast agents are discharged by wastewater treatment plants and their presence in plants may pose a health risk. It was shown that D. magna may ingest and magnify Gd accumulated in algae.	Lingott *et al.*[241] 2015
P, S and Zn in wheat (*Triticum durum*)	^{13}C was used as internal standard, Grains were embedded in Spurr's resin.	The effects of Zn and N fertilization on the speciation and localization of Zn was investigated. SEC-ICP-MS was used for complementary speciation analysis.	Pergament Persson *et al.*[236] 2016
Gd and Y in maize (*Zea mays*)	Agarose was spiked with metal standards and deposited on a glass slide for quantification.	The accumulation behavior was studied. TOF-SIMS was used as complementary technique. Analytes were found in the epidermis and cortex and root cells. Speciation analysis revealed that oxide species accumulated at the epidermis limiting further uptake.	Saatz *et al.*[242] 2016

61

Zn, Sb, As, Pb and Cd in rice seeds (*Oryza sativa L.*)	[13]C was used as internal standard, Cellulose briquette standards were prepared for calibration.	The accumulation of toxic elements near a mine site was investigate (Zn>Cd>Sb>Pb>As). FTIR was used as a complementary technique.	Basnet *et al.*[243] 2016
Cr, Mn, Ni, Cu, Zn, As, Cd, Hg and Pb in wheat (*Triticum aestivum L.*) and rye (*Secale cereale L.*)	Spiked pressed pellets were used for quantification.	The analysis of serial sections (20-24) allowed the construction of a 3D elemental distribution model. Accumulation of Mn and Zn was observed in the aleurone layer/seed coat, vascular tissue, embryonic tissue. Cr, As, Cd and Pb were mainly accumulated in the grain endosperm.	Van Malderen *et al.*[235] 2017
Ca, Na and K in tobacco (*Nicotiana tabaccum*)	Spiked gelatin was used for quantification.	LA-ICP-MS and LA-ICP-OES were compared regarding their ability to image alkali and alkaline earth elements.	Thyssen *et al.*[244] 2017
Zn in maize seeds (*Zea mays L.*)	[13]C was used as internal standard, IAEA-331 (spinach leave powder) was pressed with SRM-612 (silicate glass) to prepare pellets for quantification.	Zinc and water priming were investigated regarding the accumulation and distribution of Zn in maize seeds. For comparison, diphenyl thiocarbazone staining was performed to visualize the Zn distribution. Unprimed maize seeds were used as reference. Primed Zn was not evenly distributed. Further, Zn is translocated to the shoots and roots of the developing maize seedling.	Imran *et al.*[233] 2017

Cd, Cu, Fe and Mn in sunflower seeds (*Helianthus annuus*) grown in Cd contaminated soil	Matrix-matched standards made of spiked sunflower seed ground and NIST SRM 1573a (tomato leaves) pressed in pellets.	Cd accumulated in sunflower seeds at potentially harmful concentrations and displaced other micronutrients (Cu, F, Mn).	Pessôa et al.[245] 2017
Cs, S, Ca and K in sweet basil (*Ocimum basilicum*)	^{13}C was used as internal standard, NIST 1573a (tomato leaves) pressed in pellets.	Uptake of Cs (100 and 1000 ng mL^{-1} spiking concentration) from soils was investigated.	Ko et al.[246] 2018
S, P, Cu, Mn, Fe and Zn in rice (*Oryza sative L.*)	^{13}C was used as internal standard, SRM 1568b (rice flour) and NCS ZC73028 (rice) were pressed into pellets.	The manipulation of deoxymugineic acid and nicotianamine were evaluated for potential application in biofortification. Perl's Prussian Blue Staining was used to reveal the accumulation of Fe. Different transgenic lines overexpressing associated proteins were analyzed by LA-ICP-MS to determine Fe and Zn distribution.	Diaz-Benito et al.[232] 2018
As in Mushrooms (*Lentinula edodes, Pleurotus ostreatus,* and *Agaricus bisporus*)	-	Mushroom species obtained at markets in nine cities of China were analyzed for As content (0.01-8.31 mg kg^{-1}), speciation (As(III), As(V), MMA, DMA, AsB) and localization. As species accumulated on the surface coat of the cap and the junction of the pileus and	Li et al.[247] 2019

		stipe. The authors conclude that market mushrooms may present a health risk to the general population. ICP-MS and LC-ICP-MS were used to determine total As and speciation analysis.	
Cd in clary sage leaves (*Salvia sclarea*)	^{13}C was used as internal standard (^{34}S was evaluated).	The combination of LA-ICP-MS and chlorophyll fluorescence imaging analysis identified the effects of heavy metals on plants.	Moustakas *et al.*[248] 2019
P, Al, Ca, K, Mg, Cu, Fe, Zn, Cd, As I, and Si in rice (*Oryza sativa*)	^{13}C was used as internal standard and standard solutions were spiked into the cryo-compound.	The distribution profile of elements were compared in wild-type and mutant rice. Distinct accumulation patterns in the phloem region, inter-vascular tissues and different nodes were found.	Yamaji *et al.*[249] 2019
As, Cd, Hg, Sb and Zn in corn seeds (*Zea mays L.*)	^{13}C was used as internal standard, NIST 1573a was pressed into pellets.	As, Cd and Sb were accumulated in seeds from contaminated mining soils. Zn was concentrated in the embryo and pericarp of corn seeds	Gaiss *et al.*[250] 2019
Na, K, Ca, Mg, S, P, and Fe in two genotypes of barley (*Hordeum vulgare*)	^{13}C was used as internal standard. The C content was analyzed in root samples and compared to NIST1573a.	The two genotypes had different tolerance for salt and were analyzed regarding Na toxicity and root growth responses to salt stress.	Shelden *et al.*[251] 2020

5.4. Nanomaterials in the Environment

Nanomaterial manufacture and application are becoming increasingly relevant to medicine and the environment. For biomedical applications, analytical techniques that measure properties such as size and NPs are vital for advancement and incorporation into medical research.[40] In medicine, NPs promise to provide innovative and dedicated solutions for bioimaging, drug delivery and therapeutic applications.[252] However, the development and application of nanomaterials for medical purposes and the discharge of NPs which are routinely used for various applications including paints, hygiene products, clothing, etc., may result in environmental and physiological burdens. Little is known about their uptake, biodistribution, accumulation and toxicological effects. Previous methods to evaluate *in vivo* and *in vitro* behavior of NPs were performed using a variety of techniques including transmission electron microscopy (TEM), X-ray spectroscopy and X-ray diffraction.[253-255] ICP-MS and LA-ICP-MS have the potential to provide a new perspective on the characterization, fate, and toxicology of nanomaterials. Quantitative high spatial resolution LA-ICP-MS has been applied to the analysis of various nanomaterials including AuNPs,[256] AgNPs,[257] doped Fe-oxide particles,[258] and SeCd/ZnS quantum dots.[259] Drescher *et al.*[260] employed highly resolved elemental imaging to determine intracellular Au (25 nm) and Ag (50 nm) nanoparticle uptake and distribution into fibroblast cells (3T3). It was possible to determine the number of nanoparticles per cell at different incubation conditions. Rapid quantification by LA-ICP-MS was performed by calibration using a matrix-matched nitrocellulose membrane that was doped with NP suspensions. In another study, the same authors investigated the uptake of silica NPs with a plasmonic core (BrightSilica) in eukaryotic cells.[261] In addition to applying LA-ICP-MS to quantify the uptake and to compare it to uncoated NPs, they used surface-enhanced Raman scattering to study the interaction with endogenous biomolecules and X-ray microscopy to obtain 3D information on the distribution within cells. Bishop *et al.*[262] constructed a 3D model to study the translocation of AgNP after respiratory tract exposure and found elevated Ag concentrations in the white pulp of the spleen at concentrations exceeding 300 ng g^{-1}. Boehme *et al.*[223] undertook a comprehensive study to investigate the behavior, cellular uptake, and accumulation pattern of Al_2O_3-NPs using and comparing LA-ICP-MS, ICP-MS, flow cytometry and TEM with energy-dispersive X-ray (EDX) spectroscopy.

They analyzed the uptake of three different particles (14, 111, 750 nm) at different exposure doses into HeCaT and A549 cells while considering particle sedimentation and agglomeration in cell culture medium. They found that particles were internalized by cells, however, up to a concentration of 50 mg L^{-1} and an exposure duration of 25 h, no acute toxic effects were detected. In another study, Boehme et al.[263] examined zebrafish embryos exposed to AgNPs and $AgNO_3$. They correlated the level of both ionic and particulate Ag to sublethal and lethal effects. The zebrafish embryos accumulated Ag at increased rates directly (2 hours) after fertilization. In a subsequent study, the authors employed LA-ICP-MS in an ecotoxicological study the investigate impact and potential accumulation of Al_2O_3-, Ag- and AuNPs in *D. rerio* and *D. magna*.[219]

In a recent study by Wang et al.[264] the authors investigated the multigenerational impact of TiO_2-NPs, which can promote the bioavailability of heavy metals in the aquatic environment. Using LA-ICP-MS and TEM/EDX, they found that non-toxic exposure of *C. elegans* to TiO_2 NPs was associated with an increased Cd toxicity in the parental and subsequent generations cultured under pollutant-free conditions. The NPs adsorbed and accumulated ionic Cd, which desorbed after ingestion, accumulated and translocated. The behavior of particulate matter and the interaction with dissolved ions in the environment requires consideration and may play an important factor for elemental exposure as demonstrated in a study of elemental absorption of micro plastics.[265] Koemel et al.[266] investigated the uptake of AuNPs with different surface functionalities in rice plants (*Oryza sativa*). They found that the accumulation was dependent upon the surface charge and modality. Recently, Neves et al.[267] investigated the uptake and distribution in stem and leaves of the medicinal Brazilian ginseng (*Pfaffia glomerata*). Ko et al.[268] studied the behavior and accumulation of Y doped SiNPs in sweet basil (*Ocium basilicum*) and explored the impact on the concentration of chlorophyll, carotenoids and superoxide dismutase (SOD) activity. A study by Wojcieszek et al.[269] investigated the uptake, distribution, bioaccumulation and translocation of CeO_2-NPs in the radish (*Raphanus sativus L.*), whose edible part is in direct contact with the soil where contamination was most likely to occur.

One promising and innovative development for imaging of NPs in biological tissue is analysis via single particle (SP) LA-ICP-MS. Tuning ablation parameters enables protection of

particulate matter from disintegration, allowing transportation of intact NPs to the plasma, where elements are ionized, extracted, mass filtered and detected. The fast mass filtering, detection and signal acquisition from individual NPs as discrete pulses enables determination of number concentrations and NP sizes. Detecting these discrete pulses against the ionic background allows in-situ discrimination between particulate and ionic matter. As such, SP LA-ICP-MS is useful to locate and study the size transformation of NPs even in the presence of ionic metal species. Metarapi et al.[49] applied a SP LA-ICPMS method for NP analysis in biomaterials and demonstrated size and spatially resolved measurements of AuNPs in a sunflower root model. Custom-made gelatin standards containing reference NPs of various sizes and number concentrations were used for method development and size calibration. Yamashita et al.[270] analyzed the distribution of Au- and AgNPs among ionic species in onion cells which were exposed to an Au/Ag-NP solution. Size calibration was performed by solution nebulization ICP-MS of a reference standard. So far, no example for SP LA-ICP-TOF-MS has been presented. However, the multi-elemental and rapid acquisition of individual NPs would be advantageous for the analysis of nanocomposites, which are becoming increasingly important considering current trends for multifunctional NPs and investigations of adsorption effects in environmental and biological matrices.

5.5. Exposure Science

The field of exposure science encompasses the study of organisms with chemical or biological agents within their environments. Several techniques including the analysis of dried droplets of body fluids (e.g., blood[271] or urine[272]) are suitable to investigate acute elemental exposure. However, acute, and chronic exposures to elements are often accompanied by structural integration of elements into hard and durable tissues. This provides unique opportunities to apply LA-ICP-MS imaging to reveal past exposure events for conclusions regarding diets, medical treatments, and certain biological traits. A prominent example is Gd retention in human patients where LA-ICP-MS imaging was applied to the investigation of Gd deposition after enhanced MRI examinations with contrasting agents.[273] In combination with a complementary speciation analysis, Birka et al.[149] found significant Gd levels in skin tissues and identified intact Gd-based contrast agents in tissue extracts. Elemental imaging has been used to diagnose nephrogenic systemic fibrosis in patients suffering from renal dysfunctions

years after MRI examination. LA-ICP-MS/MS was further employed to correlate the levels of Gd with endogenous elements which provided evidence that the pathogenesis of nephrogenic systemic fibrosis was linked to generation of insoluble Gd/Ca phosphate deposits[274] (**Figure 20**). LA-ICP-MS also demonstrated that Gd may be deposited in various other organs including the brain.[275] Similarly, quantitative LA-ICP-MS was employed to study the accumulation of Pt-based cytostatic agents in testis, kidney and cochlea, liver, kidney spleen and muscle, which is of interest to understand side effects including oto- and nephrotoxicity.[145, 276, 277] Halbach *et al.*[220] examined the uptake of the Br containing acetylcholinesterase inhibitor, Naled, in zebrafish embryos and found 280-fold enrichment. The authors further applied LC-MS/MS to the metabolic pathway of this compound which indicated high reactivities and transformation rates. Van der Bent *et al.*[278] employed LA-ICP-MS in combination with µXRF to investigate allergic reactions caused by pigments in tattoo dyes in skin. Elemental imaging revealed the presence of Ti, Cr, Ni, Cu, Fe, Cu, Zr and Nb, and authors linked the allergic reaction to the presence of Ni.
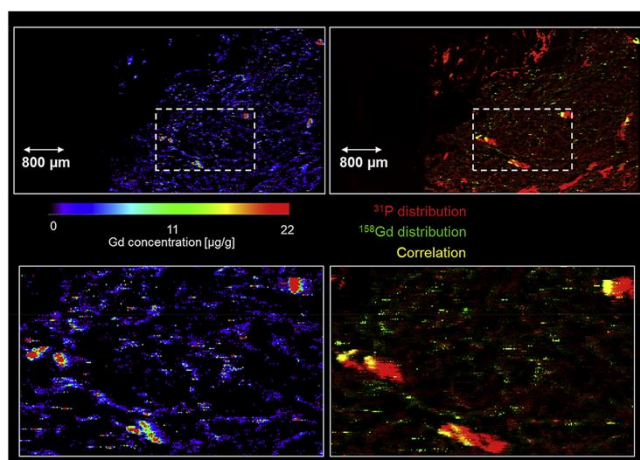
Figure 20: LA-ICP-MS/MS images of Gd (left) and P (right) in human nephrogenic systemic fibrosis skin tissue. Reproduced with permission from Ref. [274]. Copyright 2018 Elsevier.

The analysis of elemental accumulation in organs is usually connected with an invasive procedure to obtain the required tissues. Therefore, several studies evaluated investigating tissues which are easily obtainable such as hair, nails, or teeth to interrogate incorporated elements as a proxy to reveal past exposure events. The spatial resolution within these slowly growing structures is especially of interest for predicting the time and duration of exposure and contamination. Sela *et al.*[279] analyzed Zn, Fe, Cu, Cr, Pb and U hair samples and compared

analyses via LA-ICP-SFMS and ICP-MS, concluding that the lateral resolution is an important parameter that reflects environmental changes of individuals and has potential for exposure analyses and biological monitoring. Hasegawa et al.[280] presented a pilot autopsy study where the Gd concentration in hair was related to levels in other tissues. They found a high correlation between the concentration in hair and the white brain matter and dentate nucleus, suggesting that hair analysis was suitable as a non-invasive method for biomonitoring patients who were subjected to enhanced MRI examination with contrasting agents. Luo et al.[281] analyzed the distribution of As in hair from a leukemia patient treated with arsenic trioxide (As_2O_3; trade name Trisenox). Pozebon et al.[282] recommended a method to monitor the levels of Pt in hair after receiving platinum complexes post cancer treatment. Similarly, Stadlbauer et al.[283] discussed monitoring of heavy-metal intoxication from exposure to Pt and Hg intake. A further study by Abad et al. emphasized direct deposition of Hg from the environment must be considered to differentiate ingested Hg.[284] The analysis of hair by LA-ICP-MS was further investigated to monitor various essential and toxic elements to estimate dietary intake of animals.[285] Similarly, feathers and skin may be analyzed for trace elements from both external and internal contamination.[286, 287] Nails and other keratin rich structures are also viable targets of past exposures.[288] Hann et al.[289] determined the level of Tl in a thumbnail of an individual poisoned and killed in the 60s in Austria. The authors found a 170-fold increase of Tl levels and estimated the time (2-5 weeks) between the poisoning event and death based on the Tl pattern in the nail structure. Caumette et al.[290] analyzed the lateral distribution of As and I in horns of seaweed eating sheep. Seaweed is rich in As and I, and consequently, the distribution of both elements in the horn were correlated with dietary changes at different life stages.

The structural integration of elements into teeth has been investigated for more than 25 years. Evans et al. first employed LA-ICP-MS in 1995 to measure the distribution of Zn, Sr, Cu and Pb in teeth of walruses at different ages, and correlation of growth lines enabled the dating of past exposure events.[291] The analysis of heavy metals in deciduous teeth is useful to reconstruct the life-time lead exposure in children.[292, 293] Arora, Austin et al.[293, 294] used the neonatal line as a reference line to analyze the deposition of elements (Mn, Pb) during fetal development. Savabieasfahani et al.[295] found increased levels of Pb in deciduous teeth of children in war zones. Particularly high levels were found in children with birth defects. The

authors linked the increased Pb levels with contamination due to explosions, bullets, and other ammunition releases.

Other targeted structures to reveal past element exposure events include bones and otoliths. Fish otoliths are stable and durable structures that serve as a temporal biomarker for environmental monitoring and investigation of migration patterns.[131, 296, 297] Ishii *et al.*[298] analyzed bones of lead-exposed birds to measure the lifetime exposure of Pb. Bones had up to 90 % of the Pb burden (approx. 90%) and were correlated to levels in other soft tissues. In a study by Jackson *et al.*,[299] the authors evaluated a minimally invasive method to monitor the dietary-based exposure in water snakes (*Nerodia fasciata*) by sampling tail clips from three cohorts which were fed fish with varying levels of As, Se and Sr.

The possibility to apply elemental bioimaging to reveal past exposure events and to correlate element levels with biological traits opened new opportunities for LA-ICP-MS imaging. Several reports document application of bioimaging to analyze tissue remains and fossils.[300-302] The analysis of samples from animals and human individuals provided new perspectives in anthropologic and palaeontologic studies. Austin *et al.*[303] analyzed and compared Ba distributions in teeth from human children, captive macaques and a Middle Paleolithic juvenile Neanderthal. They were able to document the breast feeding and weaning pattern of the Neanderthal which consisted of seven months of exclusive breastfeeding followed by seven months of supplementation before an abrupt cessation of breastfeeding. Hair strands of ancient mummies were analyzed by LA-ICP-MS to investigate the exposure of different human populations to As,[304] Pb,[305] and Li,[306] as well as modern humans to As exposure.[307] Guede *et al.*[308] investigated the diet of medieval Muslim individuals from Tauste in Spain. They found significant differences in the elemental distribution in the dentine and enamel. As dentine remodels during the lifetime, elemental variations could be used as an indicator for the dietary intake of elements. Farell *et al.* analyzed Pb, Sr, Cn and Li in dental tissues of Chilean mummies and compared elemental levels to teeth from contemporary Egyptian children which were an order of magnitude higher.[309] They further compared the levels and distributions of Li and Zn, thought to be caused by increased environmental levels and prenatal exposures, respectively. Lopez-Costas *et al.*[310] used ICP-MS to analyze Pb and Hg levels and Pb isotopic ratios in ancient human bones to provide evidence of atmospheric

metal pollution of previous civilizations. They investigated a 700-year period in which rural Romans incorporated twice the levels of Hg and Pb into their bones than post-Romans inhabiting the same site. Maurer *et al.*[311] evaluated and compared LA-ICP-MS and ICP-MS for the elemental analysis of archaeological bones. They used Ca as internal standard and NIST612 and NIST610 as well as STDP-1500 to quantify P, Mg, N, Sr, Ba, Li, Zn, V and U. They noted that depending on the preservation state, biological and diagenetic elements may not be distinguished which may preclude the suitability of LA-ICP-MS to investigate the paleodiet.

The accumulation of exogeneous and endogenous elements is a complex process which leaves unique traces which depend on the individual physiology, the environment, and the exposed elemental species. As such, the incorporation of elements into durable tissues leaves a unique pattern which may be useful to identify individuals.[312] For example, Castro *et al.*[312] used LA-ICP-SFMS to analyze elements in bone and teeth for forensic purposes, and Stadlbauer *et al.*[313] attempted to employ LA-ICP-MS to confirm the authenticity of Mozart's skull. However, due to the heterogeneity of various tissue structures, unequivocal identification is difficult. Further forensic application of LA-ICP-MS comprise of the analysis of fibers, paper, food and objects/materials for identification or authentication reasons.[314]

5.6.   Neuroscience

A substantial amount of analytical research and development for LA-ICP-MS imaging was performed using neurological tissue as test samples.[315] The convenient size and structural heterogeneity of mouse brain sections were excellent targets to demonstrate principles of imaging in realistic time periods. There are relatively few published applications of solution nebulization ICP-MS for measuring elemental content of brain tissue before the turn of the century. ICP-MS was used as a detector for human brain proteins separated using capillary zone electrophoresis (CZE). Metals, specifically Zn, bound to metallothionein (MT) isoforms were detected in cytosolic fractions of post mortem tissue from aged control and Alzheimer's disease (AD) groups.[316] Concentrations of Cd, Co, Cu, Fe, Mn, Rb, V, and Zn were measured in digests of human tissue from diagnosed amyotrophic lateral sclerosis (ALS) and a rare, possibly related parkinsonism-dementia complex found in residents of Guam.[317] The authors reported an increase in brain Cd levels in ALS tissue, and Zn in both disease types, compared

to a control group, though very small sample groups and formalin-fixed samples give some caution. Formalin fixation has differential effects on tissue metal concentrations[318, 319] and should be considered with respect to imaging experimental design.

For example, Bonta et al.[320] examined the effects of formalin fixation and paraffin embedding of the sample on the distribution of elements in murine lungs and brain compared against fresh-frozen sections. Alkaline metal concentrations (Na and K) were drastically reduced, Mg and Ca somewhat reduced, whilst the transition metals (Mn, Fe, Ni and Zn) were less affected. The authors conclude that FFPE preparation renders the analysis of free metal ions unsuitable by LA-ICP-MS, and that transition metals distributions are comparable. However, the concentrations of Ca and Zn can be increased due to contamination by the fixation process and caution should be applied for interpretation. Similarly, Pushie et al.[321] reported that Zn was depleted from specific hippocampus sub-regions and enriched in white matter during sucrose cryoprotection and concluded that this method of sample preparation should be avoided for elemental analysis of murine brains containing labile metals.

Factors that likely influence the spatial distribution of metals and other mobile elements in neurological tissue include:

- The length of time a sample was immersed in a fixative. Samples can be archived in preservatives for decades with minimal structural degradation.
- The type of tissue being stored. Insoluble matrices like bone behave differently than lipid-rich brain tissue.
- Storage conditions under which the sample was held. Warm ambient temperature effects the mobility of more soluble elements.
- What chemicals were used to preserve the tissue. Like the biological matrix itself, the phase of solvent also influences solubility. For instance, pyridine was a common preservative for histological samples until the late 1900s.

In addition to each of these considerations, the comparatively unspecific nature of LA-ICP-MS is limited in terms of what information it can provide. Assuming that the 28 essential elements

necessary for life are found in the human brain, measuring a change in a single element is an otiose observation. The minor and "trace" elements may be present in small amounts, but they have an unknown number of possible conformations in the human proteome that is estimated to have around 9 million individual chemical species.[322] Therefore, it is important that LA-ICP-MS imaging is used within the context of a broad range of other analytical techniques used in neuroscience.

Becker led pioneering work in the early 2000s that supported later development of imaging methods used today. Gel electrophoresis was used to separate human brain proteins, and LA-ICP-MS then used to selectively sample separated protein spots in the 2D gels.[323, 324] The work logically evolved to imaging, and foundation studies were reported soon after. Rat brains with stereotaxically implanted tumor cells were imaged for Zn, Cu, P, and S on a SF ICP-MS with an effective resolution of 50 μm (**Figure 21**).[176] The relatively unimpeded masses at the high atomic weight range also leant themselves to investigation of naturally abundant elements as correction elements for signal drift. Graduating from animal models to human samples, Zoriy *et al.*[177] reported sub-part per trillion detection limits for Pb and U in three human glioblastoma samples. This work inspired subsequent and important research using human brain tissue to demonstrate the stability of LA imaging methods[325] that are still used in most laboratories today.
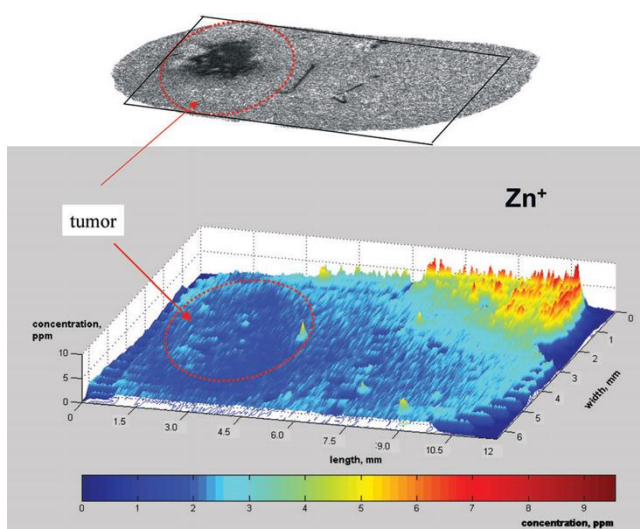
Figure 21: Oblique plane view of Zn in rat brain section. The area circled in red in the top ^{3}H-PK11195 autoradiography image depicts to the site of stereotaxic deposition of F98 cells. Reproduced with permission from Ref. [176]. Copyright 2005 Royal Society of Chemistry.

Much of the early development work involved the study of Parkinson's disease (PD) due to the long-standing association between the movement disorder and abnormal Fe disposition in the midbrain.[326] This brain region is normally highly abundant in Fe, where it mediates a range of biochemical processes that make use of the relative ease with which Fe atoms share electrons at normal pH.[327] Dopamine (DA) and Fe are normally chemically sequestered by a network of proteins and regulatory systems, though an apparent increase in oxidative stress in the PD brain follows the detectable accumulation of Fe in the substantia nigra pars compacta (SNc).[328-330] Hare *et al.*[331] used the 6-hydroxydopamine (6-OHDA) neurotoxin model of DA cell loss in mice to demonstrate how quantitative imaging of Fe following unilateral injection with the potent disrupter of mitochondrial function showed a post-lesion elevation in measurable Fe within the nigra. The strong response in Fe signal mapping the needle track was clearly visible 21 days post-injury, though no change in other metals indicated the tissue had healed (**Figure 22**) and Fe was suggested to likely be remnants of heme present following surgery. Similar results were seen with 3D reconstructions, with the needle track showing injection of the 6-OHDA toxin was made slightly above, and not directly into, the SNc.[141] Matusch *et al.*[332] used the same experimental paradigm to create multimodal images of metal and peptide distributions with LA-ICP-MS and MALDI-TOF-MS. There was evidence of damage at the site of the lesion in the mass fragments corresponding to oxidized lipid species and elevated levels of Fe. The same group had early shown that 1-methyl-4-phenyl-1,2,3,6-tetrahydropyridine (MPTP) toxicity similarly caused alterations in midbrain levels of Fe and Cu.[333] Like 6-OHDA, MPTP elicits a neurotoxic response in exposed animals, though it does not require direct injection into the brain[334] and therefore is not prone to possible interference in Fe levels from the injury path. It is important to note that both imaging and whole-brain digests have shown MPTP and 6-OHDA consistently reproduce the phenotype of increased Fe in the human PD brain,[335] though not the associated depletion in midbrain Cu.[336] The metal hypothesis of PD follows that decreased Cu and elevated Fe in the human SNc are an amplified effect of aging that lead to an environment rich in pro-oxidant Fe with a depleted supply of Cu to draw on to synthesize the Cu-binding superoxide dismutase-1 enzyme.[337]

However, increased Cu is often incorrectly described as a risk factor for PD, and even though it shares many chemical similarities when reacting with DA in controlled or theoretical environments,[338] the likelihood of these conditions being replicated in the human brain is not supported by direct experimental evidence from PD tissue.
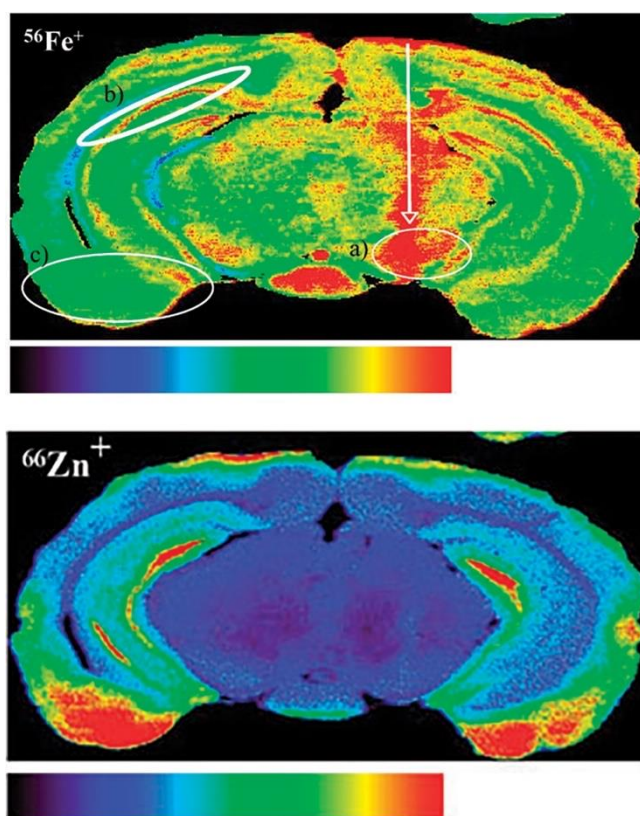
Figure 22: Fe in 6-OHDA lesioned brain tissue. The unilateral increase in Fe was seen in the SNc (marked as A; B = dentate gyrus; C = amygdala) with a corresponding elevation in Fe. No corresponding change was seen in Zn. Adapted with permission from Ref. [331]. Copyright 2009 Royal Society of Chemistry.

Of course, this does not invalidate such concepts, and is in fact essential when developing new therapeutics that directly target DA-metal chemistry.[339] Similarly, model organisms are not direct replications of human disease, though they are useful to examine a specific disease-associated pathway in isolation and with some degree of control over variables. A PD model has one feature in common: the specific depletion of DA-producing cells, and this can cause several measurable phenotypes. The term "parkinsonian neurodegeneration" is used to describe the progressive loss of dopaminergic neurons, though neurotoxins induce a rapid

development of symptoms compared to the years-long preclinical phase of human PD.[340] Imaging methods that have used parkinsonian models include 1,4,7,10-tetraazacyclododecane-1,4,7,10-tetraacetic acid (DOTA)- metal coded affinity tag (MeCAT) tagged imaging of PD-associated proteins in α-synuclein (α-syn) overexpressing mice;[341] imaging Fe and inflammation markers after 6-OHDA toxicity in rats;[342] Fe-loaded mice exposed to MPTP and the DA replacement therapy levodopa;[343] and MPTP-exposed mice treated with experimental drug candidates.[344] Examples of imaging of human tissue are more limited, primarily due to a shortage of suitable samples. Overt neurodegeneration occurs only in deep regions of the midbrain with an area not much larger than a thumbnail, and preserving the tissue that captures a chemical snapshot at the time of collection is impossible.[139] Interactions between Fe and DA are near-universally accepted as part of the molecular basis of PD, and DA metabolites that are known to both cause neuronal dysfunction and accelerate formation in the presence of Fe are specifically elevated in cells derived from human PD tissue.[345] Importantly, while the metabolites are common to both PD and the models used to replicate it, the levels are not. Human DA neurons contain much higher levels of DA compared to neurons from mice, including those genetically engineered to express human proteins involved in DA metabolism that are dysfunctional in PD. This has serious implications when using quantitative data to support a translational rationale for modulating DA levels in humans: the effects seen in animals and cell culture may be vastly different to human neurons that maintain a different resting state DA concentration.

Alzheimer's disease (AD) has had a logical connection to metals since the long-ago discredited theory that Al exposure induced the formation of characteristic neuropathological features of the disease. Even so, the scientific literature is rife with well researched but biophysically implausible accounts of Al causing protein aggregation and AD-like phenotypes in model organisms.[346] By and large this concept has been driven by *in vitro* experiments using enormous excess of both Al and disease-associated peptides that in no way represent the human condition. Metals have remained a lynchpin in the amyloid cascade hypothesis[347] and ferroptosis[348] models of AD, though extreme care should be taken interpreting metal levels as possible AD biomarkers given the likely association between certain metal species, age, and environmental exposure.[349, 350] Nevertheless, elegant longitudinal studies have shown that subtle changes in regional Fe concentrations occur across lifespan,[351] though the

estimated trajectories are based on a very high number of measurements and still show weak correlation that preclude any predictive utility on a case-by-case basis. Linking abnormal metal deposition in post mortem human brain to *in vivo* measures has obvious challenges, and it has been argued for some time that the field is guilty of publication bias with respect to metals actually being associated with AD.[352] Magnetic resonance imaging (MRI) can be used to produce indirect maps of Fe in the brain using lengthy and unpleasant scans, though directly associating quantitative Fe measurements with computerized tomography requires the scanned brain to be directly analyzed soon after.

It is also difficult to align MRI images with LA-ICP-MS data, as the orientation of samples change moving from one imaging mode to another. Tomography sections the images after data collection, whereas LA-ICP-MS requires samples be sectioned prior to analysis. This can be overcome by aligning fiducial markers, which conveniently often have a distinctive elemental signature that can be repurposed, such as Gd tracers used as contrasting agents. These do not correct for sheering and tearing of the sample when sectioned on a cryotome, though those with skills in computational neuroscience have shown how repeated measures can be used to "repair" structural damage from prior neurosurgical injections.[353] Hare *et al.*[354] used formalin-fixed paraffin-embedded (FFPE) human AD tissue to show that Fe was elevated in the grey matter of the frontal cortex of AD patients, though the authors stressed that samples were of different ages, were all preserved for different time periods, and had been stored at different temperatures for years prior to analysis. The value in this study was instead how endogenous P levels can be used as a proxy for the white/grey matter junction using much the same approach as MRI and histological staining of myelin. A similar approach was used by Stüber *et al.*,[355] who described proton-induced X-ray emission (PIXE) and MRI and claimed both Fe and myelin images could be estimated from the MRI data. With Fe present in lower levels in the cortex than midbrain structures, visualizing variation in the more diffuse network of gyri and sulci of human brain with MRI is more challenging, and contrast agents that can be cross-referenced with LA-ICP-MS are an exciting area of development.[356] Niehoff *et al.*[357] used LA-ICP-MS to measure Mn in brains scanned prior by MRI using an injected Mn^{2+} contrast agent, and while T_1 scans showed a general alignment with Mn LA-ICP-MS imaging (**Figure 23**), it is difficult to ascertain other sources of signal in the T_1 images.
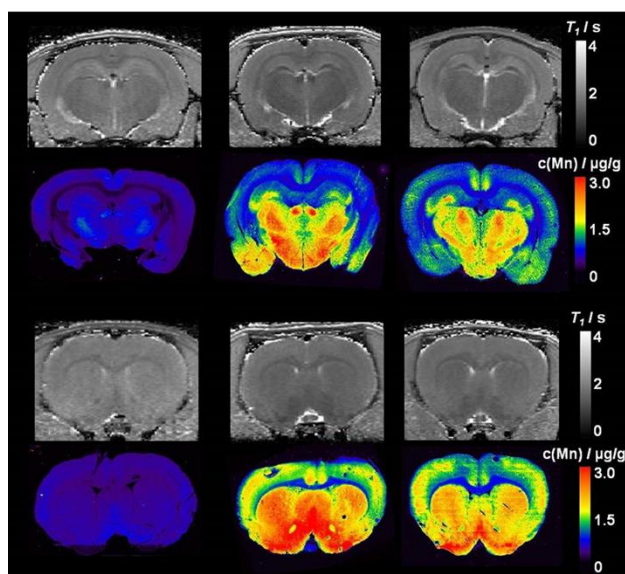
Figure 23: Untreated (left column) and MnCl$_2$-infused (middle and right columns) brains at bregma -3.3 mm (top row) and bregma (bottom row). Greyscale images are MRI and rainbow scale are μg g^{-1} Mn. Adapted with permission from Ref. [357]. Copyright 2016 WILEY VCH Verlag GmbH & Co.

LA-ICP-MS has unrivalled specificity, showing the distribution of all metal species regardless of chemical state or cellular compartment. Histochemical stains and MRI are both ambiguous measures of Fe; the former uses chemical dyes that normally react with only one chemical form (such as Perls Prussian blue staining of non-heme Fe), and the latter relies on detection of a signal that cannot be completely differentiated from interfering material (like myelin interference on Fe signal in cortical tissue). Chemical profiling of the entire Fe-binding metallome of the brain requires multiple analytical approaches to characterize all possible Fe species, including methods that can identify ferroproteins by molecular mass spectrometry[358] and estimate spatial redox state.[359] With each imaging mode added, a greater number of shared structural features can be used for alignment.

5.7.   Biomolecular Imaging

LA-ICP-MS also has utility for exploration of molecular features via immunohistochemistry (IHC) and a suitable elemental tag that may be used as a proxy to indirectly measure the target biomolecule. IHC is a qualitative bioanalytical technique that uses antibody (Ab)-antigen interactions to detect and visualize biomolecules. The presence of an antigen is measured

indirectly via a chemical reporter affixed to either a primary or a secondary Ab (the analyte in **Figure 24**). Typical IHC visualization methods use a chromogenic substrate linked to an Ab, or excitation of a conjugated fluorophore and detection of the fluorescence emission (immunofluorescence, or IF). Interpretation is limited to nominal (positive/negative) or ordinal values (low, medium, or high signal; usually reported as +, ++, and +++) of a characteristic test sample.[360] There are several limitations of IHC including difficult simultaneous identification of multiple biomolecules (multiplexing) due to a limited number of chromogenic agents and/or overlap of fluorescent emissions, and qualitative aspects limits interpretability especially when a target is modestly increased or decreased, and frequently requires a second complementary quantification strategy.
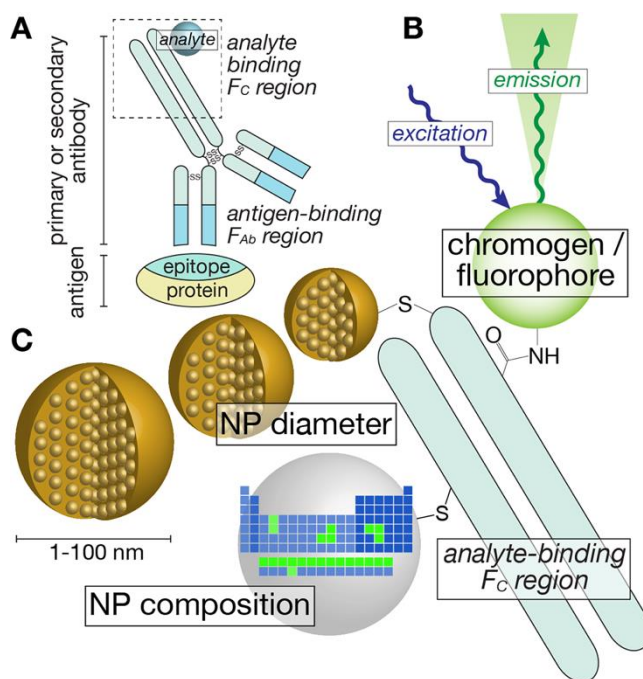
Figure 24: A) Analyte and antigen binding regions of IgG Ab. B) IF chemical reporters or C) metal NPs can be used as proxies for biomolecules of interest.

There are several commercial reporter elemental tags available including MeCAT kits, Au- and AgNPs, and Maxpar® polymeric tags. Lanthanides may also be bound in commercially produced complexing agents such as diethylenetriaminetetraacetic acid (DTTA) and 1,4,7,10-tetraazacyclododecane-1,4,7,10-tetraacetic acid (DOTA). Au- or AgNPs are appealing for IHC-LA-ICP-MS imaging due to low cost and commercial availability of pre-labelled 2° Abs. However, limitations include high Ag background from non-specific precipitation within tissue

sections, sub-optimal sensitivity due to poor ablation characteristics of Au, and limited feasibility for multiplexing. Lanthanides are ideal tags due low to negligible background signals with close to 100% ionization efficiency in the ICP. The choice of tagging protocol should consider the sensitivity that is required to visualize the target biomolecule as IHC-LA-ICP-MS is mainly dependent on the number of reporter elements per Ab. DOTA and MeCAT bind a single atom per tag, fully loaded Maxpar® polymer tags contain up to 30 atoms, and NPs may contain several thousands of atoms depending on their size and composition.[361]

In general, it is preferable to bind the elemental tag to a primary antibody to decrease the number of staining steps and to allow highly multiplexed analyses. There are several binding strategies possible dependent on the form of tag used. For example, NPs may be functionalized with streptavidin to form streptavidin-biotin bridges. Other NP binding mechanisms include simple hydrophobic interactions, covalent binding through maleimide or carbodiimide bonds and click chemistry.[362] Maleimide linkers, such as those used for the Maxpar® labels, covalently bind to sulfhydryl residues after partial reduction of the Ab disulfide bridges.[363] Other ligands such as SCN-DOTA bind to amino groups of lysine residues with improved preservation of Ab activity when compared with the covalent counterparts.[364] The next sections provide an overview of LA-ICP-MS molecular imaging with an emphasis on advances in instrumentation and tagging protocols for cellular or sub-cellular resolution.

The first use of IHC and LA-ICP-MS was in 2005 by Hutchinson *et al.*[365] who imaged amyloid (Aβ) in Alzheimer's plaques (**Figure 25**). A monoclonal Aβ antibody and a biotinylated secondary antibody were applied to consecutive sections of murine brain, with the first undergoing Ni-3,3'-diaminobenzidine (DAB) visualization and the second labelled with Eu-streptavidin, a commercial fluorescent agent. The plaques could be readily differentiated from non-plaque regions using both tags, however Ni had a higher background due to non-specific binding. Eu offered improved differentiation between regions of interest due to the increased specificity of the Eu-streptavidin protocol.
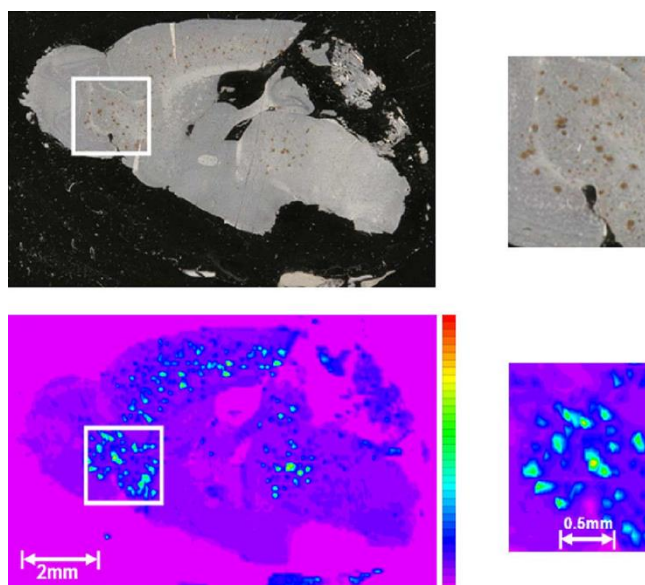
Figure 25: Light micrograph of chromogen enhanced Aβ stained mouse brain (top) and Eu image for tagged Abs (bottom). Reproduced with permission from Ref. [365]. Copyright 2005 Elsevier.

Seuma *et al.*[366] compared the use of Au- and Au/AgNPs as tags to quantitatively map MUC-1 and HER-2 cancer biomarkers in breast tissue sections. They calibrated their analysis by spiking known amounts of Au and Ag onto sections of rat liver with LODs of 0.01 ng Au and 0.005 ng Ag (3: 1 average signal to noise ratio). Jakubowski and colleagues conducted a 3-part investigation exploring various labelling methods for analysis of proteins as a model for future use on antibodies. Their initial approach used direct iodination of histidine and tyrosine residues of bovine serum albumin (BSA), pepsin and lysozyme on membrane blots of sodium dodecyl sulphate–polyacrylamide gel electrophoresis (SDS-PAGE) separations via a modified commercial radioimmunoassay protocol.[367] The I-tagged proteins were spatially quantified via LA-ICP-MS and construction of a 4-point calibration curve of BSA, which was limited to 3-orders of magnitude and an LOD of 0.15 pmol due to a high iodine signal in the blank. Their second approach investigated another radioimmunoassay label, SCN-DOTA.[368] Unlike iodination, SCN-DOTA has potential for multiplexing by chelation of isotopically enriched lanthanides as proxies for each individual target. Eu^{3+} was bound to SCN-DOTA before incubation with BSA and the resulting calibration curve was linear over 4 orders of magnitude with an LOD improvement to 15 fmol. Finally, they applied both SCN-DOTA and iodine labelling to antibodies raised against BSA, lysozyme and casein for analysis by LA-ICP-MS

81

imaging of a Western blot after SDS-PAGE separation.[369] The authors constructed a three-plex image of the Western blot by labeling anti-lysozyme, -BSA, and -casein with Tm, Ho, and Tb, respectively, resulting in clear signals of the targets, albeit with less sensitivity then direct labeling of the proteins. The iodine labelled antibodies were not suitable due to high levels of non-specific binding resulting in a high background. Similarly, Waentig et al.[370] investigated an alternative procedure for iodination of proteins using KI_3. This milder protocol improved the labeling of antibodies and, unlike the previous investigation, was useful for imaging casein and BSA on a Western blot. However, the SCN-DOTA labelling approach had superior signal-to-noise ratios. This iodination method was used by Giesen et al.[371] to label fibroblast cells and several tissue sections, where the I signal was proportional to tissue thickness and was suitable to act as an internal standard for imaging of HER-2 and CK 7 via Abs labelled with Ho- and Tm -DOTA, respectively. Here, the labelled antibodies were incubated against a breast cancer tissue section, followed by iodination, with the I signal accounting for variability in tissue thickness in the ablated regions of interest. This method was then further expanded by addition of Tb-DOTA labelled anti-MUC to the breast cancer biomarker panel.[372] Optimization of this first three-plexed analysis of tissue sections involved minimizing non-specific binding and maximizing signal-to-noise ratios via consideration of tissue thickness (5 μm), antibody incubation time and concentration (1 μg mL^{-1} for 3 h), laser energy (35%), laser spot size (200 μm), and laser scan speed (200 μm s^{-1}). The laser parameters provided adequate sensitivity to measure the expression of MUC 1, Her 2 and Ck 7, however, the resolution was 20 time less than that required for cellular resolution.

These early adopters of labelling antibodies for LA-ICP-MS detection provided the groundwork for further expansion of quantitative IHC-LA-ICP-MS protocols. de Bang et al.[373] developed a quantitative multiplexed Western blot LA-ICP-MS analysis of five plant thylakoid proteins via doping nitrocellulose blotting membranes with various lanthanide-DOTA labelled Abs. Calibration curves were constructed for each of the targets with lysozyme as an internal reference protein. The linearity was greater than 0.99 for each of the proteins with intermembrane %RSDs less than 5% (n=3), and intramembrane %RSDs less than 15% (n=12). The method had similar LODs as chemiluminescence, however the IHC-LA-ICP-MS method sensitivity was boosted by 20 times when the DOTA tag was replaced with a polymer tag with multiple lanthanide chelation moieties. Reifschneider et al.[374] introduced a non-targeted

method for LA-ICP-MS imaging of structural features by exploiting components in common histological agents. H&E are commonly applied to pathological sections to stain nuclei blue and cytoplasm pink, respectively, and underpins the visualization of tissue structures in routine clinical investigations. The authors imaged aluminum present in hematoxylin, and bromine present in eosin, to generate images of appendix, lymph nodes, fallopian tubes, and an esophageal tumor. In all cases the Al and Br signals were concordant with photomicrographs of the H&E stains and was useful to differentiate various cell populations and tissue structures. Exogenous metals were apparently unaffected by the staining protocol, allowing measurement of the distribution of Pt after application of chemotherapeutics.

Hoesl *et al.*[375] developed a simple calibration and internal standard (IS) procedure for IHC-LA-ICP-MS imaging using an ink-jet printer to print calibration standards onto Western blot membranes, and application of an IS layer over the sample using lanthanide-doped ink. The calibration curves had r^2 values greater than 0.999 for Er and Pr, whilst the IS was effective for mitigating signal drifts associated with varying laser power over the entire acquisition. The method was used to determine the concentrations of BSA, ovalbumin, and lysozyme following MeCAT tagging, SDS-PAGE separation and blotting onto nitrocellulose. Frick *et al.*[376] developed an alternative method for internal standardization by applying an Ir-labelled DNA intercalator to tissue sections. Although the IS only bound to DNA present in cell nuclei the IS was effective for resolutions greater than the size of individual cells and was suitable for normalization of signals with tissue thickness for 2 to 14 μm. As proof of principle, the Ir-intercalator was applied to a folded kidney section and immunostained with Maxpar®-labelled antibodies against E-Cadherin and histone H3. The Ir signal clearly tracked tissue thickness across the folded area and allowed correction of the thickness when quantifying the antibody labels against external standards prepared on cellulose acetate membranes.

Despite the excellent potential of this early literature, application of ICH-LA-ICP-MS did not improve on traditional IHC/IF investigations because the resolution was insufficient for cellular interrogations. Accordingly, Managh *et al.*[377] labelled regulatory macrophages (Mregs) with AuNPs for identification via LA-ICP-SF-MS. Using a low-volume ablation cell and an 8 μm spot size, individual Mregs were imaged from a culture replated into chamber slides. The AuNP labelled Mregs were then injected into mice and individual cells were detected in

sections from the lungs, liver, and spleen. Hare et al.[327] used Au/Ag-NPs to label anti-TH as a marker of dopamine in a murine parkinsonian model. Individual dopaminergic cells were observed with optimized LA-ICP-MS parameters including a 4 μm spot size, and a relationship between dopamine and Fe was identified in the mid-brain where Fe was suspected to facilitate free-radical reactions that result in neuronal cell death. Most of the later applications employed the superior sensitivity of Maxpar® labels and nanoparticles over single atom tags. Paul et al.[378] sectioned and imaged an entire murine brain, and quantified endogenous Fe, Zn, and Cu alongside a Maxpar®-conjugated anti-TH Ab with matrix-matched calibration standards. Mueller et al.[379] used a Ho-DOTA tag and a Ir-DNA intercalator to label free cell thiol groups and the nuclei of cells, respectively, and applied six Maxpar®-labelled Abs to identify specific targets for the analysis of single cells grown in culture. Quantification was performed via spiking elements at various concentrations onto a nitrocellulose slide to construct a calibration curve. Aljakna et al.[380] used Maxpar® labels to multiplex seven markers for myocardial infarction in post-mortem samples. Quantification was performed with spiked matrix-matched standards and traditional IHC was used for confirmation.

Cruz-Alonso et al.[381] used carbodiimide chemistry to bind AuNP analytes to primary antibodies to spatially determine the expression of MT in retinas, and ferroportin in the hippocampus. IF imaging was used to optimize the antibody concentration and dilution of the anti-metallothionein Ab via inherent fluorescent of the AuNPs. Cu and Zn LA-ICP-MS images were obtained alongside the Au as potential additional markers of metallothionein, however no correlation between Au and the endogenous metals was observed. The method was then extended to quantitative analysis by calculation of the number of moles of Au in each AuNP and the Ab/AuNP ratio, and preparation of calibration standards from Au-doped gelatin. No differences were observed between Au salts and AuNPs when investigated for use in the calibration standards. Alonso et al.[382] quantitively imaged ferroportin (FPN) and Fe in hippocampal sections from AD brain samples and compared against healthy control brains. No clear correlation was seen between Fe and FPN, however Fe was increased in the sections obtained from AD samples.

Other IHC applications use quantum dots in the 2-10 nm range. These probes are used in fluorescent bio-imaging applications and often contain elements that are amenable to LA-ICP-

MS imaging. Vanechova *et al.*[383] used peptide linkers to label CdS quantum dots to an anti-IgG Ab for subsequent analysis by LA-ICP-MS. McInnes *et al.*[384] assessed the suitability of a positron emission tomography (PET) Cu-complex for LA-ICP-MS imaging of Aβ plaques. They altered the ligand backbone of the complex which resulted in improved metabolic stability and ability to cross the blood-brain barrier and incorporated isotopically enriched Cu^{65}. Neumann *et al.*[341] developed a multiplexed IHC-LA-ICP-MS method to investigate neurological markers in a murine parkinsonian model brain. Six neuronal antibodies were labelled with MeCAT-bound with different lanthanides and were incubated in parkinsonian mouse model. The samples were coated in gelatin and an internal standard was printed using the inkjet printing method previously described.[375] Lores-Padin described multiplexed markers of age-related macular degeneration (AMD), MT 1/2, complement factor H, and amyloid precursor protein in eye sections.[385] Antibodies for these three targets were respectively labelled with AuNPs, AgNPs, and PtNPs and the NP/Ab ratio calculated for quantification via gelatin standards. The labelled antibodies were applied to AMD samples where accumulation was observed in subretinal drusenoid deposits and anomalous aggregates.

5.8. Imaging Mass Cytometry

Imaging Mass Cytometry™ (IMC) is a commercial IHC-LA-ICP-MS offering from Fluidigm that was designed to image molecular biomarkers in tissue sections using Maxpar® tagged Abs. The Fluidigm Hyperion™ system consists of a LA-ICP-TOF-MS equipped with a solid-state laser with a shot frequency of 100 or 200 Hz, a single spot size of approximately 0.71 µm², a scan speed of 100 pixels per second, and a low dispersion ablation chamber with a sampling area of 15 x 45 mm. IMC is used for highly multiplexed investigations of biomarker expression and was first reported by Giessen *et al.* in their 2014 paper that demonstrated the simultaneous imaging of 32 proteins at subcellular resolution.[386] The workflow required seven distinct steps (**Figure 26**): sample preprocessing using standard IHC protocols (including de-waxing of formalin-fixed paraffin-embedded sections and antigen retrieval prior to incubation with labelled Abs; air drying; laser ablation by line scanning or spot by spot; and transfer of the ablated material to the CyTOF. After ablation, the individual signals from the lanthanide tags were extracted and processed to assemble an image, followed by application of an algorithm for single cell segmentation, and finally data visualization using spanning-tree progression

analysis (SPADE). Single cell segmentation was performed with a watershed algorithm to identify sub-cellular variations and to explore tissue microenvironments. Watershed segmentation is based on topographic natural boundaries between ridges of high intensity, the watersheds, and basins of low intensity.[387] In the case of cells, membrane markers delineate these ridges away from the cytoplasm, or basin. The authors used three known membrane markers of breast cancer, β-catenin, HER2, and cytokeratin 8/18, to identify single cells by overlaying membrane and nucleus images that maximized cell-boundary demarcation. This process required visual inspection of all cell boundaries for correction, as necessary.
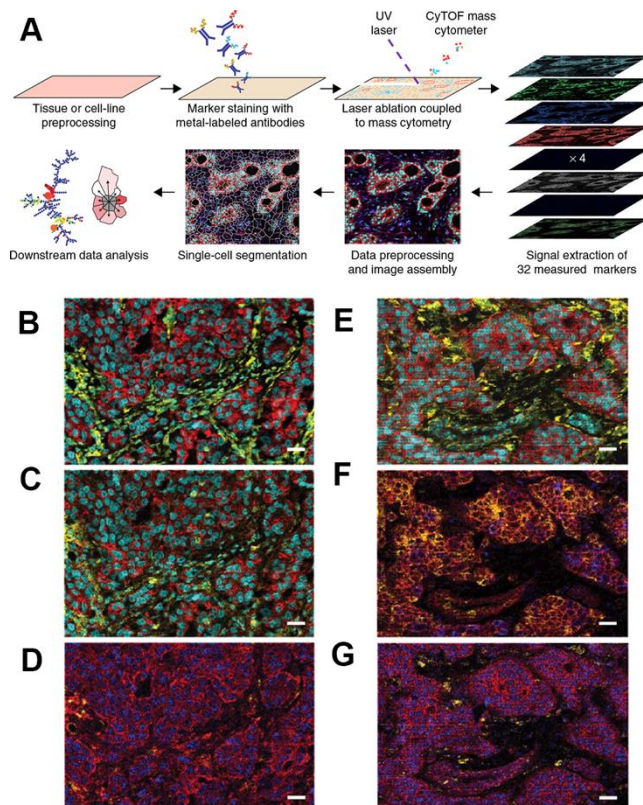
Figure 26: A) IMC workflow using lanthanide-tagged Abs. Mass cytometry images of luminal HER2+ breast cancer tissue samples. (B-G) Overlaid three-channel images of labelled cancer biomarkers from the 32-reporter panel. See Giessen *et al.*[386] for full list of tagged antibodies. Adapted with permission from Ref. [386]. Copyright 2018 Springer.

Schueffler *et al.*[388] further optimized the watershed algorithm using a nuclear marker and multiple automatically selected membrane proteins to visualize natural boundaries between

cells. Spearman's ranking was used to statistically identify four membrane protein markers to construct segmentation masks. The nuclear marker was used to ensure that the segmentation masks did not cross cell nuclei and that each segmented cell contained one nucleus. This multiple marker watershed single-cell segmentation algorithm was incorporated into the IMC HistoCAT software.[389] Here, the segmentation extracts single-cell data including the abundance of each marker, spatial features, and cellular environment including cell neighbors and crowding. This enables the analysis of cell-cell interactions described as "social networks" of cells.

Schulz *et al.*[390] extended IMC to include mRNA targets for in-situ investigations of transcription, protein expression and protein modification in a single analysis. mRNA probes for HER2, CK19, and CXCL10 were modified with lanthanides for detection and were multiplexed alongside antibodies for 16 protein and phosphorylated protein targets and applied to breast cancer samples. The mRNA probes were validated in HeLa cells and were concordant with fluorescence *in situ* hybridization (FISH) measurements. There was a good correlation between HER2 mRNA and protein expression, CK19 exhibited patient-dependent heterogeneity, and CXCL10 correlated with T cell presence in the tumor microenvironment. Strauss *et al.*[391] determined the analytical figures of merit of the Hyperion™ system using slides coated with metal doped PMMA film. The RSD of the mean signals was less than 15% when 400 x 400 μm sections of the PMMA film were ablated. Calibration curves were constructed by preparing five slides of different concentrations from 1.4×10^3 to 3.2×10^7 atoms per μm^2 of ^{151}Eu, ^{153}Eu, and ^{175}Lu. Correlation coefficient values greater than 0.999 were obtained for all elements, and LODs were estimated to be 915-1480 atoms per μm^2, corresponding to antibody LODs of 229-370 Abs per cell (assuming each Ab contained 100 metal atoms). Hoetzel *et al.*[392] developed an alternative quantification strategy by doping protein gels with target antigens to create a standard microarray with a range of antigen concentrations. This low cost, reproducible approach used routine histology methods and antigens from whole proteins, recombinant proteins, and small peptides. The quantification protocol was first applied to standard IHC with DAB precipitation before application to IMC where they determined a ratio of approximately 340 antibody molecules per detected lanthanide ion. This approach provided direct quantification of the antigen and overcomes variations in day-to-day immunohistochemical steps and antibody dilutions; however,

87

antigens are not readily available for many targets, and the method cannot compensate for non-specific binding in tissue sections.

IMC has provided complementary and unique insights for the investigation of immune responses in various organs. For example, Zhao *et al.*[393] investigated memory B cells and marginal zone B cells in human gut lymphoid tissues. They found that the memory B cells and the marginal zone B cells occupied unique niches in the lymphoid tissue, and were therefore not developmentally contiguous nor analogous. IMC was a key technology to investigate the role of dendritic cells in renal inflammation, where it confirmed differences in the expression of dendritic cells observed by multiphoton microscopy.[394] IMC was also applied to localize tonsil CD14+ macrophage in B cell follicles by Durand *et al.*[395] to investigate the polarization of follicle helper cells by dendritic cells and macrophages. Li *et al.*[396] found that memory-like CD4+ T cells colocalized with antigen-presenting cells in human fetal intestines, and further investigation characterized and determined the location of immune cell clusters in fetal liver, spleen, and intestine.

Damond *et al.*[397] used IMC to provide a comprehensive, spatial investigation of the impact of Type 1 diabetes (T1D) and autoimmune assault on insulin-producing β cells in the islets of Langerhans. Pancreas tissue was obtained from four control donors, four at T1D onset, and four with long term T1D, analyzing a total of 1581 islets. β cells were heterogeneously distributed in these islets, with two of the early-onset T1D samples containing β cells at levels approaching the controls. β cells were rarely observed in islets from the long-term cohort. They examined the evolution of the islets through T1D progression and found that many of the recent-onset islets contained near-normal fractions of β cells, however, their phenotype changed prior to destruction. They also investigated interactions between islet cells and immune cells and found that some islets containing many β cells recruited cytotoxic and helper T cells during T1D onset.

Multiple sclerosis (MS) is characterized by an inflammatory response in the brain. Park *et al.* [398] showed proof of principle of multiplexed IMC to discriminate between types of MS lesions. They first validated IMC against IF on consecutive sections, with the two techniques showing a similar number of cells and staining patterns and distinct anatomical regions. Multiplexed

IMC delineated different phases of lesions and normal tissue via visualizing of myelin and human leukocyte antigens. They differentiated infiltrating macrophages from the resident microglia and identified phenotypes of T and B cells. Demyelinating macrophages were located near blood vessels in active demyelinating areas and at the edge of active-inactive demyelinating lesions. Non-demyelinating macrophages, as well as T cells were found in distinct clusters enriched within active-inactive lesions. Theil *et al.*[399] used IMC, flow cytometry, IHC, ISH, and transcriptome analyses to track changes in lymphocyte subsets in blood and lymphoid tissues of cynomolgus monkeys treated with mAbs developed to deplete B cells in MS. The treatment functioned as expected with a rapid depletion of all B cells, with some T cells showing similar behavior. IMC was used in conjunction with IHC to determine location of B and T cells in the lymph nodes and identified a sub population of T cells in the periphery of B-cell follicles.

The inter- and intra-cellular information in highly multiplexed images, along with neighborhood analyses, lends itself well to cancer microenvironment profiling. Aoki *et al.*[400] used IMC in conjunction with scRNA-seq and IHC to characterize immune cells in classic Hodgkin lymphoma. Several T cell subpopulations and enrichment of LAG3+ T cells were observed and spatially confirmed by IMC with sporadic density increases in the same location as the tumor cells. Xiang *et al.*[401] used IMC to validate correlations between cancer-associated fibroblasts and monocytic myeloid cells in the tumor microenvironment of lung squamous cell carcinoma. This relationship was first identified by searching for expression of RNA sequencing data of 501 patients in the Cancer Genome Atlas data set.

Batth *et al.*[402] used IMC to characterize markers for identifying rare circulating tumor cells of osteosarcoma in model and patient derived cell lines, and in circulating tumor cells extracted from patient blood. From a panel of 17 Abs, they identified markers of circulating tumor cells in the model cells as well as cell surface vimentin (CSV) heterogeneity, with CSV+ cells showing statistically significant differences in smooth muscle actin expression compared against CSV- cells. Furthermore, CSV+ cells influenced protein expression in neighboring cells. The extracted circulating tumor cells were also positive for CSV, with variability seen in the other markers. It was also noted that IMC did not have the resolution to fully determine the subcellular location of these markers due to poor nuclear staining and non-specific binding.

Ali *et al.*[403] used IMC in conjunction with genomics on 483 breast tumor samples to determine how genomic alterations shape breast tumor ecosystems. Here, a panel of 37 antibodies were measured, single cells segmented, protein expression per cell noted, and neighboring cells examined. The resulting data set was used to classify cell phenotypes with clearly distinguishable fibroblasts and myofibroblasts. They also identified T cells, B cells, macrophages, endothelial cells, myoepithelial cells, and vascular smooth muscle cells. Substantive variation was observed between the IMC determined phenotypes when compared against bulk gene expression of each tumor. However, there was improved correlation when miRNA was observed with a subset of stromal phenotypes. When comparing cell phenotype distribution with genomic subtypes of breast cancer, epithelial cell phenotypes were enriched in certain genomic subtypes, which was consistent with previous observations. They also found differences in epithelial and stromal phenotypes, T cells and macrophages, and cell-cell interactions in different cancer subtypes. Furthermore, somatic genomic alterations were proposed to influence the composition of tumor cells and their microenvironment.

Jackson *et al.*[404] conducted the most in-depth analysis to date, using IMC and a panel of 35 antibodies to characterize the phenotype of tumor and stromal cells in tumor tissue from 352 patients with breast cancer covering all clinical subtypes and grades of pathology, with long-term survival data for 281 of the patients. They identified the expression of marker genes and spatial features in 855,668 cells. The phenotypes included endothelial, T and B cell, macrophage, stromal cells, and 59 diverse cell phenotypes, with some of these unique to a patient. Hierarchical clustering was used to identify 14 tumor metaclusters of common cellular subtypes. Neighborhood analysis was performed to identify regional correlations between these cellular metaclusters. Tumor cell phenotypes showed very little correlation, heterotypic interactions were associated around structural features such as blood vessels, and the neighborhood analysis showed interactions that distinguished tumor architectures related to tumor grades scored by a pathologist. Community detection showed that tumor groups were mostly dominated by a single cellular metacluster. Unsupervised clustering was used to group patient tumors based on the composition of their tumor cell metacluster and identified 18 single-cell pathology subgroups that split the clinical subtypes. Individual single-cell pathology subgroups had distinct clinical outcomes when compared to all other patients,

subgroups of the same clinical classification, and subgroups with similar cellular metaclusters but different architectures. They then mapped the cellular spatial organization of these tumors and found that patients with tumors with spatial phenotypic heterogeneity had poorer outcomes. Hierarchical clustering of the stromal microenvironments identified 11 groups with distinct cell-cell interactions within each environment. These stromal environments were associated with the singe-cell pathology subgroups and specific tumor cell phenotypes. Finally, they investigated the reproducibility and spatial variability of these subgroup classifications on a second independent cohort of 72 patients, with images containing a total of 411,410 cells. All cellular metaclusters and single-cell pathology subgroups were present in the second cohort, and 40% of tumors had a single classification in all regions, with 60% containing regions that did not agree with the tumor classification, and in most cases the single-cell pathology classification of individual regions matched the tumor-wide classifications. These findings indicated that single-cell pathology may assist prognosis beyond what is capable with contemporary classifications.

Ijsselsteijn *et al.*[102] developed a 40-member Ab panel that included markers for lineage and functional immune cells, surrogates for the states of the cancer cells, and structural markers for characterizing cancer microenvironments and cancer-immune cell interactions. This large number of markers presented several challenges of Ab staining, requiring an optimized workflow consisting of two separate antibody incubations with different temperatures and times to improve detection. Each antibody was individually assessed by IHC and DAB visualization, and each Maxpar®-labelled antibody was applied individually. Initially, incubation of 65 antibodies were examined under low pH and high pH antigen retrieval conditions, with 58 antibodies selected for further application under low pH antigen retrieval regime. Eight antibodies that performed well with IHC were excluded from the IMC panel as the signal from these low-abundant markers could not be readily observed. Several Maxpar®-labelled antibodies were not seen by standard IHC, with the conjugation process thought to affect the antibody binding domains and were therefore excluded, limiting the panel to 40 markers. Application of the entire panel to sections with an overnight incubation at 4°C resulted in some of antibodies presenting low signal and/or high background in comparison to the IHC images. Each antibody was then individually incubated on tissue sections overnight at 4°C, or five hours at room temperature. The signal for the low-abundant antigens was

superior with the room temperature incubation, while the signal was optimized for high abundant antigens with overnight incubation at 4°C. The final protocol required three days for deparaffinization, antigen retrieval, and antibody incubation of all 40 markers. The final panel was applied to colorectal cancer tissues with many immune cells detected.

Guo *et al.*[405] developed a panel of 34 antibodies of immune and structural markers for use on fresh-frozen fetal and adult intestinal samples (**Figure 27**). Initially, application of 80 antibodies and associated variables including tissue drying time, fixation, and antibody incubation times were optimized. Three drying conditions were examined, 3 min at room temperature (RT), 30 min at RT, and 1 hr at 60°C. Fixation protocols included 5 min methanol at -20°C, 5 min 1% paraformaldehyde (PFA) at RT, 5 min 1% PFA followed by 5 min methanol at 20°C, 10 min acetone at RT, 5 min 4% PFA at RT. Antibody incubation at RT was compared against overnight at 4°C. The initial panel of 80 antibodies was reduced to 43 based on IHC that displayed a clear signal-to-background ratio and was further reduced to a final panel of 34. All drying conditions were suitable for IMC based on image quality and signal for each antibody. Acetone fixation was recommended; however, the nuclear and antibody staining was not adequate when each antibody was individually applied. No one fixation method was optimal for all targets. Methanol or 1% PFA followed by methanol alone provided the best compromise. Optimal incubation conditions were determined by signal intensity and specificity of each antibody, and a maximum signal threshold for select antibodies. Most antibodies performed similarly under each condition, however there was greater variability in the maximum threshold values, and a higher background were observed, at RT. Therefore, the overnight incubation at 4°C was selected. Finally, an optimal protocol of tissue drying for 1 hr at 60°C, followed by 5 min 1% PFA followed by 5 min methanol at -20°C fixation, and overnight incubation at 4°C was applied to intestinal samples, with clear tissue structure observed along with lymphoid and myeloid immune cell subsets.
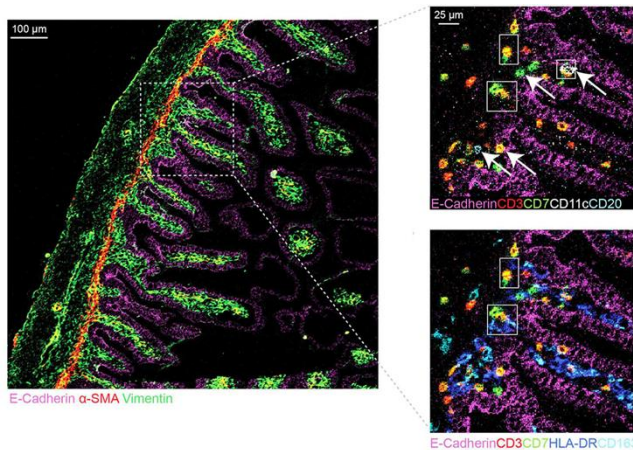
Figure 27: Multi-channel image of Maxpar®-labelled Abs in human fetal intestinal tissue. In total, 10 channels must be represented within the restraints of available colors that can be easily discerned by eye. Adapted from Ref. [405]. Licensed under CC BY 4.0.

Flint *et al.*[406] used desorption electrospray ionization (DESI)-MSI, IMC, and conventional LA-ICP-MS imaging to characterize a novel three-dimensional lung adenocarcinoma model created by aggregating spheroids to better represent the heterogeneity of cancers. The aggregated spheroids were grown to approximately 1 mm diameter before cryosectioning for analysis. DESI-MSI identified major metabolites of glycolysis and the TCA cycle in the hypoxic core, where the anaerobic conditions promote glycolysis, and glutaminolysis was evident in the outer proliferative regions. Linoleic acid and arachidonic acid were located within the outer region of the spheroid appearing to colocalize with glutathione, a metabolite that protects against ROS, suggesting an area of high metabolic activity. IMC of markers of proliferation and hypoxia confirmed necrosis occurring in the core, that the outer region was proliferative, and that glycolysis was occurring in the inner hypoxic region. The endogenous elements Mg, Cu, and Zn were measured by LA-ICP-MS. Mg and Zn are essential to cell growth and proliferation, and accordingly were found in the outer region. In contrast Cu was found in the hypoxic core, thought to have been imported to assist in preventing the formation of ROS.

IMC may also provide information on the response of cancer to therapeutic interventions for greater interrogation of the cellular response to a drug in a single measurement. Bouzekri *et al.*[407] screened breast cancer cell lines, HCC1143, SKBR3, and MCF-7, stained with 14, 20, and 25 Ab panels, respectively. The cell lines were characterized by surface heterogeneity, and

intracellular and nuclear markers. MCF-7 cells were exposed to etoposide, nocodazole, or epidermal growth factor, with a correlation in nuclear markers in mitotic cells and an inverse correlation with cell surface markers observed after treatments. Carvajal-Hausdorf et al.[408] developed an 18-Ab panel to multiplex the measurement of the intracellular and extracellular domains (ECD) of HER2, signaling proteins, and T-cell infiltration in biopsies taken from breast cancer patients treated with trastuzumab. They confirmed previous IF findings that breast cancer tumors that do not express the ECD of HER2 are less likely to respond to trastuzumab, and provided further information on the role of the immune system in the mechanism of trastuzumab action by demonstration of an association between CD8+ T cells and the ECD of HER2.

Bassan et al.[409] developed a novel compound, L-2-tellurienylalanine (TePhe), a Te-containing analog of phenylalanine, as an IMC probe to investigate protein synthesis. TePhe was incorporated into protein synthesis in place of phenylalanine via supplementation of the incubating cell culture. **Figure 28** shows an IMC image of TePhe-incorporation into a mouse jejunum stained with a DNA intercalator and Maxpar®-labelled anti-alpha smooth muscle actin, with a stronger Te signal observed in the crypts than the villi. Bassan and Nitz[410] further optimized the analysis of Te-probes by developing protocols for removing overlap with the Te signal, and combining Te isotopic signals to improve signal-to-noise. Here, the authors assembled a three-dimensional stack of all isotopic images of Te and applied a Gaussian blur filter to reduce noise.

Rana et al.,[411] noting the reduced sensitivity for low-abundant antigens due to the lack of signal amplification, developed an enzyme amplification strategy by incorporating tellurophene into alkaline phosphatase deposition using standard IHC protocols for application and detection of secondary antibodies. The reagent had a higher background signal than a comparative Maxpar®-labelled secondary Ab, however it had a 100 × higher signal for detection of low-abundant antigen. The novel reagent also showed applicability to a multiplexed IMC analysis, with four Maxpar®-labelled primary antibodies, one unlabeled primary antibody detected by the Te-AP precipitate, and an Ir-DNA intercalator applied to HCT116 xenograft tumor section. The reagent did not perturb the binding or the signal intensity of the Maxpar®-labelled antibodies or the intercalator. Yu et al.[412] developed a

metal-labelled aptamer nanoprobe by conjugating polymeric 167Er-DTPA to an RNA aptamer, A10-3.2, via maleimide coupling to target prostate specific membrane antigen in prostatic adenocarcinoma. The images were concordant with a Maxpar®-labelled antibody, with the aptamers providing 3x higher signal than that of the Abs. This was most likely due to the smaller aptamer probes accessing binding sites inaccessible to the larger antibodies. Finally, they developed a multiplexed aptamer analysis by conjugating a 176Yb-DTPA to ΔPsap4#5, which targets prostate specific antigen, and showed the distribution of these two epithelial cell biomarkers in prostate cancer tissue sections.
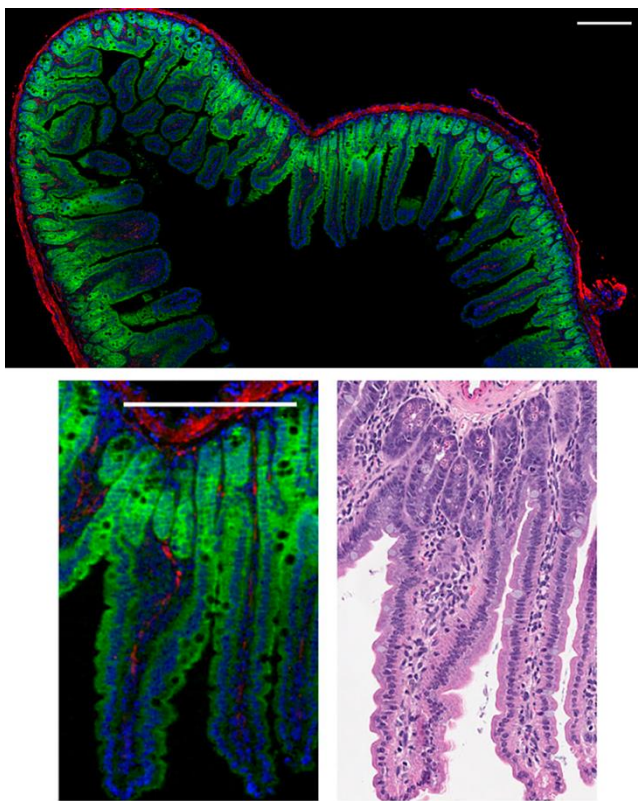
Figure 28: TePhe visualization of protein synthesis in mice. Top: IMC image of a mouse jejunum showing TePhe (green), DNA (blue), and α smooth actin (red). Bottom: Zoomed imaged and matching H&E micrograph. Scale bar 200 µm. Adapted from Ref. [409]. Copyright 2019 National Academy of Sciences.

Singh *et al.*[413] used a 23-Ab panel containing structural and infiltrating cell markers to create a spatial baseline atlas of a healthy human kidney. They developed a data analysis pipeline using machine learning to perform single-cell segmentation and phenotyping, which defined the number and organization of renal cell types, and their heterogeneity. Each antibody was

95

selected by a renal pathologist blinded to its identity after IF, chosen based on positive staining in expected cells and the morphological characteristics of the stained cells and/or regions. The antibodies were then labelled with Maxpar® reagents and examined in groups of 2-5 to ensure that the specificity of binding was unaffected. 16 kidney samples were obtained with no or minimal histopathological abnormalities to establish baseline relationships between cell types in the cortex and medulla, with a high variability of proximal tubules observed in the medulla. 13 cell types and 22 cellular populations were identified, 5% of cells unidentified, and morphological features such as the vasculature and location of immune cells also identified.

Warren *et al.*[414] developed a panel of nine mitochondrial proteins to probe skeletal muscle fibers in biopsies from patients with mitochondrial disease from deficiencies in oxidative phosphorylation. IMC was compared against IF imaging on serial sections, demonstrating comparable staining patterns and subcellular distribution. IMC had good inter-batch variation; however, a larger intra-batch variation was observed, which may be a result of differences in antibody yield and/or degree of Maxpar® labelling per reaction. Patients with mtDNA mutations exhibited spatial heterogeneity of biochemical deficiency in the muscle fibers, and patients with the same mutation had different levels of oxidative phosphorylation proteins, whilst each mtDNA variant required a different threshold of mtDNA mutation before oxidative phosphorylation occurred.

6. IMAGE PROCESSING AND ANALYSIS

A plethora of software options, both commercial and open source, are available for data reduction and image reconstruction, and have recently been comprehensively reviewed by Weiskirchen *et al.*.[415] Regardless of the choice of software, the main emphasis has been to process raw datasets into manageable file structures that can be easily visualized for interpretation and interrogation of regions of interest that reflect a biological response due a disease state or other stimulus. When compared to mature imaging techniques such as MALDI or standard IF imaging, examples of post-acquisition data processing in LA-ICP-MS imaging is somewhat limited and has been restricted to methods of improving image quality, particularly

in relation to resolution, feature selection and identification of regions of interest, and 3D reconstructions.

6.1. Feature Selection

Methods of feature selection aim to segment anatomical features within tissue sections and often relies on visual inspection of regions of interest determined from serial H&E, immunofluorescent, brightfield, and/or reference atlases. For example, Hare *et al.*[327] demonstrated that the colocalization of Fe and dopamine (as AuNP-labeled TH, which is the rate-limiting factor in dopamine metabolism) within the SNc of mice raises the risk of parkinsonian neurodegeneration in the aging brain (**Figure 29**). The Allen Brain Atlas[416] (Plate 81, bregma -2.78 mm) was consulted to demarcate the mesencephalic architecture in serial brain sections. Following manual overlays of a combination of reference traditional IHC and *in situ* hybridization (ISH) images of the expression of TH, and concomitant LA-ICP-MS imaging of Fe and Au labelled anti-TH as a proxy measure for dopamine, the authors reported that the product of the concentrations of dopamine and Fe was substantially higher in the SNc when compared against neighboring neuroanatomical structures. The elevation of the dopamine-Fe product was also confirmed in a 6-hydroxydopamine lesioned mouse model of parkinsonian cell death in the SNc and provided evidence of direct association between Fe and dopamine in the mechanism of cell death in PD. The same group have used the Allen Brain Atlas for feature selection in examples of 3D reconstructions of murine metal neuroanatomy.[378, 417]
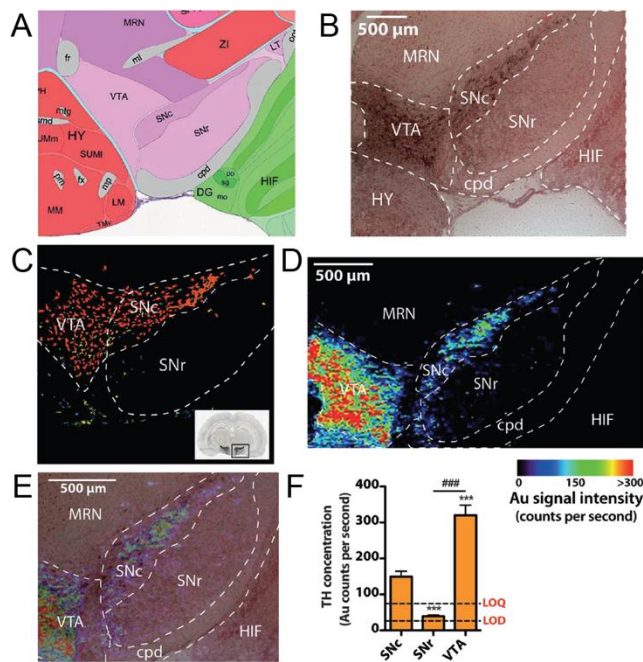
Figure 29: Assisted manual feature detection using biochemical proxy. A) Reference plate from Allen Brain Atlas. B) Annotated TH-immunostained, Nissl counterstained section at corresponding coronal level. C) Fluorescence *in situ* hybridization image of TH mRNA distribution (also from Allen Brain Atlas). D) Au image of AuNP-labeled anti TH antibody staining in section adjacent to (B); overlaid in (E). TH concentration (as measured [197]Au signal) reflecting variable enzyme activity and dopamine synthesis in the SNc, SN pars reticulata (SNr) and ventral tegmental area (VTA). Adapted from Ref. [327]. Licensed under CC BY 3.0.

Efforts to automate selection of such features consist of application of segmentation algorithms that are commonly used in traditional image processing. Approaches applied to LA-ICP-MS imaging may be separated into various broad categories: k clustering, and calculation of local and global thresholds. K clustering uses an unsupervised algorithm to partition unlabeled data into k-number of groups based typically on the mean or median. Segmentation using k-means clustering begins with the construction of clusters by selection of k random centers. The success of segmentation relies on the correct selection of k as small variations often result in poor outcomes. There are two common approaches to settle on the value of k: the elbow method, which requires manual selection, and the Bayesian inference criterion, which is prone to overestimation.[418] Local segmentation methods examine the signal standard deviation at adjacent pixels to calculate localized thresholds to segment the image into positive and background regions.[419] Global approaches apply a binary filter to

ascertain positive or negative pixels using a threshold value calculated from the entire image.[420] The three approaches are all commonly used in medical imaging and microscopy, and can be adapted for use in LA-ICP-MS bioimaging with relative ease.

Oros-Peusquens *et al.*[421] used k-means clustering to identify anatomical regions of a healthy rat brain and areas of necrosis in a photothrombosis stroke mouse model. k-means clustering was performed using unquantified and unweighted signals for C, P, Fe, Cu, Zn, Pb, and U, all of which had a high signal to noise ratio. The clustering algorithm identified several anatomical structures in the healthy rat brain including the bulbous olfactorius, layers of the cortex, white matter, plate of four collins, grey matter, the hippocampus fascia dentata and the cornu ammonis (**Figure 30**). A similar cluster analysis revealed areas of necrosis in the stroke model. The authors concluded that this simple algorithm was an effective method to segment anatomic structures and identify element accumulation in lesions induced by photothrombosis. Paul *et al.*[378] used a more advanced iterative c-means fuzzy clustering algorithm to independently identify mouse neuroanatomy by hierarchical classification using P, Mn, Fe, Co, Cu, and Zn.
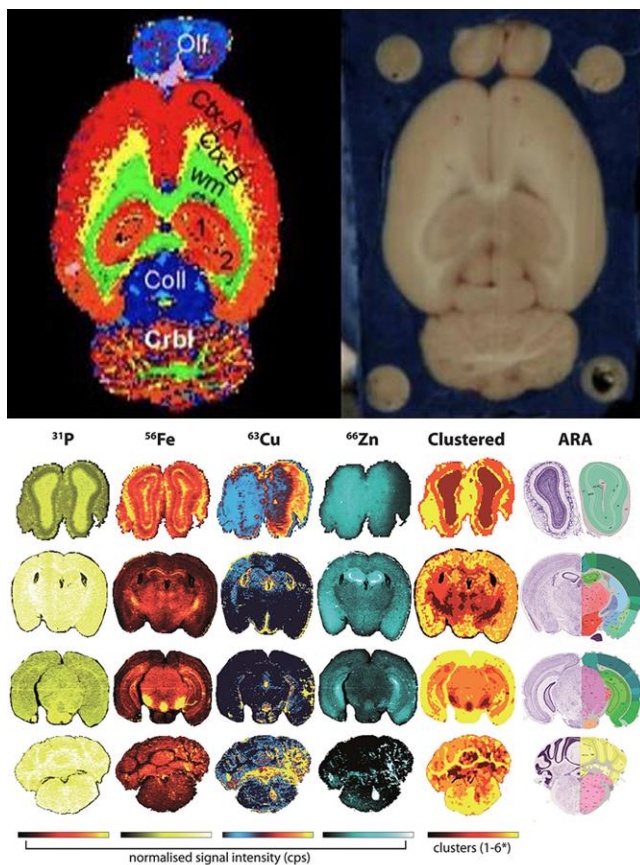

99

Figure 30: Top: Identification of 12 anatomical regions in a transverse rat brain section by k-means clustering of elemental distribution. Olfactory bulb (Olf); cortex, layers I–IV (Ctx-A); cortex, layers V–VI (Ctx-B); white matter (WM); plate of four collins (Coll); cerebellar grey matter (Crbl); hippocampus fascia dentata (1) and the cornu ammonis part 1–3 (2). Reproduced with permission from Ref. [421]. Copyright 2011 Elsevier. Bottom: Comparison of c-means fuzzy clustering algorithm with Allen Reference Atlas (ARA) for neuroanatomical classification in 4 coronal sections of wild type murine brain. Adapted from Ref. [378]. Licensed under CC BY 3.0.

Bishop *et al.*[422] investigated a variety of segmentation algorithms to objectively select dystrophin expression in the sarcolemma in wild type mice quadriceps, mdx mice, healthy human tissues, and Duchenne muscular dystrophy (DMD) patients. Dystrophin is a cytoplasmic protein that connects the cytoskeleton of a muscle fiber to the extracellular matrix via the cell membrane and has a characteristic honeycomb distribution. DMD patients typically express a small percentage of dystrophin when compared to healthy subjects, whilst mdx mice is a dystrophin knockout model and is therefore suitable for studying DMD. This application presents an interesting challenge to distinguish areas of positive dystrophin and is a pertinent example for the need to automatically segment for subsequent quantification and inter-sample comparisons. Immunohistochemistry and a gadolinium proxy were employed to measure relative concentrations of dystrophin as an alternative method of quantification to the standard concomitant Western blotting and immunofluorescence / immunohistochemistry. The authors trialed a combination of local, global, and k-clustering algorithms to automatically identify areas of positive dystrophin signals in each tissue section. Local approaches consisted of Sauvola[423] and Phansalkar[424] methods. The former was designed for adaptive document image binarization, and the latter is a variant of Sauvola's method that identifies positive signals by selection of a threshold below the local mean. The global segmentation algorithms consisted of Otsu's method[425] and median thresholding. Otsu's method calculates a threshold by minimizing intra-class intensity variance to segment the image into background and foreground, whilst the median threshold is calculated from across the entire dataset and data points below the median are demarcated as background and above as the foreground. The authors concluded that the superior method was k-means clustering which best represented the typical sarcolemma structure as determined from

visual comparison of IHC-LA-ICP-MS imaging and immunofluorescence images of natively expressed laminin in the sarcolemma.

The landmark paper by Giesen *et al.*[386] used a watershed algorithm (see section 5.8) to segment images of lanthanide-tagged antibodies produced using a CyTOF. Watershed processing treats grayscale images as topographic maps with pixel brightness representing height.[387] Lanthanide mass signals corresponding to cell membrane markers β-catenin, HER2, and cytokeratin 8/18 in human tissue were used to define and segment boundaries from which single cell breast cancer markers were extracted.

6.2.   Three-Dimensional Imaging

The first three-dimensional LA-ICP-MS image was constructed in 2010,[141] where Fe, Cu and Mn in twelve consecutive coronal sections of a mouse brain were imaged in a 6-OHDA lesioned mouse brain covering the depth of the substantia nigra (**Figure 31**). Each section was manually registered, and a 3D quantified image was assembled at approximately 100 μm^2 per pixel. The entire image stack took approximately 36 hours of continuous acquisition. The needle track from the unilateral injection was clearly visible in the Fe image with a very large increase in concentration of greater than 200 mg kg^{-1}, most likely from extracellular heme after hemorrhage from the traumatic brain injury. The intact P image showed the wound had healed in the animal euthanized 28 days after injection. The SN was shown to have a higher concentration of Fe ipsilateral to the lesion (40.7 mg kg^{-1}) compared against the contralateral SN (33.9 mg kg^{-1}), postulated to be due to a biological response of the neurotoxin. The Fe track was observed to terminate a few hundred μm superior to the SNc. The same manual method was further applied to the construction of a 46-plate reference atlas of Fe, Cu and Zn in the cerebrum and brainstem of a C57BL/6 mouse brain.[417] The ablation of the 46 sections was performed with an 80 μm laser spot size and took approximately 158 hours to complete scanning.
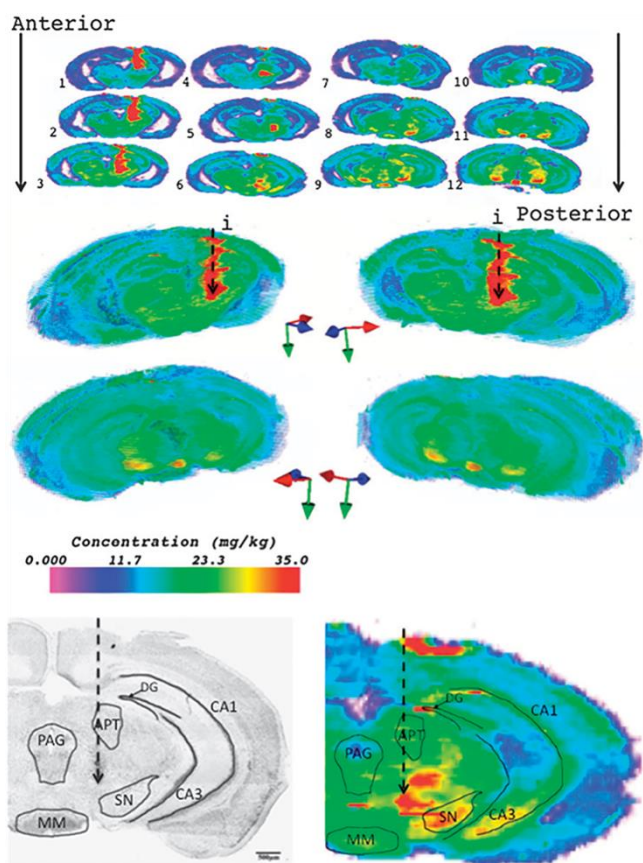
Figure 31: Two-dimensional images and 3D reconstruction of Fe in 6-OHDA lesioned (dashed arrow) mouse brain. Regions of mouse brain corresponding to increased trace element concentration are shown in a Nissl stain (bottom left) and Fe 2D image (bottom right) of section 6. APT = anterior pretectal nucleus, SN = substantia nigra, DG = dentate gyrus, CA1 and CA3 fields of hippocampus and MM = medial mammillary nucleus. Reproduced with permission from Ref [141]. Copyright 2010 Royal Society of Chemistry.

Paul *et al.*[378] described data reduction software, Biolite, to three-dimensionally map elements in the murine brain. The software was derived from the popular Iolite package that is used primarily in the geological sciences.[426] Serial coronal sections at 90 μm intervals were imaged for P, Mn, Fe, Co, Cu and Zn, as well as Au-labelled anti-TH. Each section was ablated, background corrected, masked with polygon drawing tool, and aligned using an automatic pyramidal voxel approach. The alignment algorithm performed an iterative affine transformation that minimized the difference between a 'reference' image and a 'test' image until each section was accurately registered for visualization and interrogation in three-dimensions. The software allows heuristic registration from single or multiple elements, providing flexibility in selection of contrasting data, and was superior to manual registrations

and due to the flexibility of element selection may be applied to any three-dimensional data stack.

Westerhausen *et al.*[427] undertook continuous acquisition to construct three-dimensional images of dystrophin expression in murine quadriceps. Here, repeated subpixel offset orthogonal ablation of a 50 μm thick section incubated with a Gd-labelled anti-dystrophin monoclonal antibody was performed until complete removal of the section from the glass slide. The resulting layers of data were processed via a combination of super resolution reconstruction and median filtering to produce three dimensional representations of dystrophin expression in individual muscle fibers (**Figure 32**). The authors investigated two laser conditions, the first consisting of refocusing the laser by 5 μm after acquisition of each layer, and the second was leaving the focal point constant. No difference was observed between the two methods. Although an unfocussed laser provides simplicity for experimental setups, it would be expected that with thicker sections, the refocusing approach would be required. The authors concluded that this method of three-dimensional acquisition was superior to previous methods because the requirement for registration of individual tissue section is dispensed with, providing a true spatial representation of the original specimen. It would be expected modifications of this method, especially with fast acquisition low-dispersion cells and TOF instruments, will be applied to three-dimensional reconstructions of whole organs such as brain, pancreas, lungs, liver etc, and will open a new vista of discovery in murine and other animal models of human diseases.
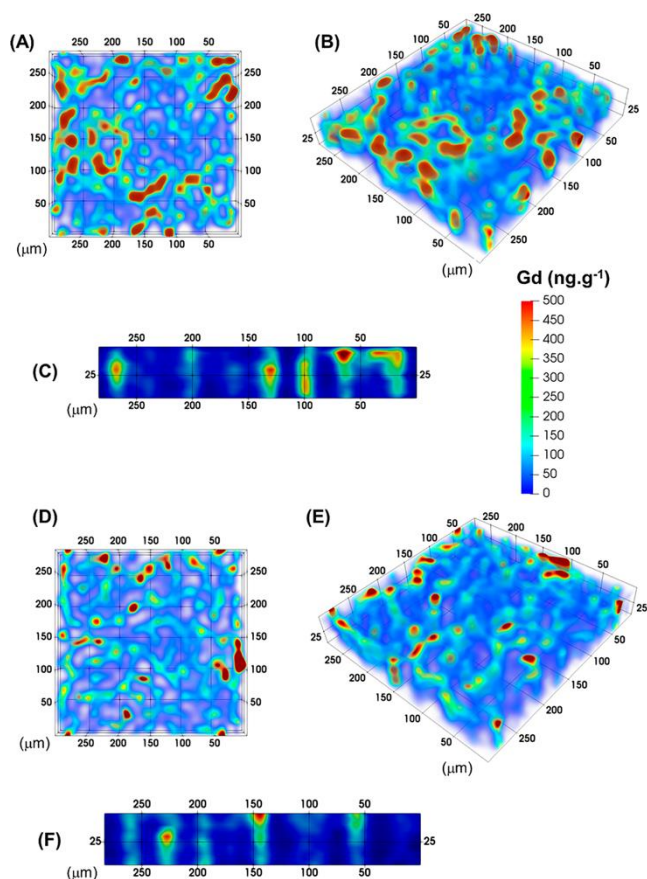
Figure 32: 3D reconstruction from repeated ablation. (A-C) Single-focus planar, and refocused oblique and isometric views of Gd-labelled dystrophin in mouse muscle tissue. (D-F) Planar, oblique and isometric views of single focus laser acquisition. Reproduced with permission from Ref. [427]. Copyright 2019 American Chemical Society.

7.   COMPLEMENTARY TECHNIQUES AND MULTIMODAL IMAGING

In vivo and *ex vivo* studies using various imaging methods are often conducted to clarify the mode of action and side effects of medications, to assess the toxicity of certain materials and/or to understand the development of diseases. LA-ICP-MS cannot be applied directly to *in vivo* imaging; however, it may be conducted with other complementary *in vivo* techniques such as computed tomography (CT), MRI or PET. Other *ex vivo* molecular or higher resolution elemental imaging methods such as XRF, secondary-ion mass spectrometry (SIMS) and laser-induced plasma spectroscopy (LIBS) offer synergistic potential for the analysis of elements, pharmaceuticals, metabolites, lipids, peptides and proteins in biological tissues. Multimodal imaging combines two or more methods to augment imaging diagnostics and to gain improved insights into biological processes.[428] For example, molecular selective methods such

as infrared spectroscopy and Raman spectroscopy may add additional valuable information [429,430]. Very high-resolution images of only a few nanometres using electron microscopy is another example of complementarity, providing valuable information in medical biochemical disorders[211] or for the analysis of nanomaterials in human cell lines.[223]

This section presents an overview of the most widely used techniques suitable for multimodal imaging in conjunction with LA-ICP-MS.

7.1.   In vivo imaging methods

In vivo imaging methods including CT and MRI provide orthogonal perspectives of elements and their behavior in whole organisms when employed in combination with LA-ICP-MS. CT and MRI can be performed without administration of contrast agents to visualize structural, functional and molecular changes in tissues.[431] Bulk *et al.*[432] used quantitative MRI to image Fe in the frontal cortex of healthy human controls with comparisons against histochemical and quantitative LA-ICP-MS imaging in post-mortem tissues of Alzheimer's disease patients. Construction of 3D native elemental maps for biological specimens using LA-ICP-MS coupled with X-ray tomography has been recently performed,[433, 434] opening the path to new 3D imaging capabilities to fully visualize the quantitative elemental distribution in structurally complex biological specimens (**Figure 33**). The combination of LA-ICP-MS with CT or MRI provides several advantages in clinical and research, connecting *in vivo* experiments and highly resolved quantitative data.
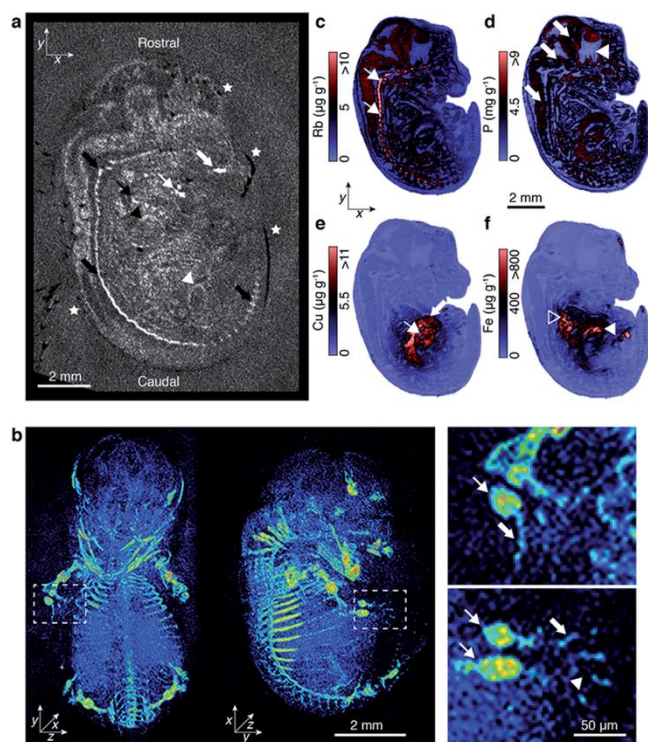
Figure 33: Multi-modal non-contrast μCT and LA-ICP-MS imaging of C57BL/6 mouse embryo. A) Tomographic sagittal radiograph. B) Reconstructed 3D voxelgrams oriented in the coronal (left) and sagittal (right) planes expand typical gross skeletal development features, (C-F) Concentrations of Rb, P, Cu and Zn found in the different parts of the embryo, respectively. Reproduced with permission from Ref. [433]. Copyright 2020 Royal Society of Chemistry.

Nanoparticles and metal-complexed contrasting agents are promising innovative materials to improve diagnostic imaging[253] and are suitable for multimodal imaging with LA-ICP-MS to monitor their distribution and fate. Pugh *et al.*[356] studied the distribution of Gd-based MRI contrasting agents and novel Gd-tagged liposome nanoparticles in pig brains, and investigated synergies of both techniques. Here, LA-ICP-MS improved the sensitivity of detecting the contrast agents, which became relevant a few years later after the observation that Gd may be retained in patients after contrast-enhanced MRI examinations.[273, 274, 356] Kevadiya *et al.*[435] assessed the biodistribution of lymphoid tissue macrophages of drug loaded multimodal radiolabeled particles (^{177}LuBSNRs) to predict pharmacological properties of long acting rilpivirine (LA RPV) employing a combination of single photon emission computed tomography (SPECT) and LA-ICP-MS. Recently, Mangarova *et al.*[436] used a combination of *in vivo* MRI and *ex vivo* magnetic particle spectroscopy (MPS) for the investigation of abdominal aortic aneurysms and its progression using iron magnetic NPs as surrogate markers for

molecular targeting of vascular inflammation. The results were validated by histological analysis, immunohistology and LA-ICP-MS.

7.2. Matrix Assisted Laser Desorption Ionization

Metal homeostasis is tightly controlled by countless biomolecules including peptides and lipids, which generally cannot be imaged by LA-ICP-MS. Consequently, analysis of heteroatoms and metals without knowledge of associated attenuating biomolecules or species information provides only a restricted perspective on biological processes. Therefore, molecular mass spectrometry imaging (MSI) techniques are becoming increasingly important for complete investigations. One dominant technique is MALDI, which was first described by Spengler in 1994[437] and extensively developed by Caprioli's research group after their first report in 1997.[438] MALDI-MSI links molecular evaluation of numerous analytes using mass spectrometry with spatial and morphological information to provide visualize arrangement of biomolecules in tissues and cells.[439, 440] MALDI-MSI has been used to produce spatially resolved images of proteins,[441, 442] lipids,[443, 444] and exogenous or endogenous small molecules, especially molecules involved in drug metabolism.[445 446-448] To support the desorption and ionization of these compounds, the previously deposited matrix plays a fundamental role and depending on the analytes of interest, different matrices are applicable.[449]

As histological features remain intact throughout the analysis of a tissue section, distribution maps of multiple analytes can be correlated with histological and clinical features. However, compared to LA-ICP-MS, the complexity of the biological matrix and interferences make quantification approaches extremely difficult. Sample preparation for MALDI-MSI is generally compatible to LA-ICP-MS. For example, Bianga *et al.*[189] compared LA-ICP-MS and MALDI-MSI targeting the distribution of two Pt-based anti-cancer metallodrugs (cisplatin and oxaliplatin) in human tumor samples taken from patients diagnosed with colorectal or ovarian peritoneal carcinomatosis. Matusch *et al.* analyzed 6-OHDA lesioned rat brain sections using molecular and atomic spectrometry.[332] Here, quantitative spatial distributions of Mn, Fe, Zn and Cu were obtained using LA-ICP-MS and correlated with the lipid distributions measured by ion

mobility-based MALDI-MS (**Figure 34**). A combination of LA-ICP-MS and MALDI was used to determine expression of the Zn-dependent matrix MMP-11 in breast cancer tissues with the former to quantitatively determine the Zn distribution and the latter to examine correlation between overexpression of MMP-11 protein by mass fingerprinting.[450] Holzlechner et al.[451] investigated human malignant pleural mesothelioma from a patient treated with cisplatin as a cytostatic agent with both LA-ICP-MS imaging and MALDI-MSI. While LA-ICP-MS provided quantitative information on the platinum distribution along with the distribution of other elemental analytes in the tissue sample, MALDI-MSI revealed the lipid distributions. Recently, Lohöfer et al.[452] used a combination of MRI, MALDI-MSI, and LA-ICP-MS to visualize the distribution of Gadofluorine P in plaque tissue with high spatial resolution, adding novel insights into molecular MR imaging of atherosclerosis.
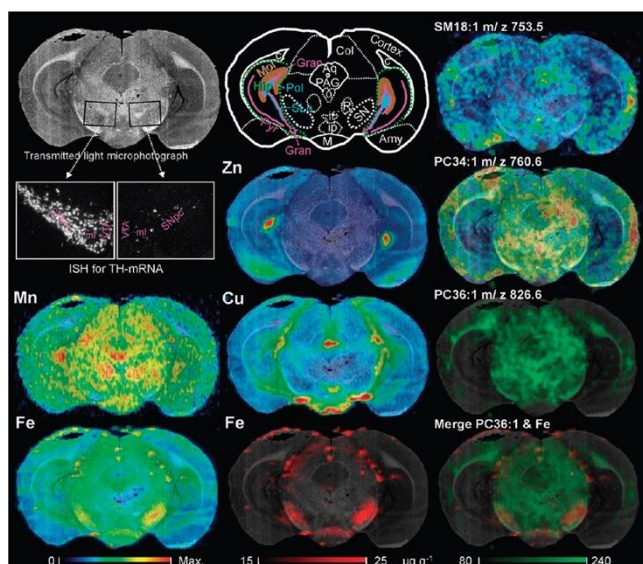
Figure 34: Multimodal imaging approach integrating light microscopy underlain as background of each image facilitating morphological orientation, elemental concentration maps obtained by LA-ICP-MS (left and middle column) and lipid maps obtained by MALDI-IM-MS imaging. Reproduced with permission from Ref. [332]. Copyright 2012 American Chemical Society.

7.3.   Secondary Ion Mass Spectrometry

MALDI-MSI and LA-ICP-MS are limited to analyses above the nanoscale which precludes the investigation of various anatomical structures including cells. Secondary Ion Mass

Spectrometry (SIMS) was developed in the late 1960s[453-455] and was commercialized by Benninghoven and colleagues in the late 1980s,[456, 457] and is suitable for imaging small molecules and elements with improved spatial resolutions. Here, a primary ion beam is focused on a surface and used to generate secondary molecular/elemental ions which can be extracted and measured by mass spectrometry. There are two fundamentally different approaches to SIMS analysis of biological samples based on the instrument design, static TOF-SIMS, and dynamic SIMS using a magnetic sector mass spectrometer. Static SIMS focusses on the first top monolayer of a specimen, providing mostly molecular characterization, whilst dynamic SIMS is used for bulk composition and in-depth distribution of trace elements. The primary ion beam can be focused to nanometer-scaled dimensions suitable for cell and tissue imaging with MS.[458] However, SIMS is partially limited in its application to life sciences due to challenges of quantitative analysis, molecular identification, and the necessity of biological sample preservation within high-vacuum environments. These limitations may be mitigated by developments of novel ion sources for TOF-SIMS and high-resolution dynamic SIMS instruments [458].

Although LA-ICP-MS and SIMS have been widely applied in geology and environmental applications,[459] only a few studies have been reported in biological specimens. Becker et al.[78] combined LA-ICP-MS and SIMS to measure cholesterol, lipids and alkali metals in mouse heart tissue. Here, various transition, alkali and alkaline-earth metals and non-metals were imaged by LA-ICP-MS, while Na, K and phosphocholine, choline, and cholesterol were imaged by SIMS. Recent studies have explored the applicability to *in vivo* applications, combining LA-ICP-MS, nanoSIMS and electron microscopy imaging suitable for multi-scale detection of Pt and Cu distribution in tissues. Legin *et al.*[460] determined the spatial platinum accumulation in kidney and tumor samples upon administration of selected Pt anticancer drugs, which were quantitatively assessed by LA-ICP-MS in histologically heterogeneous organs and selected regions of interest for subcellular-scale imaging with nanoSIMS. Moreover, Ackerman *et al.*[461] employed a combination of LA-ICP-MS and nanoSIMS to investigate the distribution and concentration of Cu within photoreceptor megamitochondria in a zebrafish model of Menkes disease to obtain images with higher spatial resolution.

7.4.   Laser-Induced Breakdown Spectroscopy

Laser-induced breakdown spectroscopy[462] (LIBS) harnesses post ablation short-lived plasmas above the sample to excite elements for optical emission detection. Some advantages of LIBS include rapid multielement analyses, simplicity, ease of operation at room temperature and pressure, and minimal or no sample preparation. These features make LIBS-based imaging a promising and rapid method for investigations of elemental distributions and mapping in a variety of samples.[463] However, limitations related to lower sensitivity, matrix effects and spectral interferences generally make quantification difficult. Nevertheless, LIBS is particularly suitable for integration into LA-ICP-MS workflows for simultaneous atomic emission and isotopic mass measurement in the same experiment. LIBS is often not suitable for analysis of trace concentrations in biological tissues and has been mostly be used for geological applications.[464] Bonta *et al*. demonstrated the simultaneous use of LIBS and LA-ICP-MS (tandem LA/LIBS) for elemental mapping of trace and bulk elements in biological tissues.[465] While LA-ICP-MS was well suited for analysis of trace elements such as Fe, Zn, Cu in tissues, LIBS was optimal for the mapping of major (C, H, O) and minor elements (Na, K, Ca, Mg). The combination of both techniques provided synergistic measurement of elements which was not possible in isolation due to low sensitivity and/or strong interferences. Galiová *et al*. combined LA-ICP-MS and LIBS to analyze metals in prehistoric brown bears (*Ursus arctos*) to reconstruct the nutrition, health and migration of the animal,[301] and Kaiser *et al*. analyzed Pb, Mn and Cu in plant tissues.[229]

7.5.   X-Ray Fluorescence Imaging

XRF is a non-destructive multi-elemental mapping technique compatible with subsequent LA-ICP-MS imaging of biological tissue. Depending on the experimental set-up, various primary X-ray energies may be used to analyse almost all elements of the periodic table. Bench-top instruments typically have resolutions in mid-μm ranges and detection limits in the low μg g^{-1} region, depending on the element and excitation energy. However, with high-end instrumentation such as particle accelerators, limits of detection and spatial resolution are much improved providing attractive options for imaging of biological tissues.[466, 467]

LA-ICP-MS and benchtop µXRF were compared by Gholap et al.[221] who performed elemental analysis of the freshwater crustacean *Daphnia magna*. In this study, Ca, P, S and Zn were selected for element-to-tissue correlation. The results showed similar detection limits of Ca and P by comparing both techniques, using a lateral resolution of 15 µm for LA-ICP-MS and 25 µm for µXRF. Blaske et al.[468] investigated complex histological specimens including tissues affected by metal implants, bone, and soft tissue embedded in methyl methacrylate substrate by capillary-focused µXRF and LA-ICP-MS. Neves et al.[267] used LA-ICP-MS and µXRF as complementary techniques to investigate the uptake and translocation of La_2O_3 NPs in stems and leaves of the South American medicinal plant *Pfaffia glomerata.* Feng et al.[159] developed a method based on isotope dilution LA-ICP-MS for accurate quantitative determination of Fe, Cu and Zn in brain tissue sections using µXRF and immunohistochemical approaches in AD murine brains. In a recent study performed by Mueller et al.[70] a novel quantification approach for µXRF analysis using matrix-matched gelatin standards was used to quantify the iron distribution in liver tissue of a murine iron-overload model. In addition, LA-ICP-MS/MS was used to verify the µXRF results and to improve LODs. In another study, Reifschneider et al.[257] traced the AgNP uptake by macrophages using synchrotron-based µXRF and LA-ICP-MS. The non-destructive nature of X-ray methods allowed subsequent LA-ICP-MS experiments to provide the sensitivity required to determine elemental distribution within the same sample.

8.   CONCLUSIONS AND FUTURE DIRECTIONS

LA-ICP-MS imaging is now a mature technique that may be applied to a vast array of contemporary applications in health, environment, occupational exposures, and the elucidation of fundamental mechanistic biological processes. Commercial systems solely marketed for imaging applications offer turnkey solutions accessible to the general research community and may be exploited by any user with basic analytical or bio-analytical chemistry training.

The introduction of modern time of flight instruments has invited speculation of the obsolescence of quadrupole systems for imaging applications. This sentiment is based on fast scanning of TOF mass spectrometers which allow very rapid acquisitions and high resolution

when coupled to modern cells. However, this projection is somewhat premature when several factors are considered. The first is the relative expense of TOF instruments which are typically 3 times more costly than quadrupole counterparts. Although fast acquisition provides significant savings in running costs per sample, this high cost of capital expenditure presents a barrier of entry for new users. The high saturation of single quadrupole instruments in the ICP-MS market presents opportunities for researchers to purchase lasers to upgrade existing instrumentation within laboratories. Although quadrupoles cannot compete with TOF instruments in terms of multiplexing and single cell resolution, not all applications require high resolution. For example, imaging gross anatomical structures may be suitable to answer specific mechanistic questions, as has been demonstrated in many applications described in this review. Furthermore, new technologies that time the firing of the laser with that of the quadrupole scanning cycle to limit aliasing artefacts are in development.[469] These novel devices are effective for measurement of multiple elements with quadrupole-based instruments with fast washout cells and single shot analysis, offering the potential for highly multiplexed analyses as an alternative to TOF instruments.

There is excellent potential for imaging biomolecules in both research and routine clinical applications. Imaging of molecular cancer biomarkers is an area of growth driving the continued development of incorporation of IHC into imaging workflows. This niche area is likely to be dominated by TOF based configurations due to high resolution and multiplexing requirements. It is anticipated that improved tagging protocols such as substitution of lanthanide loaded polymers with nanoparticles for higher sensitivities will be developed. There is also a necessity for better quality control and standard operating procedures for IHC, especially in assurance of antibody tagging efficiencies, and quantification approaches. The multiplexing capability of IHC-LA-ICP-MS is unsurpassed by any other method and offers unique opportunities for precision diagnostics in clinical settings. The uptake of the technology in clinical practice to help define treatment regimens will be dependent on the relative cost to benefit aspects when compared to standard IHC/IF procedures. The clinical translation of the technology in the short term is likely to augment contemporary approaches and may be adopted more rapidly if capital costs were reduced.

Cell designs for imaging have reached a pinnacle with signal washout times in milliseconds. It is unlikely and unnecessary to further improve washout times, however there is room for improvement in configurations that reduce capital costs in both manufacture of cells and laser choice. In general, LA systems for biological imaging have been repurposed from geoscience applications and consequently incorporate lasers with higher fluences than necessary. Development of a low cost and low powered laser sufficient to ablate biological material would significantly increase the momentum of uptake of LA-ICP-MS imaging across all research and medical areas.

A search of the literature reveals that the application of nanoparticles for the treatments and/or diagnosis of cancers remains of high interest, with approximately 5 to 6 thousand publications per year since 2016. Application of LA-ICP-MS to investigate the spatial distribution of nanoparticles post administration has been used in just a handful applications. This surprising underutilization is perhaps due to a lack of awareness and knowledge of the technique, or its relative expense. It is anticipated that nanoparticle imaging combined with traditional solution-based characterization will be a huge area of growth in the coming years.

9. AUTHOR INFORMATION

9.1. Corresponding Author

*Email: philip.doble@uts.edu.au

9.2. ORCID

Philip A. Doble: 0000-0002-8472-1301

Raquel Gonzalez de Vega: 0000-0002-9806-9633

David P. Bishop: 0000-0002-6533-4410

Dominic J. Hare: 0000-0002-5922-7643

David Clases: 0000-0003-3880-9385

9.3. Notes

The authors declare no competing financial interest.

9.4. Biographies

Philip A. Doble

Distinguished Professor Doble is the founder and leader of the Atomic Medicine Initiative and has a world-wide reputation for Analytical and Bioanalytical research such as discovery of new biomarkers for diseases where disequilibrium of elements in the body are thought to be involved. Essential trace elements have long been known to play key roles in innumerable physiological processes. Many enzymes and proteins use embedded trace elements for activity. For example, the superoxide dismutase (SOD) family of enzymes responsible for the antioxidant defense of all cells exposed to oxygen requires copper, zinc and manganese to function. Furthermore, metabolic disturbances associated with disease are accompanied by detectable changes in trace element concentrations. He has developed platform technology for elemental bio-imaging that is used by biologists and medical specialists to probe these metabolic disturbances.

Raquel Gonzalez de Vega

Raquel Gonzalez de Vega obtained her doctoral degree in Analytical Chemistry at the University of Oviedo (Spain) in 2017 in the group of Prof. Sanz-Medel. During her PhD studies she performed two research stays at the University of Muenster in the Group or Prof. Karst. In 2017 she joined Prof. Doble's Group as a postdoctoral researcher and became lecturer for Analytical Chemistry at the University of Technology Sydney (UTS) in 2020. She is a member of the Atomic Medicine Initiative and focusses her research on the development of new methods based on elemental and molecular mass spectrometry as well as trace elemental analyses, bio-imaging techniques and speciation analysis.

David P. Bishop

Dr Bishop is a Senior Lecturer in analytical chemistry at the University of Technology Sydney, where his research focuses on the application of state-of-the-art technology to analytical challenges in a diverse range of disciplines with a particular emphasis on biological and environmental sciences. He is a current recipient of the Australian Research Council's Discovery Early Career Researcher Award, with his Fellowship is examining the translational utility of immunohistochemistry and chemical imaging in cell biology. He is a former Fullbright Scholar, spending part of 2016 at the University of California, Los Angeles (UCLA) Center for Duchenne Muscular Dystrophy (CDMD) developing new methods for visualising disease biochemistry.

Dominic Hare

Associate Professor Dominic Hare received a PhD in Chemistry from UTS in 2009, after which he held fellowships from the Australian Research Council and National Health and Medical Research Council at UTS and the Florey Institute of Neuroscience and Mental Health. He relocated to Melbourne in 2012 and worked at the Florey, where he established the Atomic Pathology Laboratory. He left the Florey in late 2018 to join the University of Melbourne. His primary interest is the emerging field of digital pathology and applications of multimodal chemical imaging.

David Clases

David Clases obtained a PhD in Analytical Chemistry 2017 at the University of Muenster (Germany) and undertook his postdoctoral studies at the University of Technology Sydney (Australia). After the award of a fellowship from the German Research Foundation in 2018, he was employed as a lecturer for Analytical Chemistry. He works on the development of ICP-MS methods and hyphenated techniques to perform elemental speciation and bioimaging. He further develops new approaches for the characterization of emerging nanomaterials and their incorporation into analytical workflows.

10. ACKNOWLEDGEMENTS

11. REFERENCES

1. Banci, L.; Bertini, I., Metallomics and the Cell: Some Definitions and General Comments. *Met. Ions Life Sci.* **2013**, *12,* 1-13.
2. Wang, S.; Brown, R.; Gray, D. J., Application of Laser Ablation-ICPMS to the Spatially Resolved Micro-Analysis of Biological Tissue. *Appl. Spectrosc.* **1994**, *48,* 1321-1325.
3. Feldmann, J. r.; Kindness, A.; Ek, P., Laser Ablation of Soft Tissue Using a Cryogenically Cooled Ablation Cell. *J. Anal. At. Spectrom.* **2002**, *17,* 813-818.
4. Kindness, A.; Sekaran, C. N.; Feldmann, J., Two-Dimensional Mapping of Copper and Zinc in Liver Sections by Laser Ablation-Inductively Coupled Plasma Mass Spectrometry. *Clin. Chem.* **2003**, *49,* 1916-1923.
5. Greenfield, S.; Jones, I. L.; Berry, C. T., High-Pressure Plasmas as Spectroscopic Emission Sources. *The Analyst* **1964**, *89,* 713-720.
6. Wendt, R. H.; Fassel, V. A., Induction-Coupled Plasma Spectrometric Excitation Source. *Anal. Chem.* **2002**, *37,* 920-922.
7. Boumans, P. W. J. M., Inductively Coupled Plasma-Atomic Emission Spectroscopy: Its Present and Future Position in Analytical Chemistry. *Fresenius' Zeitschrift für Analytische Chemie* **1979**, *299,* 337-361.
8. Fassel, V. A., Analytical Inductively Coupled Plasma Spectroscopies — Past, Present, and Future. *Fresenius' Zeitschrift für analytische Chemie* **1986**, *324,* 511-518.
9. Meyer, G. A., Icp: Still the Panacea for Trace Metals Analysis? *Anal. Chem.* **2008**, *59,* 1345A-1354A.
10. Gray, A. L., It All Depends on the Source. *PNAS* **1974**, *11,* 182-183.
11. Gray, A. L., Mass-Spectrometric Analysis of Solutions Using an Atmospheric Pressure Ion Source. *The Analyst* **1975**, *100,* 289-299.
12. Houk, R. S.; Fassel, V. A.; Flesch, G. D.; Svec, H. J.; Gray, A. L.; Taylor, C. E., Inductively Coupled Argon Plasma as an Ion Source for Mass Spectrometric Determination of Trace Elements. *Anal. Chem.* **2002**, *52,* 2283-2289.

13. Potter, D., A Commercial Perspective on the Growth and Development of the Quadrupole ICP-MS Market. *J. Anal. At. Spectrom.* **2008**, *23,* 690-693.

14. Gray, A. L., The Evolution of the ICP as an Ion Source for Mass Spectrometry. *J. Anal. At. Spectrom.* **1986**, *1,* 403-405.

15. Profrock, D.; Prange, A., Inductively Coupled Plasma-Mass Spectrometry (ICP-MS) for Quantitative Analysis in Environmental and Life Sciences: A Review of Challenges, Solutions, and Trends. *Appl. Spectrosc.* **2012**, *66,* 843-68.

16. Bishop, D. P.; Hare, D. J.; Clases, D.; Doble, P. A., Applications of Liquid Chromatography-Inductively Coupled Plasma-Mass Spectrometry in the Biosciences: A Tutorial Review and Recent Developments. *Trends Analyt. Chem.* **2018**, *104,* 11-21.

17. Haraguchi, H., Metallomics as Integrated Biometal Science. *J. Anal. At. Spectrom.* **2004**, *19,* 5-14.

18. Houk, R. S., Mass Spectrometry of Inductively Coupled Plasmas. *Anal. Chem.* **2008**, *58,* 97A-105A.

19. Uchida, H.; Ito, T., Comparative Study of 27.12 and 40.68 Mhz Inductively Coupled Argon Plasmas for Mass Spectrometry on the Basis of Analytical Characteristic Distributions. *J. Anal. At. Spectrom.* **1994**, *9,* 1001-1006.

20. Saha, M. N., Liii. Ionization in the Solar Chromosphere. *Lond. Edinb. Dubl. Phil. Mag.* **2009**, *40,* 472-488.

21. Niu, H.; Houk, R. S., Fundamental Aspects of Ion Extraction in Inductively Coupled Plasma Mass Spectrometry. *Spectrochim. Acta Part B At. Spectrosc.* **1996**, *51,* 779-815.

22. Pak, Y.-N., Errors in Isotope Dilution Caused by Matrix-Induced Mass Bias Effect in Quadrupole Inductively Coupled Plasma-Mass Spectrometry. *Bull. Korean Chem. Soc.* **2014**, *35,* 3482-3488.

23. Tanner, S. D., Space Charge in ICP-MS: Calculation and Implications. *Spectrochim. Acta Part B At. Spectrosc.* **1992**, *47,* 809-823.

24. Hu, K.; Clemons, P. S.; Houk, R. S., Inductively Coupled Plasma Mass Spectrometry with an Enlarged Sampling Orifice and Offset Ion Lens. I. Ion Trajectories and Detector Performance. *J. Am. Soc. Mass Spectrom.* **1993**, *4,* 16-27.

25. Vanhaecke, F.; de Wannemacker, G. n.; Moens, L.; Dams, R.; Latkoczy, C.; Prohaska, T.; Stingeder, G., Dependence of Detector Dead Time on Analyte Mass Number in Inductively Coupled Plasma Mass Spectrometry. *J. Anal. At. Spectrom.* **1998**, *13,* 567-571.

26. Tanner, S. D.; Baranov, V. I.; Bandura, D. R., Reaction Cells and Collision Cells for ICP-MS: A Tutorial Review. *Spectrochim. Acta Part B At. Spectrosc.* **2002**, *57,* 1361-1452.

27. Fernández, S. D.; Sugishama, N.; Encinar, J. R.; Sanz-Medel, A., Triple Quad ICPMS (ICPQQQ) as a New Tool for Absolute Quantitative Proteomics and Phosphoproteomics. *Anal. Chem.* **2012**, *84,* 5851-5857.

28. Bolea-Fernandez, E.; Balcaen, L.; Resano, M.; Vanhaecke, F., Overcoming Spectral Overlap Via Inductively Coupled Plasma-Tandem Mass Spectrometry (ICP-MS/MS). A Tutorial Review. *J. Anal. At. Spectrom.* **2017**, *32,* 1660-1679.

29. Gießmann, U.; Greb, U., High Resolution ICP-MS ? A New Concept for Elemental Mass Spectrometry. *Fresenius J. Anal. Chem.* **1994**, *350,* 186-193.

30. Moldovan, M.; Krupp, E. M.; Holliday, A. E.; Donard, O. F. X., High Resolution Sector Field ICP-MS and Multicollector ICP-MS as Tools for Trace Metal Speciation in Environmental Studies: A Review. *J. Anal. At. Spectrom.* **2004**, *19,* 815-822.

31. Myers, D. P.; Hieftje, G. M., Preliminary Design Considerations and Characteristics of an Inductively Coupled Plasma-Time-of-Flight Mass Spectrometer. *Microchem. J.* **1993**, *48,* 259-277.

32. Bandura, D. R.; Baranov, V. I.; Ornatsky, O. I.; Antonov, A.; Kinach, R.; Lou, X.; Pavlov, S.; Vorobiev, S.; Dick, J. E.; Tanner, S. D., Mass Cytometry: Technique for Real Time Single Cell Multitarget Immunoassay Based on Inductively Coupled Plasma Time-of-Flight Mass Spectrometry. *Anal. Chem.* **2009**, *81,* 6813-6822.

33. Bleiner, D.; Belloni, F.; Doria, D.; Lorusso, A.; Nassisi, V., Overcoming Pulse Mixing and Signal Tailing in Laser Ablation Inductively Coupled Plasma Mass Spectrometry Depth Profiling. *J. Anal. At. Spectrom.* **2005**, *20,* 1337-1343.

34. Gundlach-Graham, A.; Gunther, D., Toward Faster and Higher Resolution LA-ICPMS Imaging: On the Co-Evolution of LA Cell Design and Icpms Instrumentation. *Anal. Bioanal. Chem.* **2016**, *408,* 2687-2695.

35. Linge, K. L.; Jarvis, K. E., Quadrupole ICP-MS: Introduction to Instrumentation, Measurement Techniques and Analytical Capabilities. *Geostand. Geoanal. Res.* **2009**, *33,* 445-467.

36. Clases, D.; Gonzalez de Vega, R.; Funke, S.; Lockwood, T. E.; Westerhausen, M. T.; Taudte, R. V.; Adlard, P. A.; Doble, P. A., Matching Sensitivity to Abundance: High Resolution Immuno-Mass Spectrometry Imaging of Lanthanide Labels and Endogenous Elements in the Murine Brain. *J. Anal. At. Spectrom.* **2020**, *35,* 728-735.

37. Sylvester, P. J.; Jackson, S. E., A Brief History of Laser Ablation Inductively Coupled Plasma Mass Spectrometry (LA–ICP–MS). *Elements* **2016**, *12,* 307-310.

38. Petrell, M.; Morgavi, D.; Vetere, F.; Perugini, D., Elemental Imaging and Petro-Volcanological Applications of an Improved Laser Ablation Inductively Coupled Quadrupole Plasma Mass Spectrometry. *Periodico di Mineralogia* **2016**, *85,* 25-39.

39. Horstmann, M.; Gonzalez de Vega, R.; Bishop, D. P.; Karst, U.; Doble, P. A.; Clases, D., Determination of Gadolinium Mri Contrast Agents in Fresh and Oceanic Waters of Australia Employing Micro-Solid Phase Extraction, Hilic-ICP-MS and Bandpass Mass Filtering. *J. Anal. At. Spectrom.* **2021**.

40. Meyer, S.; Gonzalez de Vega, R.; Xu, X.; Du, Z.; Doble, P. A.; Clases, D., Characterization of Upconversion Nanoparticles by Single-Particle ICP-MS Employing a Quadrupole Mass Filter with Increased Bandpass. *Anal. Chem.* **2020**, *92,* 15007-15016.

41. Lear, J.; Hare, D.; Adlard, P.; Finkelstein, D.; Doble, P., Improving Acquisition Times of Elemental Bio-Imaging for Quadrupole-Based LA-ICP-MS. *J. Anal. At. Spectrom.* **2012**, *27,* 159-164.

42. Hattendorf, B.; Hartfelder, U.; Günther, D., Skip the Beat: Minimizing Aliasing Error in LA-ICP-MS Measurements. *Anal. Bioanal. Chem.* **2019**, *411,* 591-602.

43. van Elteren, J. T. v.; Šelih, V. S.; Šala, M.; Malderen, S. J. M. V.; Vanhaecke, F., Imaging Artifacts in Continuous Scanning 2D LA-ICPMS Imaging Due to Nonsynchronization Issues. *Anal. Chem.* **2018**, *90,* 2896-2901.

44. van Elteren, J. T.; Šelih, V. S.; Šala, M., Insights into the Selection of 2D LA-ICP-MS (Multi) Elemental Mapping Conditions. *J. Anal. At. Spectrom.* **2019**, *34,* 1919-1931.

45. van Elteren, J. T.; Metarapi, D.; Šala, M.; Šelih, V. S.; Stremtan, C. C., Fine-Tuning of LA-ICP-QMS Conditions for Elemental Mapping. *J. Anal. At. Spectrom.* **2020**, *35,* 2494-2497.

46. van Malderen, S. J. M.; van Elteren, J. T.; Vanhaecke, F., Development of a Fast Laser Ablation-Inductively Coupled Plasma-Mass Spectrometry Cell for Sub-μm Scanning of Layered Materials. *J. Anal. At. Spectrom.* **2015**, *30,* 119-125.

47. Chew, D.; Drost, K.; Petrus, J. A., Ultrafast, > 50 hz LA-ICP-MS Spot Analysis Applied to U‑Pb Dating of Zircon and Other U‑Bearing Minerals. *Geostand. Geoanal. Res.* **2019**, *43,* 39-60.

48. Matthews, W. A.; Guest, B., A Practical Approach for Collecting Large-N Detrital Zircon U-Pb Data Sets by Quadrupole LA-ICP-MS. *Geostand. Geoanal. Res.* **2017**, *41,* 161-180.

49. Metarapi, D.; Šala, M.; Vogel-Mikuš, K.; Šelih, V. S.; Elteren, J. T. v., Nanoparticle Analysis in Biomaterials Using Laser Ablation–Single Particle–Inductively Coupled Plasma Mass Spectrometry. *Anal. Chem.* **2019**, *91,* 6200-6205.

50. Hare, D. J.; Fryer, F.; Paul, B.; Bishop, D. P.; Doble, P. A., Characterisation of Matrix-Based Polyatomic Interference Formation in Laser Ablation-Inductively Coupled Plasma-Mass Spectrometry using Dried Micro-Droplet Ablation and its Relevance for Bioimaging. *Anal. Methods* **2016**, *8,* 7552-7556.

51. Lear, J.; Hare, D. J.; Fryer, F.; Adlard, P. A.; Finkelstein, D. I.; Doble, P. A., High-Resolution Elemental Bioimaging of Ca, Mn, Fe, Co, Cu, and Zn Employing LA-ICP-MS and Hydrogen Reaction Gas. *Anal. Chem.* **2012**, *84,* 6707-6714.

52. Hu, Z.; Gao, S.; Liu, Y.; Hu, S.; Chen, H.; Yuan, H., Signal Enhancement in Laser Ablation ICP-MS by Addition of Nitrogen in the Central Channel Gas. *J. Anal. At. Spectrom.* **2008**, *23,* 1093-1101.

53. Lam, J. W. H.; Horlick, G., A Comparison of Argon and Mixed Gas Plasmas for Inductively Coupled Plasma-Mass Spectrometry. *Spectrochim. Acta Part B At. Spectrosc.* **1990**, *45,* 1313-1325.

54. Durrant, S. F., Feasibility of Improvement in Analytical Performance in Laser Ablation Inductively Coupled Plasma-Mass Spectrometry (LA-ICP-MS) by Addition of Nitrogen to the Argon Plasma. *Fresenius J. Anal. Chem.* **1994**, *349,* 768-771.

55. Richter-Brockmann, S.; Garbert, K.; von Bremen-Kühne, M.; Wehe, C. A.; Reifschneider, O.; Sperling, M.; Wallrad, L.; Schmitz-Thom, I.; Kudla, J.; Karst, U., Elemental Bioimaging of Na Distribution in Roots of Arabidopsis Thaliana Using Laser Ablation-ICP-MS under Cold Plasma Conditions. *J. Anal. At. Spectrom.* **2020**, *35,* 2057-2063.

56. Y. Patterson, K.; Veillon, C.; David Hill, A.; B. Moser-Veillon, P.; C. O'Haver, T., Measurement of Calcium Stable Isotope Tracers Using Cool Plasma ICP-MS. *J. Anal. At. Spectrom.* **1999**, *14,* 1673-1677.

57. Koyanagi, G. K.; Bohme, D. K.; Bandura, D. R., Inductively Coupled Plasma Mass Spectrometry Handbook. **2005**, 336-384.

58. Yamada, N., Kinetic Energy Discrimination in Collision/Reaction Cell ICP-MS: Theoretical Review of Principles and Limitations. *Spectrochim. Acta Part B At. Spectrosc.* **2015**, *110,* 31-44.

59. McCurdy, E.; Woods, G., The Application of Collision/Reaction Cell Inductively Coupled Plasma Mass Spectrometry to Multi-Element Analysis in Variable Sample Matrices, Using He as a Non-Reactive Cell Gas. *J. Anal. At. Spectrom.* **2004**, *19,* 607-615.

60. Hachmoller, O.; Zibert, A.; Zischka, H.; Sperling, M.; Groba, S. R.; Grunewald, I.; Wardelmann, E.; Schmidt, H. H.; Karst, U., Spatial Investigation of the Elemental

Distribution in Wilson's Disease Liver after D-Penicillamine Treatment by LA-ICP-MS. *J. Trace Elem. Med. Biol.* **2017**, *44,* 26-31.

61. Mason, P. R. D.; Kraan, W. J., Attenuation of Spectral Interferences During Laser Ablation Inductively Coupled Plasma Mass Spectrometry (LA-ICP-MS) Using an Rf Only Collision and Reaction Cell. *J. Anal. At. Spectrom.* **2002**, *17,* 858-867.

62. Bandura, D. R.; Baranov, V. I.; Litherland, A. E.; Tanner, S. D., Gas-Phase Ion–Molecule Reactions for Resolution of Atomic Isobars: Ams and ICP-MS Perspectives. *Int. J. Mass Spectrom.* **2006**, *255-256,* 312-327.

63. D'Ilio, S.; Violante, N.; Majorani, C.; Petrucci, F., Dynamic Reaction Cell ICP-MS for Determination of Total as, Cr, Se and V in Complex Matrices: Still a Challenge? A Review. *Anal. Chim. Acta* **2011**, *698,* 6-13.

64. Koppenaal, D. W.; Eiden, G. C.; Barinaga, C. J., Collision and Reaction Cells in Atomic Mass Spectrometry: Development, Status, and Applications. *J. Anal. At. Spectrom.* **2004**, *19,* 561-570.

65. Wehe, C. A.; Niehoff, A. C.; Thyssen, G. M.; Sperling, M.; Karst, U., Rapid Cell Mode Switching and Dual Laser Ablation Inductively Coupled Plasma Mass Spectrometry for Elemental Bioimaging. *Rapid Commun. Mass Spectrom.* **2014**, *28,* 2627-2635.

66. Bishop, D. P.; Clases, D.; Fryer, F.; Williams, E.; Wilkins, S.; Hare, D. J.; Cole, N.; Karst, U.; Doble, P. A., Elemental Bio-Imaging Using Laser Ablation-Triple Quadrupole-ICP-MS. *J. Anal. At. Spectrom.* **2016**, *31,* 197-202.

67. Balcaen, L.; Bolea-Fernandez, E.; Resano, M.; Vanhaecke, F., Inductively Coupled Plasma - Tandem Mass Spectrometry (ICP-MS/MS): A Powerful and Universal Tool for the Interference-Free Determination of (Ultra)Trace Elements - a Tutorial Review. *Anal. Chim. Acta* **2015**, *894,* 7-19.

68. Masthoff, M.; Buchholz, R.; Beuker, A.; Wachsmuth, L.; Kraupner, A.; Albers, F.; Freppon, F.; Helfen, A.; Gerwing, M.; Höltke, C.; Hansen, U.; Rehkämper, J.; Vielhaber, T.; Heindel, W.; Eisenblätter, M.; Karst, U.; Wildgruber, M.; Faber, C., Introducing Specificity to Iron Oxide Nanoparticle Imaging by Combining 57 Fe-Based MRI and Mass Spectrometry. *Nano Lett.* **2019**, *19,* 7908-7917.

69. Van Acker, T.; Bolea-Fernandez, E.; De Vlieghere, E.; Gao, J.; De Wever, O.; Vanhaecke, F., Laser Ablation-Tandem Icp-Mass Spectrometry (LA-ICP-MS/MS) Imaging of Iron Oxide Nanoparticles in Ca-Rich Gelatin Microspheres. *J. Anal. At. Spectrom.* **2019**, *34,* 1846-1855.

70. Müller, J.-C.; Horstmann, M.; Traeger, L.; Steinbicker, A. U.; Sperling, M.; Karst, U., μxrf and La-Icp-Tqms for Quantitative Bioimaging of Iron in Organ Samples of a Hemochromatosis Model. *J. Trace Elem. Med. Biol.* **2019**, *52,* 166-175.

71. Crone, B.; Schlatt, L.; Nadar, R. A.; van Dijk, N. W. M.; Margiotta, N.; Sperling, M.; Leeuwenburgh, S.; Karst, U., Quantitative Imaging of Platinum-Based Antitumor Complexes in Bone Tissue Samples Using LA-ICP-MS. *J. Trace Elem. Med. Biol.* **2019**, *54,* 98-102.

72. Bucker, P.; Richter, H.; Radbruch, A.; Sperling, M.; Brand, M.; Holling, M.; van Marck, V.; Paulus, W.; Jeibmann, A.; Karst, U., Deposition Patterns of Iatrogenic Lanthanum and Gadolinium in the Human Body Depend on Delivered Chemical Binding Forms. *J. Trace Elem. Med. Biol.* **2021**, *63,* 126665.

73. Thyssen, Georgina M.; Keil, C.; Wolff, M.; Sperling, M.; Kadow, D.; Haase, H.; Karst, U., Bioimaging of the Elemental Distribution in Cocoa Beans by Means of LA-ICP-TQMS. *J. Anal. At. Spectrom.* **2018**, *33,* 187-194.

74. Becker, J. S.; Zoriy, M.; Przybylski, M.; Becker, J. S., High Resolution Mass Spectrometric Brain Proteomics by Maldi-Fticr-Ms Combined with Determination of P, S, Cu, Zn and Fe by LA-ICP-MS. *Int. J. Mass Spectrom.* **2007**, *261,* 68-73.

75. Becker, J. S.; Lobinski, R.; Becker, J. S., Metal Imaging in Non-Denaturing 2d Electrophoresis Gels by Laser Ablation Inductively Coupled Plasma Mass Spectrometry (LA-ICP-MS) for the Detection of Metalloproteins. *Metallomics* **2009**, *1,* 312-316.

76. Konz, I.; Fernandez, B.; Fernandez, M. L.; Pereiro, R.; Gonzalez, H.; Alvarez, L.; Coca-Prados, M.; Sanz-Medel, A., Gold Internal Standard Correction for Elemental Imaging of Soft Tissue Sections by LA-ICP-MS: Element Distribution in Eye Microstructures. *Anal. Bioanal. Chem.* **2013**, *405,* 3091-3096.

77. Latkoczy, C.; Günther, D., Enhanced Sensitivity in Inductively Coupled Plasma Sector Field Mass Spectrometry for Direct Solid Analysis Using Laser Ablation (La-Icp-Sfms). *J. Anal. At. Spectrom.* **2002**, *17,* 1264-1270.

78. Becker, J. S.; Breuer, U.; Hsieh, H. F.; Osterholt, T.; Kumtabtim, U.; Wu, B.; Matusch, A.; Caruso, J. A.; Qin, Z., Bioimaging of Metals and Biomolecules in Mouse Heart by Laser Ablation Inductively Coupled Plasma Mass Spectrometry and Secondary Ion Mass Spectrometry. *Anal. Chem.* **2010**, *82,* 9528-9533.

79. Clases, D.; Birka, M.; Sperling, M.; Faust, A.; Karst, U., Isobaric Dilution Analysis as a Calibration Tool for Long Lived Radionuclides in ICP-MS. *J. Trace Elem. Med. Biol.* **2017**, *40,* 97-103.

80. Pisonero, J.; Bouzas-Ramos, D.; Traub, H.; Cappella, B.; Álvarez-Llamas, C.; Richter, S.; Mayo, J. C.; Costa-Fernandez, J. M.; Bordel, N.; Jakubowski, N., Critical Evaluation of Fast and Highly Resolved Elemental Distribution in Single Cells Using LA-ICP-SFMS. *J. Anal. At. Spectrom.* **2019**, *34,* 655-663.

81. Waentig, L.; Jakubowski, N.; Roos, P. H., Multi-Parametric Analysis of Cytochrome P450 Expression in Rat Liver Microsomes by LA-ICP-MS. *J. Anal. At. Spectrom.* **2011**, *26,* 310-319.

82. Ardelt, D.; Polatajko, A.; Primm, O.; Reijnen, M., Isotope Ratio Measurements with a Fully Simultaneous Mattauch-Herzog ICP-MS. *Anal. Bioanal. Chem.* **2013**, *405,* 2987-2994.

83. Lobo, L.; Pereiro, R.; Fernández, B., Opportunities and Challenges of Isotopic Analysis by Laser Ablation ICP-MS in Biological Studies. *Trends Analyt. Chem.* **2018**, *105,* 380-390.

84. Urgast, D. S.; Feldmann, J., Isotope Ratio Measurements in Biological Tissues Using LA-ICP-MS – Possibilities, Limitations, and Perspectives. *J. Anal. At. Spectrom.* **2013**, *28,* 1367-1371.

85. Urgast, D. S.; Hill, S.; Kwun, I. S.; Beattie, J. H.; Goenaga-Infante, H.; Feldmann, J., Zinc Isotope Ratio Imaging of Rat Brain Thin Sections from Stable Isotope Tracer Studies by LA-MC-ICP-MS. *Metallomics* **2012**, *4,* 1057-1063.

86. Woodhead, J. D.; Hellstrom, J.; Hergt, J. M.; Greig, A.; Maas, R., Isotopic and Elemental Imaging of Geological Materials by Laser Ablation Inductively Coupled Plasma-Mass Spectrometry. *Geostand. Geoanal. Res.* **2007**, *31,* 331-343.

87. Thorrold, S. R.; Jones, G. P.; Planes, S.; Hare, J. A., Transgenerational Marking of Embryonic Otoliths in Marine Fishes Using Barium Stable Isotopes. *Can. J. Fish. Aquat. Sci.* **2006**, *63,* 1193-1197.

88. Huelga-Suarez, G.; Fernandez, B.; Moldovan, M.; Garcia Alonso, J. I., Detection of Transgenerational Barium Dual-Isotope Marks in Salmon Otoliths by Means of LA-ICP-MS. *Anal. Bioanal. Chem.* **2013**, *405,* 2901-2909.

89. Wang, Y. X.; Specht, A.; Horst, W. J., Stable Isotope Labelling and Zinc Distribution in Grains Studied by Laser Ablation ICP-MS in an Ear Culture System Reveals Zinc Transport Barriers During Grain Filling in Wheat. *New Phytol.* **2011**, *189,* 428-437.

90. Paul, B.; Paton, C.; Norris, A.; Woodhead, J.; Hellstrom, J.; Hergt, J.; Greig, A., Cellspace: A Module for Creating Spatially Registered Laser Ablation Images within the Iolite Freeware Environment. *J. Anal. At. Spectrom.* **2012**, *27,* 700-706.

91. Prohaska, T.; Irrgeher, J.; Zitek, A., Simultaneous Multi-Element and Isotope Ratio Imaging of Fish Otoliths by Laser Ablation Split Stream ICP-MS/MC ICP-MS. *J. Anal. At. Spectrom.* **2016**, *31,* 1612-1621.

92. Avigliano, E.; Pisonero, J.; Bouchez, J.; Pouilly, M.; Domanico, A.; Sánchez, S.; Clavijo, C.; Scarabotti, P.; Facetti, J. F.; Caffetti, J. D.; del Rosso, F. R.; Llamazares Vegh, S.; Volpedo, A. V., Otolith Sr/Ca Ratio Complements Sr Isotopes to Reveal Fish Migration in Large Basins with Heterogeneous Geochemical Landscapes. *Environ. Biol. Fishes* **2021**.

93. Copeland, S. R.; Sponheimer, M.; Ruiter, D. J. d.; Lee-Thorp, J. A.; Codron, D.; Roux, P. J. l.; Grimes, V.; Richards, M. P., Strontium Isotope Evidence for Landscape Use by Early Hominins. *Nature* **2011**, *474,* 76-78.

94. Resano, M.; Aramendía, M.; Rello, L.; Calvo, M. L.; Bérail, S.; Pécheyran, C., Direct Determination of Cu Isotope Ratios in Dried Urine Spots by Means of FS-LA-MC-ICPMS. Potential to Diagnose Wilson's Disease. *J. Anal. At. Spectrom.* **2013**, *28,* 98-106.

95. Hendriks, L.; Gundlach-Graham, A.; Hattendorf, B.; Günther, D., Characterization of a New ICP-TOFMS Instrument with Continuous and Discrete Introduction of Solutions. *J. Anal. At. Spectrom.* **2017**, *32,* 548-561.

96. Olsen, L. R.; Leipold, M. D.; Pedersen, C. B.; Maecker, H. T., The Anatomy of Single Cell Mass Cytometry Data. *Cytometry A* **2019**, *95,* 156-172.

97. Azimzada, A.; Farner, J. M.; Jreije, I.; Hadioui, M.; Liu-Kang, C.; Tufenkji, N.; Shaw, P.; Wilkinson, K. J., Single- and Multi-Element Quantification and Characterization of TiO_2 Nanoparticles Released from Outdoor Stains and Paints. *Frontiers in Environmental Science* **2020**, *8,* 91.

98. Myers, D. P.; Li, G.; Yang, P.; Hieftje, G. M., An Inductively Coupled Plasma-Time-of-Flight Mass Spectrometer for Elemental Analysis. Part I: Optimization and Characteristics. *J. Am. Soc. Mass Spectrom.* **1994**, *5,* 1008-1016.

99. Burger, M.; Hendriks, L.; Kaeslin, J.; Gundlach-Graham, A.; Hattendorf, B.; Günther, D., Characterization of Inductively Coupled Plasma Time-of-Flight Mass Spectrometry in Combination with Collision/Reaction Cell Technology – Insights from Highly Time-Resolved Measurements. *J. Anal. At. Spectrom.* **2019**, *34,* 135-146.

100. Monk, S. M.; Lev, S. M., Toxicological Applications of Cryogenic Laser Ablation Inductively Coupled Plasma Time of Flight Mass Spectrometry (CLA-ICP-TOF-MS). *J. Anal. At. Spectrom.* **2013**, *28,* 274-279.

101. Greenhalgh, C. J.; Voloaca, O. M.; Shaw, P.; Donard, A.; Cole, L. M.; Clench, M. R.; Managh, A. J.; Haywood-Small, S. L., Needles in Haystacks: Using Fast-Response LA Chambers and ICP-TOF-MS to Identify Asbestos Fibres in Malignant Mesothelioma Models. *J. Anal. At. Spectrom.* **2020**, *35,* 2231-2238.

102. Ijsselsteijn, M. E.; van der Breggen, R.; Farina Sarasqueta, A.; Koning, F.; de Miranda, N., A 40-Marker Panel for High Dimensional Characterization of Cancer Immune Microenvironments by Imaging Mass Cytometry. *Front. Immunol.* **2019**, *10,* 2534.

103. Gray, A. L., Solid Sample Introduction by Laser Ablation for Inductively Coupled Plasma Source Mass Spectrometry. *The Analyst* **1985**, *110,* 551-556.

104. Date, A. R., An Introduction to Inductively Coupled Plasma Source Mass Spectrometry. *Trends Analyt. Chem.* **1983**, *2,* 225-230.

105. Arrowsmith, P.; Hughes, S. K., Entrainment and Transport of Laser Ablated Plumes for Subsequent Elemental Analysis. *Appl. Spectrosc.* **2016**, *42,* 1231-1239.

106. Bleiner, D.; Günther, D., Theoretical Description and Experimental Observation of Aerosol Transport Processes in Laser Ablation Inductively Coupled Plasma Mass Spectrometry. *J. Anal. At. Spectrom.* **2001**, *16,* 449-456.

107. Tanner, M.; Günther, D., In Torch Laser Ablation Sampling for Inductively Coupled Plasma Time of Flight Mass Spectrometry. *J. Anal. At. Spectrom.* **2006**, *21,* 941-947.

108. Tanner, M.; Günther, D., In Torch Laser Ablation Sampling for Inductively Coupled Plasma Mass Spectrometry. *J. Anal. At. Spectrom.* **2005**, *20,* 987-989.

109. Liu, Y.; Hu, Z.; Yuan, H.; Hu, S.; Cheng, H., Volume-Optional and Low-Memory (VOLM) Chamber for Laser Ablation-ICP-MS: Application to Fiber Analyses. *J. Anal. At. Spectrom.* **2007**, *22,* 582-585.

110. Becker, J. S.; Gorbunoff, A.; Zoriy, M.; Izmer, A.; Kayser, M., Evidence of near-Field Laser Ablation Inductively Coupled Plasma Mass Spectrometry (NF-LA-ICP-MS) at Nanometre Scale for Elemental and Isotopic Analysis on Gels and Biological Samples. *J. Anal. At. Spectrom.* **2006**, *21,* 19-25.

111. Pushie, M. J.; Pickering, I. J.; Korbas, M.; Hackett, M. J.; George, G. N., Elemental and Chemically Specific X-Ray Fluorescence Imaging of Biological Systems. *Chem. Rev.* **2014**, *114,* 8499-84541.

112. Müller, W.; Shelley, M.; Miller, P.; Broude, S., Initial Performance Metrics of a New Custom-Designed Arf Excimer La-Icpms System Coupled to a Two-Volume Laser-Ablation Cell. *J. Anal. At. Spectrom.* **2009**, *24,* 209-214.

113. Šala, M.; Šelih, V. S.; Stremtan, C. C.; Teun van Elteren, J., Analytical Performance of a High-Repetition Rate Laser Head (500 Hz) for HR LA-ICP-QMS Imaging. *J. Anal. At. Spectrom.* **2020**, *35,* 1827-1831.

114. Douglas, D. N.; Managh, A. J.; Reid, H. J.; Sharp, B. L., High-Speed, Integrated Ablation Cell and Dual Concentric Injector Plasma Torch for Laser Ablation-Inductively Coupled Plasma Mass Spectrometry. *Anal. Chem.* **2015**, *87,* 11285-11294.

115. Wang, H. A.; Grolimund, D.; Giesen, C.; Borca, C. N.; Shaw-Stewart, J. R.; Bodenmiller, B.; Gunther, D., Fast Chemical Imaging at High Spatial Resolution by Laser Ablation Inductively Coupled Plasma Mass Spectrometry. *Anal. Chem.* **2013**, *85,* 10107-10116.

116. Gundlach-Graham, A.; Burger, M.; Allner, S.; Schwarz, G.; Wang, H. A.; Gyr, L.; Grolimund, D.; Hattendorf, B.; Gunther, D., High-Speed, High-Resolution, Multielemental Laser Ablation-Inductively Coupled Plasma-Time-of-Flight Mass Spectrometry Imaging: Part I. Instrumentation and Two-Dimensional Imaging of Geological Samples. *Anal. Chem.* **2015**, *87,* 8250-8258.

117. Burger, M.; Gundlach-Graham, A.; Allner, S.; Schwarz, G.; Wang, H. A.; Gyr, L.; Burgener, S.; Hattendorf, B.; Grolimund, D.; Gunther, D., High-Speed, High-Resolution, Multielemental LA-ICP-TOFMS Imaging: Part Ii. Critical Evaluation of

Quantitative Three-Dimensional Imaging of Major, Minor, and Trace Elements in Geological Samples. *Anal. Chem.* **2015**, *87,* 8259-8267.

118. van Malderen, S. J. M.; Managh, A. J.; Sharp, B. L.; Vanhaecke, F., Recent Developments in the Design of Rapid Response Cells for Laser Ablation-Inductively Coupled Plasma-Mass Spectrometry and Their Impact on Bioimaging Applications. *J. Anal. At. Spectrom.* **2016**, *31,* 423-439.

119. Malderen, S. J. M. V.; Acker, T. V.; Vanhaecke, F., Sub-Micrometer Nanosecond LA-ICP-MS Imaging at Pixel Acquisition Rates above 250 Hz Via a Low-Dispersion Setup. *Anal. Chem.* **2020**, *92,* 5756-5764.

120. Silva, M. d.; Arruda, M., Laser Ablation (Imaging) for Mapping and Determining Se and S in Sunflower Leaves. *Metallomics* **2012**, *5,* 62-67.

121. Wu, B.; Zoriy, M.; Chen, Y.; Becker, J. S., Imaging of Nutrient Elements in the Leaves of Elsholtzia Splendens by Laser Ablation Inductively Coupled Plasma Mass Spectrometry (LA-ICP-MS). *Talanta* **2009**, *78,* 132-137.

122. Schuchert, P. C.; Arkhipkin, A. I.; Koenig, A. E., Traveling around Cape Horn: Otolith Chemistry Reveals a Mixed Stock of Patagonian Hoki with Separate Atlantic and Pacific Spawning Grounds. *Fisheries Research* **2010**, *102,* 80-86.

123. D'Avignon, G.; Rose, G. A., Otolith Elemental Fingerprints Distinguish Atlantic Cod Spawning Areas in Newfoundland and Labrador. *Fisheries Research* **2013**, *147,* 1-9.

124. Vasconcelos, R. P.; Reis-Santos, P.; Tanner, S.; Maia, A.; Latkoczy, C.; Günther, D.; Costa, M. J.; Cabral, H., Evidence of Estuarine Nursery Origin of Five Coastal Fish Species Along the Portuguese Coast through Otolith Elemental Fingerprints. *Estuarine, Coastal and Shelf Science* **2008**, *79,* 317-327.

125. Flem, B.; Moen, V.; Grimstvedt, A., Trace Element Analysis of Scales from Four Populations of Norwegian Atlantic Salmon (Salmo Salar L.) for Stock Identification Using Laser Ablation Inductively Coupled Plasma Mass Spectrometry. *Appl. Spectrosc.* **2004**, *59,* 245-251.

126. Holá, M.; Kalvoda, J.; Nováková, H.; Škoda, R.; Kanický, V., Possibilities of LA-ICP-MS Technique for the Spatial Elemental Analysis of the Recent Fish Scales: Line Scan Vs. Depth Profiling. *Appl. Surf. Sci.* **2011**, *257,* 1932-1940.

127. Perkins, W. T.; Fuge, R.; Pearce, N. J. G., Quantitative Analysis of Trace Elements in Carbonates Using Laser Ablation Inductively Coupled Plasma Mass Spectrometry. *J. Anal. At. Spectrom.* **1991**, *6,* 445-449.

128. Jackson, B.; Harper, S.; Smith, L.; Flinn, J., Elemental Mapping and Quantitative Analysis of Cu, Zn, and Fe in Rat Brain Sections by Laser Ablation ICP-MS. *Anal. Bioanal. Chem.* **2006**, *384,* 951-957.

129. Wang, C. H., Otolith Elemental Ratios of Flathead Mullet Mugil Cephalus in Taiwanese Waters Reveal Variable Patterns of Habitat Use. *Estuarine, Coastal and Shelf Science* **2014**, *151,* 124-130.

130. Kemp, J.; Swearer, S. E.; Jenkins, G. P.; Robertson, S., Otolith Chemistry is More Accurate Than Otolith Shape in Identifying Cod Species (Genus Pseudophycis) in the Diet of Australian Fur Seals (Arctocephalus Pusillus Doriferus). *Can. J. Fish. Aquat. Sci.* **2011**, *68,* 1732-1743.

131. Ranaldi, M.; Gagnon, M., Trace Metal Incorporation in Otoliths of Pink Snapper (Pagrus Auratus) as an Environmental Monitor. *Comparative Biochemistry and Physiology Part C: Toxicology & Pharmacology* **2010**, *152,* 248-255.

132. Ranaldi, M. M.; Gagnon, M. M., Zinc Incorporation in the Otoliths of Juvenile Pink Snapper (Pagrus Auratus Forster): The Influence of Dietary Versus Waterborne Sources. *J. Exp. Mar. Biol. Ecol.* **2008**, *360,* 56-62.

133. Kaimal, B.; Johnson, R.; Hannigan, R., Distinguishing Breeding Populations of Mallards (Anas Platyrhynchos) Using Trace Elements. *J. Geochem. Explor.* **2009**, *102,* 44-48.

134. Ethier, D. M.; Kyle, C. J.; Nocera, J. J., Tracking Animal Movement by Comparing Trace Element Signatures in Claws to Spatial Variability of Elements in Soils. *Sci. Total Environ.* **2014**, 699-705.

135. Ethier, D. M.; Kyle, C. J.; Kyser, T. K.; Nocera, J. J., Trace Elements in Claw Keratin as Temporally Explicit Indicators of Geographic Origin in Terrestrial Mammals. *Ann. Zool. Fenn.* **2013**, *50,* 89-99.

136. Cucina, A.; Dudgeon, J.; Neff, H., Methodological Strategy for the Analysis of Human Dental Enamel by LA-ICP-MS. *J. Archaeol. Sci.* **2007**, *34,* 1884-1888.

137. Hare, D. J.; Lear, J.; Bishop, D.; Beavis, A.; Doble, P. A., Protocol for Production of Matrix-Matched Brain Tissue Standards for Imaging by Laser Ablation-Inductively Coupled Plasma-Mass Spectrometry. *Anal. Methods* **2013**, *5,* 1915-1921.

138. Becker, J. S.; Zoriy, M. V.; Pickhardt, C.; Palomero-Gallagher, N.; Zilles, K., Imaging of Copper, Zinc, and Other Elements in Thin Section of Human Brain Samples (Hippocampus) by Laser Ablation Inductively Coupled Plasma Mass Spectrometry. *Anal. Chem.* **2005**, *77,* 3208-3216.

139. New, E. J.; Wimmer, V. C.; Hare, D. J., Promises and Pitfalls of Metal Imaging in Biology. *Cell Chem. Biol.* **2018**, *25,* 7-18.

140. Westerhausen, M. T.; Lockwood, T. E.; Gonzalez de Vega, R.; Rohnelt, A.; Bishop, D. P.; Cole, N.; Doble, P. A.; Clases, D., Low Background Mould-Prepared Gelatine Standards for Reproducible Quantification in Elemental Bio-Imaging. *Analyst* **2019**, *144,* 6881-6888.

141. Hare, D. J.; George, J. L.; Grimm, R.; Wilkins, S.; Adlard, P. A.; Cherny, R. A.; Bush, A. I.; Finkelstein, D. I.; Doble, P., Three-Dimensional Elemental Bio-Imaging of Fe, Zn, Cu, Mn and P in a 6-Hydroxydopamine Lesioned Mouse Brain. *Metallomics* **2010**, *2,* 745-753.

142. González de Vega, R.; Fernández-Sánchez, M. L.; Pisonero, J.; Eiró, N.; Vizoso, F. J.; Sanz-Medel, A., Quantitative Bioimaging of Ca, Fe, Cu and Zn in Breast Cancer Tissues by LA-ICP-MS. *J. Anal. At. Spectrom.* **2017**, *32,* 671-677.

143. Bonta, M.; Lohninger, H.; Marchetti-Deschmann, M.; Limbeck, A., Application of Gold Thin-Films for Internal Standardization in LA-ICP-MS Imaging Experiments. *Analyst* **2013**, *139,* 1521-1531.

144. Reifschneider, O.; Wentker, K. S.; Strobel, K.; Schmidt, R.; Masthoff, M.; Sperling, M.; Faber, C.; Karst, U., Elemental Bioimaging of Thulium in Mouse Tissues by Laser Ablation-Icpms as a Complementary Method to Heteronuclear Proton Magnetic Resonance Imaging for Cell Tracking Experiments. *Anal. Chem.* **2015**, *87,* 4225-4230.

145. Reifschneider, O.; Wehe, C. A.; Raj, I.; Ehmcke, J.; Ciarimboli, G.; Sperling, M.; Karst, U., Quantitative Bioimaging of Platinum in Polymer Embedded Mouse Organs Using Laser Ablation ICP-MS. *Metallomics* **2013**, *5,* 1440-1447.

146. Austin, C.; Hare, D.; Rawling, T.; McDonagh, A. M.; Doble, P., Quantification Method for Elemental Bio-Imaging by LA-ICP-MS Using Metal Spiked Pmma Films. *J. Anal. At. Spectrom.* **2010**, *25,* 722-725.

147. Sala, M.; Selih, V. S.; van Elteren, J. T., Gelatin Gels as Multi-Element Calibration Standards in LA-ICP-MS Bioimaging: Fabrication of Homogeneous Standards and Microhomogeneity Testing. *Analyst* **2017**, *142,* 3356-3359.

148. Stärk, H. J.; Wennrich, R., A New Approach for Calibration of Laser Ablation Inductively Coupled Plasma Mass Spectrometry Using Thin Layers of Spiked Agarose Gels as References. *Anal. Bioanal. Chem.* **2011**, *399,* 2211-2217.

149. Birka, M.; Wentker, K. S.; Lusmoller, E.; Arheilger, B.; Wehe, C. A.; Sperling, M.; Stadler, R.; Karst, U., Diagnosis of Nephrogenic Systemic Fibrosis by Means of Elemental Bioimaging and Speciation Analysis. *Anal. Chem.* **2015**, *87,* 3321-3328.

150. Limbeck, A.; Galler, P.; Bonta, M.; Bauer, G.; Nischkauer, W.; Vanhaecke, F., Recent Advances in Quantitative LA-ICP-MS Analysis: Challenges and Solutions in the Life Sciences and Environmental Chemistry. *Anal. Bioanal. Chem.* **2015**, *407,* 6593-617.

151. Austin, C.; Fryer, F.; Lear, J.; Bishop, D.; Hare, D.; Rawling, T.; Kirkup, L.; McDonagh, A.; Doble, P., Factors Affecting Internal Standard Selection for Quantitative Elemental Bio-Imaging of Soft Tissues by LA-ICP-MS. *J. Anal. At. Spectrom.* **2011**, *26,* 1494-1501.

152. Todolí, J. L.; Mermet, J. M., Study of Polymer Ablation Products Obtained by Ultraviolet Laser Ablation — Inductively Coupled Plasma Atomic Emission Spectrometry. *Spectrochim. Acta Part B At. Spectrosc.* **1998**, *53,* 1645-1656.

153. Frick, D. A.; Günther, D., Fundamental Studies on the Ablation Behaviour of Carbon in LA-ICP-MS with Respect to the Suitability as Internal Standard. *J. Anal. At. Spectrom.* **2012**, *27,* 1294-1303.

154. Grijalba, N.; Legrand, A.; Holler, V.; Bouvier-Capely, C., A Novel Calibration Strategy Based on Internal Standard-Spiked Gelatine for Quantitative Bio-Imaging by LA-ICP-MS: Application to Renal Localization and Quantification of Uranium. *Anal. Bioanal. Chem.* **2020**, *412,* 3113-3122.

155. O'Reilly, J.; Douglas, D.; Braybrook, J.; So, P. W.; Vergucht, E.; Garrevoet, J.; Vekemans, B.; Vincze, L.; Goenaga-Infante, H., A Novel Calibration Strategy for the Quantitative Imaging of Iron in Biological Tissues by LA-ICP-MS Using Matrix-Matched Standards and Internal Standardisation. *J. Anal. At. Spectrom.* **2014**, *29,* 1378-1384.

156. Rodríguez-González, P.; Marchante-Gayón, J. M.; García Alonso, J. I.; Sanz-Medel, A., Isotope Dilution Analysis for Elemental Speciation: A Tutorial Review. *Spectrochim. Acta Part B At. Spectrosc.* **2005**, *60,* 151-207.

157. Heilmann, J.; Boulyga, S. F.; Heumann, K. G., Development of an Isotope Dilution Laser Ablation ICP-MS Method for Multi-Element Determination in Crude and Fuel Oil Samples. *J. Anal. At. Spectrom.* **2009**, *24,* 385-390.

158. Moraleja, I.; Mena, M. L.; Lázaro, A.; Neumann, B.; Tejedor, A.; Jakubowski, N.; Gómez-Gómez, M. M.; Esteban-Fernández, D., An Approach for Quantification of Platinum Distribution in Tissues by LA-ICP-MS Imaging Using Isotope Dilution Analysis. *Talanta* **2018**, *178,* 166-171.

159. Feng, L.; Wang, J.; Li, H.; Luo, X.; Li, J., A Novel Absolute Quantitative Imaging Strategy of Iron, Copper and Zinc in Brain Tissues by Isotope Dilution Laser Ablation ICP-MS. *Anal. Chim. Acta* **2017**, *984,* 66-75.

160. Thieleke, J. P.; Vogt, C., A Calibration Strategy for LA-ICP-MS Using Isotope Dilution for Solid Reference Materials. *J. Anal. At. Spectrom.* **2016**, *31,* 1198-1205.

161. Fernandez, B.; Rodriguez-Gonzalez, P.; Garcia Alonso, J. I.; Malherbe, J.; Garcia-Fonseca, S.; Pereiro, R.; Sanz-Medel, A., On-Line Double Isotope Dilution Laser

Ablation Inductively Coupled Plasma Mass Spectrometry for the Quantitative Analysis of Solid Materials. *Anal. Chim. Acta* **2014**, *851,* 64-71.

162. Bauer, O. B.; Koppen, C.; Sperling, M.; Schurek, H. J.; Ciarimboli, G.; Karst, U., Quantitative Bioimaging of Platinum Via Online Isotope Dilution-Laser Ablation-Inductively Coupled Plasma Mass Spectrometry. *Anal. Chem.* **2018**, *90,* 7033-7039.

163. Pickhardt, C.; Izmer, A. V.; Zoriy, M. V.; Schaumlöffel, D.; Sabine Becker, J., On-Line Isotope Dilution in Laser Ablation Inductively Coupled Plasma Mass Spectrometry Using a Microflow Nebulizer Inserted in the Laser Ablation Chamber. *Int. J. Mass Spectrom.* **2006**, *248,* 136-141.

164. Becker, J. S.; Pickhardt, C.; Pompe, W., Determination of Ag, Tl, and Pb in Few Milligrams of Platinum Nanoclusters by on-Line Isotope Dilution in Laser Ablation Inductively Coupled Plasma Mass Spectrometry. *Int. J. Mass Spectrom.* **2004**, *237,* 13-17.

165. Douglas, D. N.; O'Reilly, J.; O'Connor, C.; Sharp, B. L.; Goenaga-Infante, H., Quantitation of the Fe Spatial Distribution in Biological Tissue by Online Double Isotope Dilution Analysis with LA-ICP-MS: A Strategy for Estimating Measurement Uncertainty. *J. Anal. At. Spectrom.* **2016**, *31,* 270-279.

166. Clases, D.; Gonzalez de Vega, R.; Adlard, P. A.; Doble, P. A., On-Line Reverse Isotope Dilution Analysis for Spatial Quantification of Elemental Labels Used in Immunohistochemical Assisted Imaging Mass Spectrometry Via LA-ICP-MS. *J. Anal. At. Spectrom.* **2019**, *34,* 407-412.

167. Pozebon, D.; Scheffler, G. L.; Dressler, V. L., Recent Applications of Laser Ablation Inductively Coupled Plasma Mass Spectrometry (LA-ICP-MS) for Biological Sample Analysis: A Follow-up Review. *J. Anal. At. Spectrom.* **2017**, *32,* 890-919.

168. Pozebon, D.; Scheffler, G. L.; Dressler, V. L.; Nunes, M. A. G., Review of the Applications of Laser Ablation Inductively Coupled Plasma Mass Spectrometry (LA-ICP-MS) to the Analysis of Biological Samples. *J. Anal. At. Spectrom.* **2014**, *29,* 2204-2228.

169. Gammoh, N. Z.; Rink, L., Zinc in Infection and Inflammation. *Nutrients* **2017**, *9,* 624.

170. Engelken, J.; Altmeyer, M.; Franklin, R. B., The Disruption of Trace Element Homeostasis Due to Aneuploidy as a Unifying Theme in the Etiology of Cancer. *bioRxiv* **2014**, 002105.

171. Fischer-Fodor, E.; Miklasova, N.; Berindan-Neagoe, I.; Saha, B., Iron, Inflammation and Invasion of Cancer Cells. *Clujul Med* **2015**, *88,* 272-7.

172. Luca, A. D.; Barile, A.; Arciello, M.; Rossi, L., Copper Homeostasis as Target of Both Consolidated and Innovative Strategies of Anti-Tumor Therapy. *J. Trace Elem. Med. Biol.* **2019**, *55,* 204-213.

173. Klein, C. B.; Frenkel, K.; Costa, M., The Role of Oxidative Processes in Metal Carcinogenesis. *Chem. Res. Toxicol.* **1991**, *4,* 592-604.

174. Rosenberg, B.; VanCamp, L.; Trosko, J. E.; Mansour, V. H., Platinum Compounds: A New Class of Potent Antitumour Agents. *Nature* **1969**, *222,* 385-386.

175. Ndagi, U.; Mhlongo, N.; Soliman, M. E., Metal Complexes in Cancer Therapy - an Update from Drug Design Perspective. *Drug Des. Devel. Ther.* **2017**, *11,* 599-616.

176. Becker, J. S.; Zoriy, M. V.; Dehnhardt, M.; Pickhardt, C.; Zilles, K., Copper, Zinc, Phosphorus and Sulfur Distribution in Thin Section of Rat Brain Tissues Measured by Laser Ablation Inductively Coupled Plasma Mass Spectrometry: Possibility for Small-Size Tumor Analysis. *J. Anal. At. Spectrom.* **2005**, *20,* 912-917.

177. Zoriy, M. V.; Dehnhardt, M.; Reifenberger, G.; Zilles, K.; Becker, J. S., Imaging of Cu, Zn, Pb and U in Human Brain Tumor Resections by Laser Ablation Inductively Coupled Plasma Mass Spectrometry. *Int. J. Mass Spectrom.* **2006**, *257,* 27-33.

178. Hsieh, Y.-K.; Jiang, P.-S.; Yang, B.-S.; Sun, T.-Y.; Peng, H.-H.; Wang, C.-F., Using Laser Ablation/Inductively Coupled Plasma Mass Spectrometry to Bioimage Multiple Elements in Mouse Tumors after Hyperthermia. *Anal. Bioanal. Chem.* **2011**, *401,* 909-915.

179. Riesop, D.; Hirner, A. V.; Rusch, P.; Bankfalvi, A., Zinc Distribution within Breast Cancer Tissue: A Possible Marker for Histological Grading? *J. Cancer Res. Clin. Oncol.* **2015**, *141,* 1321-1331.

180. Doble, P. A.; Miklos, G. L., Distributions of Manganese in Diverse Human Cancers Provide Insights into Tumour Radioresistance. *Metallomics* **2018**, *10,* 1191-1210.

181. Gregory, E. M.; Fridovich, I., Oxygen Metabolism in Lactobacillus Plantarum. *J. Bacteriol.* **1974**, *117,* 166-169.

182. Archibald, F. S.; Fridovich, I., Manganese and Defenses against Oxygen Toxicity in Lactobacillus Plantarum. *J. Bacteriol.* **1981**, *145,* 442-451.

183. Hare, D.; Burger, F.; Austin, C.; Fryer, F.; Grimm, R.; Reedy, B.; Scolyer, R. A.; Thompson, J. F.; Doble, P., Elemental Bio-Imaging of Melanoma in Lymph Node Biopsies. *Analyst* **2009**, *134,* 450-453.

184. Zhang, X.; Liu, R.; Yuan, Q.; Gao, F.; Li, J.; Zhang, Y.; Zhao, Y.; Chai, Z.; Gao, L.; Gao, X., The Precise Diagnosis of Cancer Invasion/Metastasis Via 2d Laser Ablation Mass Mapping of Metalloproteinase in Primary Cancer Tissue. *ACS Nano* **2018**, *12,* 11139-11151.

185. Vega, R. G. d.; Clases, D.; Fernández-Sánchez, M. L.; Eiró, N.; González, L. O.; Vizoso, F. J.; Doble, P. A.; Sanz-Medel, A., Mmp-11 as a Biomarker for Metastatic Breast Cancer by Immunohistochemical-Assisted Imaging Mass Spectrometry. *Anal. Bioanal. Chem.* **2019**, *411,* 639-646.

186. Costas-Rodriguez, M.; Colina-Vegas, L.; Solovyev, N.; De Wever, O.; Vanhaecke, F., Cellular and Sub-Cellular Cu Isotope Fractionation in the Human Neuroblastoma Sh-Sy5y Cell Line: Proliferating Versus Neuron-Like Cells. *Anal. Bioanal. Chem.* **2019**, *411,* 4963-4971.

187. Zoriy, M.; Matusch, A.; Spruss, T.; Becker, J. S., Laser Ablation Inductively Coupled Plasma Mass Spectrometry for Imaging of Copper, Zinc, and Platinum in Thin Sections of a Kidney from a Mouse Treated with Cis-Platin. *Int. J. Mass Spectrom.* **2007**, *260,* 102-106.

188. Hartmann, J. T.; Kollmannsberger, C.; Kanz, L.; Bokemeyer, C., Platinum Organ Toxicity and Possible Prevention in Patients with Testicular Cancer. *Int. J. Cancer* **1999**, *83,* 866-869.

189. Bianga, J.; Bouslimani, A.; Bec, N.; Quenet, F.; Mounicou, S.; Szpunar, J.; Bouyssiere, B.; Lobinski, R.; Larroque, C., Complementarity of Maldi and La Icp Mass Spectrometry for Platinum Anticancer Imaging in Human Tumor. *Metallomics* **2014**, *6,* 1382-1386.

190. Carlier, C.; Laforce, B.; Van Malderen, S. J. M.; Gremonprez, F.; Tucoulou, R.; Villanova, J.; De Wever, O.; Vincze, L.; Vanhaecke, F.; Ceelen, W., Nanoscopic Tumor Tissue Distribution of Platinum after Intraperitoneal Administration in a Xenograft Model of Ovarian Cancer. *J. Pharm. Biomed. Anal.* **2016**, *131,* 256-262.

191. Egger, A. E.; Kornauth, C.; Haslik, W.; Hann, S.; Theiner, S.; Bayer, G.; Hartinger, C. G.; Keppler, B. K.; Pluschnig, U.; Mader, R. M., Extravasation of Pt-Based

Chemotherapeutics – Bioimaging of Their Distribution in Resectates Using Laser Ablation-Inductively Coupled Plasma-Mass Spectrometry (LA-ICP-MS). *Metallomics* **2015**, *7,* 508-515.

192.   Theiner, S.; Kornauth, C.; Varbanov, H. P.; Galanski, M.; Schoonhoven, S. V.; Heffeter, P.; Berger, W.; Egger, A. E.; Keppler, B. K., Tumor Microenvironment in Focus: LA-ICP-MS Bioimaging of a Preclinical Tumor Model Upon Treatment with Platinum(Iv)-Based Anticancer Agents. *Metallomics* **2015**, *7,* 1256-1264.

193.   Lum, T.-S.; Ho, C.-L.; Tsoi, Y.-K.; Siu, C.-H.; Yue, P. Y.-K.; Wong, W.-Y.; Leung, K. S.-Y., Elemental Bioimaging of Platinum in Mouse Tissues by Laser Ablation-Inductively Coupled Plasma-Mass Spectrometry for the Study of Localization Behavior of Structurally Similar Complexes. *Int. J. Mass Spectrom.* **2016**, *404,* 40-47.

194.   Hucke, A.; Rinschen, M. M.; Bauer, O. B.; Sperling, M.; Karst, U.; Koppen, C.; Sommer, K.; Schroter, R.; Ceresa, C.; Chiorazzi, A.; Canta, A.; Semperboni, S.; Marmiroli, P.; Cavaletti, G.; Schlatt, S.; Schlatter, E.; Pavenstadt, H.; Heitplatz, B.; Van Marck, V.; Sparreboom, A.; Barz, V.; Knief, A.; Deuster, D.; Zehnhoff-Dinnesen, A. A.; Ciarimboli, G., An Integrative Approach to Cisplatin Chronic Toxicities in Mice Reveals Importance of Organic Cation-Transporter-Dependent Protein Networks for Renoprotection. *Arch. Toxicol.* **2019**, *93,* 2835-2848.

195.   Niehoff, A. C.; Grunebaum, J.; Moosmann, A.; Mulac, D.; Sobbing, J.; Niehaus, R.; Buchholz, R.; Kroger, S.; Wiehe, A.; Wagner, S.; Sperling, M.; von Briesen, H.; Langer, K.; Karst, U., Quantitative Bioimaging of Platinum Group Elements in Tumor Spheroids. *Anal. Chim. Acta* **2016**, *938,* 106-113.

196.   Theiner, S.; Malderen, S. J. M.; Acker, T.; Legin, A. A.; Keppler, B. K.; Vanhaecke, F.; Koellensperger, G., Fast High-Resolution LA-ICP-MS Imaging of the Distribution of Platinum-Based Anti-Cancer Compounds in Multicellular Tumor Spheroids. *Anal. Chem.* **2017**, *89,* 12641-12645.

197.   Van Malderen, S. J.; van Elteren, J. T.; Vanhaecke, F., Submicrometer Imaging by Laser Ablation-Inductively Coupled Plasma Mass Spectrometry Via Signal and Image Deconvolution Approaches. *Anal. Chem.* **2015**, *87,* 6125-6132.

198.   Klose, M. H. M.; Theiner, S.; Kornauth, C.; Meier-Menches, S. M.; Heffeter, P.; Berger, W.; Koellensperger, G.; Keppler, B. K., Bioimaging of Isosteric Osmium and Ruthenium Anticancer Agents by LA-ICP-MS. *Metallomics* **2018**, *10,* 388-396.

199.   McCall, A. S.; Cummings, C. F.; Bhave, G.; Vanacore, R.; Page-McCaw, A.; Hudson, B. G., Bromine Is an Essential Trace Element for Assembly of Collagen Iv Scaffolds in Tissue Development and Architecture. *Cell* **2014**, *157,* 1380-1392.

200.   Rodriguez-Moro, G.; Ramirez-Acosta, S.; Arias-Borrego, A.; Garcia-Barrera, T.; Gomez-Ariza, J. L., Environmental Metallomics. *Adv. Exp. Med. Biol.* **2018**, *1055,* 39-66.

201.   Heffernan, A. L.; Hare, D. J., Tracing Environmental Exposure from Neurodevelopment to Neurodegeneration. *Trends Neurosci.* **2018**, *41,* 496-501.

202.   Clarkson, T. W., The Toxicology of Mercury. *Crit. Rev. Clin. Lab. Sci.* **2008**, *34,* 369-403.

203.   Rutkowska, M.; Dubalska, K.; Bajger-Nowak, G.; Konieczka, P.; Namieśnik, J., Organomercury Compounds in Environmental Samples: Emission Sources, Toxicity, Environmental Fate, and Determination. *Crit. Rev. Environ. Sci. Technol.* **2014**, *44,* 638-704.

204.   Barst, B. D.; Gevertz, A. K.; Chumchal, M. M.; Smith, J. D.; Rainwater, T. R.; Drevnick, P. E.; Hudelson, K. E.; Hart, A.; Verbeck, G. F.; Roberts, A. P., Laser Ablation ICP-MS

Co-Localization of Mercury and Immune Response in Fish. *Environ Sci Technol* **2011**, *45,* 8982-8988.

205. Niehoff, A. C.; Bauer, O. B.; Kroger, S.; Fingerhut, S.; Schulz, J.; Meyer, S.; Sperling, M.; Jeibmann, A.; Schwerdtle, T.; Karst, U., Quantitative Bioimaging to Investigate the Uptake of Mercury Species in Drosophila Melanogaster. *Anal. Chem.* **2015**, *87,* 10392-10396.

206. Pamphlett, R.; Satgunaseelan, L.; Jew, S. K.; Doble, P. A.; Bishop, D. P., Elemental Bioimaging Shows Mercury and Other Toxic Metals in Normal Breast Tissue and in Breast Cancers. *PLoS One* **2020**, *15,* e0228226.

207. Pamphlett, R.; Kum Jew, S.; Doble, P. A.; Bishop, D. P., Elemental Analysis of Aging Human Pituitary Glands Implicates Mercury as a Contributor to the Somatopause. *Front. Endocrinol (Lausanne)* **2019**, *10,* 419.

208. Niehoff, A. C.; Schulz, J.; Soltwisch, J.; Meyer, S.; Kettling, H.; Sperling, M.; Jeibmann, A.; Dreisewerd, K.; Francesconi, K. A.; Schwerdtle, T.; Karst, U., Imaging by Elemental and Molecular Mass Spectrometry Reveals the Uptake of an Arsenolipid in the Brain of Drosophila Melanogaster. *Anal. Chem.* **2016**, *88,* 5258-63.

209. Eijkelkamp, B. A.; Morey, J. R.; Neville, S. L.; Tan, A.; Pederick, V. G.; Cole, N.; Singh, P. P.; Ong, C. Y.; Gonzalez de Vega, R.; Clases, D.; Cunningham, B. A.; Hughes, C. E.; Comerford, I.; Brazel, E. B.; Whittall, J. J.; Plumptre, C. D.; McColl, S. R.; Paton, J. C.; McEwan, A. G.; Doble, P. A.; McDevitt, C. A., Dietary Zinc and the Control of Streptococcus Pneumoniae Infection. *PLoS Pathog.* **2019**, *15,* e1007957.

210. Hare, D.; Tolmachev, S.; James, A.; Bishop, D.; Austin, C.; Fryer, F.; Doble, P., Elemental Bio-Imaging of Thorium, Uranium, and Plutonium in Tissues from Occupationally Exposed Former Nuclear Workers. *Anal. Chem.* **2010**, *82,* 3176-3182.

211. M-M, P.; Weiskirchen, R.; Gassler, N.; Bosserhoff, A. K.; Becker, J. S., Novel Bioimaging Techniques of Metals by Laser Ablation Inductively Coupled Plasma Mass Spectrometry for Diagnosis of Fibrotic and Cirrhotic Liver Disorders. *PLoS One* **2013**, *8,* e58702.

212. Togao, M.; Nakayama, S. M. M.; Ikenaka, Y.; Mizukawa, H.; Makino, Y.; Kubota, A.; Matsukawa, T.; Yokoyama, K.; Hirata, T.; Ishizuka, M., Bioimaging of Pb and Stim1 in Mice Liver, Kidney and Brain Using Laser Ablation Inductively Coupled Plasma Mass Spectrometry (LA-ICP-MS) and Immunohistochemistry. *Chemosphere*, **2020**, *238*, 124581.

213. Yamagishi, Y.; Furukawa, S.; Tanaka, A.; Kobayashi, Y.; Sugiyama, A., Histopathological Localization of Cadmium in Rat Placenta by LA-ICP-MS Analysis. *J. Toxicol. Pathol.* **2016**, *29,* 279-283.

214. Mercan, S.; Ellez, S. Z.; Türkmen, Z.; Yayla, M.; Cengiz, S., Quantitative Lead Determination in Coating Paint on Children'S Outwear by LA-ICP-MS: A Practical Calibration Strategy for Solid Samples. *Talanta* **2015**, *132,* 222-227.

215. Bolker, J., There's More to Life Than Rats and Flies. *Nature* **2012**, *491,* 31-33.

216. Persson, D. P.; Chen, A.; Aarts, M. G.; Salt, D. E.; Schjoerring, J. K.; Husted, S., Multi-Element Bioimaging of Arabidopsis Thaliana Roots. *Plant Physiol.* **2016**, *172,* 835-847.

217. Hare, D. J.; Jones, M. W. M.; Wimmer, V. C.; Jenkins, N. L.; Jonge, M. D. d.; Bush, A. I.; McColl, G., High-Resolution Complementary Chemical Imaging of Bio-Elements in Caenorhabditis Elegans. *Metallomics* **2015**, *8,* 156-160.

218. Crone, B.; Aschner, M.; Schwerdtle, T.; Karst, U.; Bornhorst, J., Elemental Bioimaging of Cisplatin in Caenorhabditis Elegans by LA-ICP-MS. *Metallomics* **2015**, *7,* 1189-1195.

130

219. Böhme, S.; Stärk, H.-J.; Kühnel, D.; Reemtsma, T., Exploring LA-ICP-MS as a Quantitative Imaging Technique to Study Nanoparticle Uptake in Daphnia Magna and Zebrafish (Danio Rerio) Embryos. *Anal. Bioanal. Chem.* **2015**, *407,* 5477-5485.

220. Halbach, K.; Wagner, S.; Scholz, S.; Luckenbach, T.; Reemtsma, T., Elemental Imaging (LA-ICP-MS) of Zebrafish Embryos to Study the Toxicokinetics of the Acetylcholinesterase Inhibitor Naled. *Anal. Bioanal. Chem.* **2019**, *411,* 617-627.

221. Gholap, D. S.; Izmer, A.; De Samber, B.; van Elteren, J. T.; Selih, V. S.; Evens, R.; De Schamphelaere, K.; Janssen, C.; Balcaen, L.; Lindemann, I.; Vincze, L.; Vanhaecke, F., Comparison of Laser Ablation-Inductively Coupled Plasma-Mass Spectrometry and Micro-X-Ray Fluorescence Spectrometry for Elemental Imaging in Daphnia Magna. *Anal. Chim. Acta* **2010**, *664,* 19-26.

222. Santos, M. C.; Wagner, M.; Wu, B.; Scheider, J.; Oehlmann, J.; Cadore, S.; Becker, J. S., Biomonitoring of Metal Contamination in a Marine Prosobranch Snail (Nassarius Reticulatus) by Imaging Laser Ablation Inductively Coupled Plasma Mass Spectrometry (LA-ICP-MS). *Talanta* **2009**, *80,* 428-433.

223. Bohme, S.; Stark, H. J.; Meissner, T.; Springer, A.; Reemtsma, T.; Kuhnel, D.; Busch, W., Quantification of Al_2O_3 Nanoparticles in Human Cell Lines Applying Inductively Coupled Plasma Mass Spectrometry (Neb-ICP-MS, LA-ICP-MS) and Flow Cytometry-Based Methods. *J Nanopart Res* **2014**, *16,* 2592.

224. Beeckman, T.; Viane, R., Embedding Thin Plant Specimens for Oriented Sectioning. *Biotech. Histochem.* **2009**, *75,* 23-26.

225. Siebold, M.; Leidich, P.; Bertini, M.; Deflorio, G.; Feldmann, J.; Krupp, E. M.; Halmschlager, E.; Woodward, S., Application of Elemental Bioimaging Using Laser Ablation ICP-MS in Forest Pathology: Distribution of Elements in the Bark of Picea Sitchensis Following Wounding. *Anal. Bioanal. Chem.* **2012**, *402,* 3323-3331.

226. Papaslioti, E. M.; Parviainen, A.; Roman Alpiste, M. J.; Marchesi, C.; Garrido, C. J., Quantification of Potentially Toxic Elements in Food Material by Laser Ablation-Inductively Coupled Plasma-Mass Spectrometry (LA-ICP-MS) via Pressed Pellets. *Food Chem.* **2019**, *274,* 726-732.

227. Narewski, U.; Werner, G.; Schulz, H.; Vogt, C., Application of Laser Ablation Inductively Coupled Mass Spectrometry (LA-ICP-MS) for the Determination of Major, Minor, and Trace Elements in Bark Samples. *Fresenius. J. Anal. Chem.* **2000**, *366,* 167-170.

228. Becker, J. S.; Dietrich, R. C.; Matusch, A.; Pozebon, D.; Dressler, V. L., Quantitative Images of Metals in Plant Tissues Measured by Laser Ablation Inductively Coupled Plasma Mass Spectrometry. *Spectrochim. Acta Part B At. Spectrosc.* **2008**, *63,* 1248-1252.

229. Kaiser, J.; Galiová, M.; Novotný, K.; Červenka, R.; Reale, L.; Novotný, J.; Liška, M.; Samek, O.; Kanický, V.; Hrdlička, A.; Stejskal, K.; Adam, V.; Kizek, R., Mapping of Lead, Magnesium and Copper Accumulation in Plant Tissues by Laser-Induced Breakdown Spectroscopy and Laser-Ablation Inductively Coupled Plasma Mass Spectrometry. *Spectrochim. Acta Part B At. Spectrosc.* **2009**, *64,* 67-73.

230. Hanć, A.; Piechalak, A.; Tomaszewska, B.; Barałkiewicz, D., Laser Ablation Inductively Coupled Plasma Mass Spectrometry in Quantitative Analysis and Imaging of Plant's Thin Sections. *Int. J. Mass Spectrom.* **2014**, *363,* 16-22.

231. Koelmel, J.; Amarasiriwardena, D., Imaging of Metal Bioaccumulation in Hay-Scented Fern (Dennstaedtia Punctilobula) Rhizomes Growing on Contaminated Soils by Laser Ablation ICP-MS. *Environ. Pollut.* **2012**, *168,* 62-70.

232. Diaz-Benito, P.; Banakar, R.; Rodriguez-Menendez, S.; Capell, T.; Pereiro, R.; Christou, P.; Abadia, J.; Fernandez, B.; Alvarez-Fernandez, A., Iron and Zinc in the Embryo and Endosperm of Rice (Oryza Sativa L.) Seeds in Contrasting 2'-Deoxymugineic Acid/Nicotianamine Scenarios. *Front Plant Sci* **2018**, *9,* 1190.

233. Imran, M.; Garbe-Schönberg, D.; Neumann, G.; Boelt, B.; Mühling, K. H., Zinc Distribution and Localization in Primed Maize Seeds and Its Translocation During Early Seedling Development. *Environ. Exp. Bot.* **2017**, *143,* 91-98.

234. Wu, B.; Chen, Y.; Becker, J. S., Study of Essential Element Accumulation in the Leaves of a Cu-Tolerant Plant Elsholtzia Splendens after Cu Treatment by Imaging Laser Ablation Inductively Coupled Plasma Mass Spectrometry (LA-ICP-MS). *Anal. Chim. Acta* **2009**, *633,* 165-72.

235. Van Malderen, S. J. M.; Laforce, B.; Van Acker, T.; Vincze, L.; Vanhaecke, F., Imaging the 3D Trace Metal and Metalloid Distribution in Mature Wheat and Rye Grains Via Laser Ablation-Icp-Mass Spectrometry and Micro-X-Ray Fluorescence Spectrometry. *J. Anal. At. Spectrom.* **2017**, *32,* 289-298.

236. Persson, D. P.; de Bang, T. C.; Pedas, P. R.; Kutman, U. B.; Cakmak, I.; Andersen, B.; Finnie, C.; Schjoerring, J. K.; Husted, S., Molecular Speciation and Tissue Compartmentation of Zinc in Durum Wheat Grains with Contrasting Nutritional Status. *New Phytol.* **2016**, *211,* 1255-1265.

237. Galiová, M.; Kaiser, J.; Novotný, K.; Novotný, J.; Vaculovič, T.; Liška, M.; Malina, R.; Stejskal, K.; Adam, V.; Kizek, R., Investigation of Heavy-Metal Accumulation in Selected Plant Samples Using Laser Induced Breakdown Spectroscopy and Laser Ablation Inductively Coupled Plasma Mass Spectrometry. *Applied Physics A* **2008**, *93,* 917-922.

238. Zhu, Y.; Hioki, A.; Itoh, A.; Umemura, T.; Haraguchi, H.; Chiba, K., Relative Enrichment of Mo in the Radicle of Peanut Seed (Arachis Hypogaea), Observed by Multi-Elemental Imagining with LA-ICP-MS. *Anal. Sci.* **2012**, *28,* 1121-1124.

239. Lefèvre, I.; Vogel‑MikuŠ, K.; Jeromel, L.; VavpetiČ, P.; Planchon, S.; ArČOn, I.; Elteren, J. T. V.; Lepoint, G.; Gobert, S.; Renaut, J.; Pelicon, P.; Lutts, S., Differential Cadmium and Zinc Distribution in Relation to Their Physiological Impact in the Leaves of the Accumulating Zygophyllum Fabago L. *Plant, Cell Environ.* **2014**, *37,* 1299-1320.

240. Callahan, D. L.; Hare, D. J.; Bishop, D. P.; Doble, P. A.; Roessner, U., Elemental Imaging of Leaves from the Metal Hyperaccumulating Plant Noccaea Caerulescens Shows Different Spatial Distribution of Ni, Zn and Cd. *RSC Adv.* **2016**, *6,* 2337-2344.

241. Lingott, J.; Lindner, U.; Telgmann, L.; Esteban-Fernández, D.; Jakubowski, N.; Panne, U., Gadolinium-Uptake by Aquatic and Terrestrial Organisms-Distribution Determined by Laser Ablation Inductively Coupled Plasma Mass Spectrometry. *Environmental Science: Processes & Impacts* **2015**, *18,* 200-207.

242. Saatz, J.; Stryhanyuk, H.; Vetterlein, D.; Musat, N.; Otto, M.; Reemtsma, T.; Richnow, H. H.; Daus, B., Location and Speciation of Gadolinium and Yttrium in Roots of Zea Mays by LA-ICP-MS and Tof-Sims. *Environ. Pollut.* **2016**, *216,* 245-252.

243. Basnet, P.; Amarasiriwardena, D.; Wu, F.; Fu, Z.; Zhang, T., Investigation of Tissue Level Distribution of Functional Groups and Associated Trace Metals in Rice Seeds (Oryza Sativa L.) Using Ftir and LA-ICP-MS. *Microchem. J.* **2016**, *127,* 152-159.

132

244. Thyssen, G. M.; Holtkamp, M.; Kaulfurst-Soboll, H.; Wehe, C. A.; Sperling, M.; von Schaewen, A.; Karst, U., Elemental Bioimaging by Means of La-Icp-Oes: Investigation of the Calcium, Sodium and Potassium Distribution in Tobacco Plant Stems and Leaf Petioles. *Metallomics* **2017**, *9,* 676-684.

245. Pessôa, G. d. S.; Júnior, C. A. L.; Madrid, K. C.; Arruda, M. A. Z., A Quantitative Approach for Cd, Cu, Fe and Mn through Laser Ablation Imaging for Evaluating the Translocation and Accumulation of Metals in Sunflower Seeds. *Talanta* **2017**, *167,* 317-324.

246. Ko, J. A.; Furuta, N.; Lim, H. B., Quantitative Mapping of Elements in Basil Leaves (Ocimum Basilicum) Based on Cesium Concentration and Growth Period Using Laser Ablation ICP-MS. *Chemosphere* **2018**, *190,* 368-374.

247. Li, M. Y.; Wang, P.; Wang, J. Y.; Chen, X. Q.; Zhao, D.; Yin, D. X.; Luo, J.; Juhasz, A. L.; Li, H. B.; Ma, L. Q., Arsenic Concentrations, Speciation, and Localization in 141 Cultivated Market Mushrooms: Implications for Arsenic Exposure to Humans. *Environ Sci Technol* **2019**, *53,* 503-511.

248. Moustakas, M.; Hanc, A.; Dobrikova, A.; Sperdouli, I.; Adamakis, I. S.; Apostolova, E., Spatial Heterogeneity of Cadmium Effects on Salvia Sclarea Leaves Revealed by Chlorophyll Fluorescence Imaging Analysis and Laser Ablation Inductively Coupled Plasma Mass Spectrometry. *Materials (Basel)* **2019**, *12,* 2953.

249. Yamaji, N.; Ma, J. F., Bioimaging of Multiple Elements by High-Resolution LA-ICP-MS Reveals Altered Distribution of Mineral Elements in the Nodes of Rice Mutants. *Plant J.* **2019**, *99,* 1254-1263.

250. Gaiss, S.; Amarasiriwardena, D.; Alexander, D.; Wu, F., Tissue Level Distribution of Toxic and Essential Elements During the Germination Stage of Corn Seeds (Zea Mays, L.) Using LA-ICP-MS. *Environ. Pollut.* **2019**, *252,* 657-665.

251. Shelden, M. C.; Gilbert, S. E.; Tyerman, S. D., A Laser Ablation Technique Maps Differences in Elemental Composition in Roots of Two Barley Cultivars Subjected to Salinity Stress. *Plant J.* **2020**, *101,* 1462-1473.

252. Chithrani, B. D.; Ghazani, A. A.; Chan, W. C. W., Determining the Size and Shape Dependence of Gold Nanoparticle Uptake into Mammalian Cells. *Nano Lett.* **2006**, *6,* 662-668.

253. Du, Z.; Gupta, A.; Clarke, C.; Cappadona, M.; Clases, D.; Liu, D.; Yang, Z.; Karan, S.; Price, W. S.; Xu, X., Porous Upconversion Nanostructures as Bimodal Biomedical Imaging Contrast Agents. *The Journal of Physical Chemistry C* **2020**, *124,* 12168-12174.

254. Gilbert, B.; Fakra, S. C.; Xia, T.; Pokhrel, S.; Madler, L.; Nel, A. E., The Fate of Zno Nanoparticles Administered to Human Bronchial Epithelial Cells. *ACS Nano* **2012**, *6,* 4921-4930.

255. Nativo, P.; Prior, I. A.; Brust, M., Uptake and Intracellular Fate of Surface-Modified Gold Nanoparticles. *ACS Nano* **2008**, *2,* 1639-1644.

256. Wang, M.; Zheng, L. N.; Wang, B.; Chen, H. Q.; Zhao, Y. L.; Chai, Z. F.; Reid, H. J.; Sharp, B. L.; Feng, W. Y., Quantitative Analysis of Gold Nanoparticles in Single Cells by Laser Ablation Inductively Coupled Plasma-Mass Spectrometry. *Anal. Chem.* **2014**, *86,* 10252-10256.

257. Reifschneider, O.; Vennemann, A.; Buzanich, G.; Radtke, M.; Reinholz, U.; Riesemeier, H.; Hogeback, J.; Koppen, C.; Grossgarten, M.; Sperling, M.; Wiemann, M.; Karst, U., Revealing Silver Nanoparticle Uptake by Macrophages Using Sr-Muxrf and LA-ICP-MS. *Chem. Res. Toxicol.* **2020**, *33,* 1250-1255.

258. Scharlach, C.; Müller, L.; Wagner, S.; Kobayashi, Y.; Kratz, H.; Ebert, M.; Jakubowski, N.; Schellenberger, E., LA-ICP-MS Allows Quantitative Microscopy of Europium-Doped Iron Oxide Nanoparticles and Is a Possible Alternative to Ambiguous Prussian Blue Iron Staining. *J. Biomed. Nanotechnol.* **2016**, *12,* 1001-1010.

259. Zarco-Fernandez, S.; Coto-Garcia, A. M.; Munoz-Olivas, R.; Sanz-Landaluze, J.; Rainieri, S.; Camara, C., Bioconcentration of Ionic Cadmium and Cadmium Selenide Quantum Dots in Zebrafish Larvae. *Chemosphere* **2016**, *148,* 328-335.

260. Drescher, D.; Giesen, C.; Traub, H.; Panne, U.; Kneipp, J.; Jakubowski, N., Quantitative Imaging of Gold and Silver Nanoparticles in Single Eukaryotic Cells by Laser Ablation ICP-MS. *Anal. Chem.* **2012**, *84,* 9684-9688.

261. Drescher, D.; Zeise, I.; Traub, H.; Guttmann, P.; Seifert, S.; Büchner, T.; Jakubowski, N.; Schneider, G.; Kneipp, J., In Situ Characterization of Sio2nanoparticle Biointeractions Using Brightsilica. *Adv. Funct. Mater.* **2014**, *24,* 3765-3775.

262. Bishop, D. P.; Grossgarten, M.; Dietrich, D.; Vennemann, A.; Cole, N.; Sperling, M.; Wiemann, M.; Doble, P. A.; Karst, U., Quantitative Imaging of Translocated Silver Following Nanoparticle Exposure by Laser Ablation-Inductively Coupled Plasma-Mass Spectrometry. *Anal. Methods* **2018**, *10,* 836-840.

263. Böhme, S.; Stärk, H.-J.; Reemtsma, T.; Kühnel, D., Effect Propagation after Silver Nanoparticle Exposure in Zebrafish (Danio Rerio) Embryos: A Correlation to Internal Concentration and Distribution Patterns. *Environmental Science: Nano* **2015**, *2,* 603-614.

264. Wang, J.; Nie, Y.; Dai, H.; Wang, M.; Cheng, L.; Yang, Z.; Chen, S.; Zhao, G.; Wu, L.; Guang, S.; Xu, A., Parental Exposure to TiO_2 NPs Promotes the Multigenerational Reproductive Toxicity of Cd in Caenorhabditis Elegans Via Bioaccumulation of Cd in Germ Cells. *Environmental Science: Nano* **2019**, *6,* 1332-1342.

265. El Hadri, H.; Gigault, J.; Mounicou, S.; Grassl, B.; Reynaud, S., Trace Element Distribution in Marine Microplastics Using Laser Ablation-ICP-MS. *Mar. Pollut. Bull.* **2020**, *160,* 111716.

266. Koelmel, J.; Leland, T.; Wang, H.; Amarasiriwardena, D.; Xing, B., Investigation of Gold Nanoparticles Uptake and Their Tissue Level Distribution in Rice Plants by Laser Ablation-Inductively Coupled-Mass Spectrometry. *Environ. Pollut.* **2013**, *174,* 222-228.

267. Neves, V. M.; Heidrich, G. M.; Rodrigues, E. S.; Enders, M. S. P.; Muller, E. I.; Nicoloso, F. T.; Carvalho, H. W. P.; Dressler, V. L., La_2O_3 Nanoparticles: Study of Uptake and Distribution in Pfaffia Glomerata (Spreng.) Pedersen by LA-ICP-MS and Mu-Xrf. *Environ Sci Technol* **2019**, *53,* 10827-10834.

268. Ko, J. A.; Furuta, N.; Lim, H. B., New Approach for Mapping and Physiological Test of Silica Nanoparticles Accumulated in Sweet Basil (Ocimum Basilicum) by LA-ICP-MS. *Anal. Chim. Acta* **2019**, *1069,* 28-35.

269. Wojcieszek, J.; Jimenez-Lamana, J.; Bierla, K.; Ruzik, L.; Asztemborska, M.; Jarosz, M.; Szpunar, J., Uptake, Translocation, Size Characterization and Localization of Cerium Oxide Nanoparticles in Radish (Raphanus Sativus L.). *Sci. Total Environ.* **2019**, *683,* 284-292.

270. Yamashita, S.; Yoshikuni, Y.; Obayashi, H.; Suzuki, T.; Green, D.; Hirata, T., Simultaneous Determination of Size and Position of Silver and Gold Nanoparticles in Onion Cells Using Laser Ablation-ICP-MS. *Anal. Chem.* **2019**, *91,* 4544-4551.

271. Kroger, S.; Sperling, M.; Karst, U., Quantitative Dried Blood Spot Analysis for Metallodrugs by Laser Ablation-Inductively Coupled Plasma-Mass Spectrometry. *J. Trace Elem. Med. Biol.* **2019**, *51,* 50-56.

272. Kumtabtim, U.; Siripinyanond, A.; Auray-Blais, C.; Ntwari, A.; Becker, J. S., Analysis of Trace Metals in Single Droplet of Urine by Laser Ablation Inductively Coupled Plasma Mass Spectrometry. *Int. J. Mass Spectrom.* **2011**, *307,* 174-181.

273. Clases, D.; Sperling, M.; Karst, U., Analysis of Metal-Based Contrast Agents in Medicine and the Environment. *Trends Analyt. Chem.* **2018**, *104,* 135-147.

274. Clases, D.; Fingerhut, S.; Jeibmann, A.; Sperling, M.; Doble, P.; Karst, U., LA-ICP-MS/MS Improves Limits of Detection in Elemental Bioimaging of Gadolinium Deposition Originating from Mri Contrast Agents in Skin and Brain Tissues. *J. Trace Elem. Med. Biol.* **2019**, *51,* 212-218.

275. Richter, H.; Bucker, P.; Dunker, C.; Karst, U.; Kircher, P. R., Gadolinium Deposition in the Brain of Dogs after Multiple Intravenous Administrations of Linear Gadolinium Based Contrast Agents. *PLoS One* **2020**, *15,* e0227649.

276. Moreno-Gordaliza, E.; Giesen, C.; Lázaro, A.; Esteban-Fernández, D.; Humanes, B.; Cañas, B.; Panne, U.; Tejedor, A.; Jakubowski, N.; Gómez-Gómez, M. M., Elemental Bioimaging in Kidney by LA–ICP–MS as a Tool to Study Nephrotoxicity and Renal Protective Strategies in Cisplatin Therapies. *Anal. Chem.* **2011**, *83,* 7933-7940.

277. Egger, A. E.; Theiner, S.; Kornauth, C.; Heffeter, P.; Berger, W.; Keppler, B. K.; Hartinger, C. G., Quantitative Bioimaging by LA-ICP-MS: A Methodological Study on the Distribution of Pt and Ru in Viscera Originating from Cisplatin- and Kp1339-Treated Mice. *Metallomics* **2014**, *6,* 1616-25.

278. Bent, S. A. S. v. d.; Berg, T.; Karst, U.; Sperling, M.; Rustemeyer, T., Allergic Reaction to a Green Tattoo with Nickel as a Possible Allergen. *Contact Dermatitis* **2019**, *81,* 64-66.

279. Sela, H.; Karpas, Z.; Zoriy, M.; Pickhardt, C.; Becker, J. S., Biomonitoring of Hair Samples by Laser Ablation Inductively Coupled Plasma Mass Spectrometry (LA-ICP-MS). *Int. J. Mass Spectrom.* **2007**, *261,* 199-207.

280. Hasegawa, M.; Duncan, B. R.; Marshall, D. A.; Gonzalez-Cuyar, L. F.; Paulsen, M.; Kobayashi, M.; Simpson, C.; Maravilla, K. R., Human Hair as a Possible Surrogate Marker of Retained Tissue Gadolinium: A Pilot Autopsy Study Correlating Gadolinium Concentrations in Hair with Brain and Other Tissues among Decedents Who Received Gadolinium-Based Contrast Agents. *Investigative Radiology* **2020**, *55,* 636-642.

281. Luo, R.; Su, X.; Xu, W.; Zhang, S.; Zhuo, X.; Ma, D., Determination of Arsenic and Lead in Single Hair Strands by Laser Ablation Inductively Coupled Plasma Mass Spectrometry. *Sci. Rep.* **2017**, *7,* 3426.

282. Pozebon, D.; Dressler, V. L.; Matusch, A.; Becker, J. S., Monitoring of Platinum in a Single Hair by Laser Ablation Inductively Coupled Plasma Mass Spectrometry (LA-ICP-MS) after Cisplatin Treatment for Cancer. *Int. J. Mass Spectrom.* **2008**, *272,* 57-62.

283. Stadlbauer, C.; Prohaska, T.; Reiter, C.; Knaus, A.; Stingeder, G., Time-Resolved Monitoring of Heavy-Metal Intoxication in Single Hair by Laser Ablation Icp-Drcms. *Anal. Bioanal. Chem.* **2005**, *383,* 500-508.

284. Abad, S. Q.; Rodríguez-González, P.; Alonso, J. I. G., Evidence of the Direct Adsorption of Mercury in Human Hair During Occupational Exposure to Mercury Vapour. *J. Trace Elem. Med. Biol.* **2016**, *36,* 16-21.

285. Noël, M.; Christensen, J. R.; Spence, J.; Robbins, C. T., Using Laser Ablation Inductively Coupled Plasma Mass Spectrometry (LA-ICP-MS) to Characterize Copper, Zinc and Mercury Along Grizzly Bear Hair Providing Estimate of Diet. *Sci. Total Environ.* **2015**, *529,* 1-9.

286. Ek, K. H.; Morrison, G. M.; Lindberg, P.; Rauch, S., Comparative Tissue Distribution of Metals in Birds in Sweden Using ICP-MS and Laser Ablation ICP-MS. *Arch. Environ. Contam. Toxicol.* **2004**, *47*, 259-269.

287. Chavatte, L.; Juan, M.; Mounicou, S.; Leblanc Noblesse, E.; Pays, K.; Nizard, C.; Bulteau, A. L., Elemental and Molecular Imaging of Human Full Thickness Skin after Exposure to Heavy Metals. *Metallomics* **2020**, *12,* 1555-1562.

288. Rodushkin, I.; Axelsson, M. D., Application of Double Focusing Sector Field ICP-MS for Multielemental Characterization of Human Hair and Nails. Part iii. Direct Analysis by Laser Ablation. *Sci. Total Environ.* **2003**, *305,* 23-39.

289. Hann, S.; Latkoczy, C.; Bereuter, T. L.; Prohaska, T.; Stingeder, G.; Reiter, C., Reconstruction of a Case of Thallium Poisoning Using LA-ICP-SFMS. *International Journal of Legal Medicine* **2005**, *119,* 35-39.

290. Caumette, G.; Ouypornkochagorn, S.; Scrimgeour, C. M.; Raab, A.; Feldmann, J., Monitoring the Arsenic and Iodine Exposure of Seaweed-Eating North Ronaldsay Sheep from the Gestational and Suckling Periods to Adulthood by Using Horns as a Dietary Archive. *Environ. Sci. Technol.* **2007**, *41,* 2673-2679.

291. Evans, R. D.; Richner, P.; Outridge, P. M., Micro-Spatial Variations of Heavy Metals in the Teeth of Walrus as Determined by Laser Ablation ICP-MS: The Potential for Reconstructing a History of Metal Exposure. *Arch. Environ. Contam. Toxicol.* **1995**, *28,* 55-60.

292. Shepherd, T. J.; Dirks, W.; Manmee, C.; Hodgson, S.; Banks, D. A.; Averley, P.; Pless-Mulloli, T., Reconstructing the Life-Time Lead Exposure in Children Using Dentine in Deciduous Teeth. *Sci. Total Environ.* **2012**, *425,* 214-222.

293. Austin, C.; Niedzwiecki, M. M.; Arora, M., Multielemental Bioimaging of Tissues in Children's Environmental Health Research. *Curr. Opin. Pediatr.* **2016**, *28,* 216-220.

294. Arora, M.; Bradman, A.; Austin, C.; Vedar, M.; Holland, N.; Eskenazi, B.; Smith, D. R., Determining Fetal Manganese Exposure from Mantle Dentine of Deciduous Teeth. *Environ Sci Technol* **2012**, *46,* 5118-5125.

295. Savabieasfahani, M.; Ali, S. S.; Bacho, R.; Savabi, O.; Alsabbak, M., Prenatal Metal Exposure in the Middle East: Imprint of War in Deciduous Teeth of Children. *Environ. Monit. Assess.* **2016**, *188,* 505.

296. Palace, V. P.; Halden, N. M.; Yang, P.; Evans, R. E.; Sterling, G., Determining Residence Patterns of Rainbow Trout Using Laser Ablation Inductively Coupled Plasma Mass Spectrometry (LA-ICP-MS) Analysis of Selenium in Otoliths. *Environ. Sci. Technol.* **2007**, *41,* 3679-3683.

297. Mounicou, S.; Frelon, S.; Guernic, A. L.; Eb-Levadoux, Y.; Camilleri, V.; Fevrier, L.; Pierrisnard, S.; Carasco, L.; Gilbin, R.; Mahé, K.; Tabouret, H.; Bareille, G.; Simon, O., Use of Fish Otoliths as a Temporal Biomarker of Field Uranium Exposure. *Sci. Total Environ.* **2019**, *690,* 511-521.

298. Ishii, C.; Nakayama, S. M. M.; Kataba, A.; Ikenaka, Y.; Saito, K.; Watanabe, Y.; Makino, Y.; Matsukawa, T.; Kubota, A.; Yokoyama, K.; Mizukawa, H.; Hirata, T.; Ishizuka, M., Characterization and Imaging of Lead Distribution in Bones of Lead-Exposed Birds by ICP-MS and LA-ICP-MS. *Chemosphere* **2018**, *212,* 994-1001.

136

299. Jackson, B. P.; Hopkins, W. A.; Baionno, J., Laser Ablation-ICP-MS Analysis of Dissected Tissue: A Conservation-Minded Approach to Assessing Contaminant Exposure. *Environ. Sci. Technol.* **2003**, *37,* 2511-2515.

300. Kowal-Linka, M.; Jochum, K. P.; Surmik, D., LA-ICP-MS Analysis of Rare Earth Elements in Marine Reptile Bones from the Middle Triassic Bonebed (Upper Silesia, S Poland): Impact of Long-Lasting Diagenesis, and Factors Controlling the Uptake. *Chem. Geol.* **2014**, *363,* 213-228.

301. Galiová, M.; Kaiser, J.; Fortes, F. J.; Novotný, K.; Malina, R.; Prokeš, L.; Hrdlička, A.; Vaculovič, T.; Nývltová Fišáková, M.; Svoboda, J.; Kanický, V.; Laserna, J. J., Multielemental Analysis of Prehistoric Animal Teeth by Laser-Induced Breakdown Spectroscopy and Laser Ablation Inductively Coupled Plasma Mass Spectrometry. *Appl. Opt.* **2010**, *49,* C191-C199.

302. Roberts, J.; Weeks, L.; Fillios, M.; Cable, C.; al-Ali, Y. Y.; Boraik, M.; Zein, H., Preliminary Insights into Late Prehistoric Fish Procurement Strategies in the Desert Interior of Southeastern Arabia: The Results of LA-ICP-MS Analysis of a Fish Otolith Assemblage from Saruq Al-Hadid, Uae. *Journal of Archaeological Science: Reports* **2019**, *26,* 101856.

303. Austin, C.; Smith, T. M.; Bradman, A.; Hinde, K.; Joannes-Boyau, R.; Bishop, D.; Hare, D. J.; Doble, P.; Eskenazi, B.; Arora, M., Barium Distributions in Teeth Reveal Early-Life Dietary Transitions in Primates. *Nature* **2013**, *498,* 216-219.

304. Byrne, S.; Amarasiriwardena, D.; Bandak, B.; Bartkus, L.; Kane, J.; Jones, J.; Yañez, J.; Arriaza, B.; Cornejo, L., Were Chinchorros Exposed to Arsenic? Arsenic Determination in Chinchorro Mummies' Hair by Laser Ablation Inductively Coupled Plasma-Mass Spectrometry (LA-ICP-MS). *Microchem. J.* **2010**, *94,* 28-35.

305. Bartkus, L.; Amarasiriwardena, D.; Arriaza, B.; Bellis, D.; Yañez, J., Exploring Lead Exposure in Ancient Chilean Mummies Using a Single Strand of Hair by Laser Ablation-Inductively Coupled Plasma-Mass Spectrometry (LA-ICP-MS). *Microchem. J.* **2011**, *98,* 267-274.

306. Blumenstiel, D.; McDonald, M.; Arriaza, B.; Amarasiriwardena, D., Exposure to Geogenic Lithium in Ancient Andeans: Unraveling Lithium in Mummy Hair Using LA-ICP-MS. *J. Archaeol. Sci.* **2020**, *113,* 105062.

307. Steely, S.; Amarasiriwardena, D.; Jones, J.; Yañez, J., A Rapid Approach for Assessment of Arsenic Exposure by Elemental Analysis of Single Strand of Hair Using Laser Ablation-Inductively Coupled Plasma-Mass Spectrometry. *Microchem. J.* **2007**, *86,* 235-240.

308. Guede, I.; Zuluaga, M. C.; Ortega, L. A.; Alonso-Olazabal, A.; Murelaga, X.; Pina, M.; Gutierrez, F. J., Analyses of Human Dentine and Tooth Enamel by Laser Ablation-Inductively Coupled Plasma-Mass Spectrometry (LA-ICP-MS) to Study the Diet of Medieval Muslim Individuals from Tauste (Spain). *Microchem. J.* **2017**, *130,* 287-294.

309. Farell, J.; Amarasiriwardena, D.; Goodman, A. H.; Arriaza, B., Bioimaging of Trace Metals in Ancient Chilean Mummies and Contemporary Egyptian Teeth by Laser Ablation-Inductively Coupled Plasma-Mass Spectrometry (LA-ICP-MS). *Microchem. J.* **2013**, *106,* 340-346.

310. López-Costas, O.; Kylander, M.; Mattielli, N.; Álvarez-Fernández, N.; Pérez-Rodríguez, M.; Mighall, T.; Bindler, R.; Cortizas, A. M., Human Bones Tell the Story of Atmospheric Mercury and Lead Exposure at the Edge of Roman World. *Sci. Total Environ.* **2019**, *710,* 136319.

311. Maurer, A.-F.; Barrulas, P.; Person, A.; Mirão, J.; Barrocas Dias, C.; Boudouma, O.; Segalen, L., Testing LA-ICP-MS Analysis of Archaeological Bones with Different Diagenetic Histories for Paleodiet Prospect. *Palaeogeography, Palaeoclimatology, Palaeoecology* **2019**, *534,* 109287.

312. Castro, W.; Hoogewerff, J.; Latkoczy, C.; Almirall, J. R., Application of Laser Ablation (LA-ICP-SF-MS) for the Elemental Analysis of Bone and Teeth Samples for Discrimination Purposes. *Forensic Sci. Int.* **2010**, *195,* 17-27.

313. Stadlbauer, C.; Reiter, C.; Patzak, B.; Stingeder, G.; Prohaska, T., History of Individuals of the 18th/19th Centuries Stored in Bones, Teeth, and Hair Analyzed by LA-ICP-MS-A Step in Attempts to Confirm the Authenticity of Mozart's Skull. *Anal. Bioanal. Chem.* **2007**, *388,* 593-602.

314. Almirall, J. R.; Trejos, T., Applications of LA-ICP-MS to Forensic Science. *Elements* **2016**, *12,* 335-340.

315. McAllum, E. J.; Hare, D. J., From Niche Methods to Necessary Tools: The Growing Importance of Analytical Atomic Spectrometry in Metal Imaging in Neuroscience. *Spectrochim. Acta Part B At. Spectrosc.* **2019**, *156,* 20-32.

316. Wolf, C.; Schaumlöffel, D.; Richarz, A.-N.; Prange, A.; Brätter, P., Cze-ICP-MS Separation of Metallothioneins in Human Brain Cytosols: Comparability of Electropherograms Obtained from Different Sample Matrices. *Analyst* **2003**, *128,* 576-580.

317. Gellein, K.; Garruto, R. M.; Syversen, T.; Sjobakk, T. E.; Flaten, T. P., Concentrations of Cd, Co, Cu, Fe, Mn, Rb, V, and Zn in Formalin-Fixed Brain Tissue in Amyotrophic Lateral Sclerosis and Parkinsonism-Dementia Complex of Guam Determined by High-Resolution ICP-MS. *Biol. Trace Elem. Res.* **2003**, *96,* 39-60.

318. Hare, D. J.; George, J. L.; Bray, L.; Volitakis, I.; Vais, A.; Ryan, T. M.; Cherny, R. A.; Bush, A. I.; Masters, C. L.; Adlard, P. A.; Doble, P. A.; Finkelstein, D. I., The Effect of Paraformaldehyde Fixation and Sucrose Cryoprotection on Metal Concentration in Murine Neurological Tissue. *J. Anal. At. Spectrom.* **2014**, *29,* 565-570.

319. Hare, D. J.; Gerlach, M.; Riederer, P., Considerations for Measuring Iron in Post-Mortem Tissue of Parkinson's Disease Patients. *J Neural Transm (Vienna)* **2012**, *119,* 1515-1521.

320. Bonta, M.; Török, S.; Hegedus, B.; Döme, B.; Limbeck, A., A Comparison of Sample Preparation Strategies for Biological Tissues and Subsequent Trace Element Analysis Using LA-ICP-MS. *Anal. Bioanal. Chem.* **2017**, *409,* 1805-1814.

321. Pushie, M. J.; Hollings, A.; Reinhardt, J.; Webb, S. M.; Lam, V.; Takechi, R.; Mamo, J. C.; Paterson, P. G.; Kelly, M. E.; George, G. N.; Pickering, I. J.; Hackett, M. J., Sample Preparation with Sucrose Cryoprotection Dramatically Alters Zn Distribution in the Rodent Hippocampus, as Revealed by Elemental Mapping. *J. Anal. At. Spectrom.* **2020**, *35,* 2498-2508.

322. Ponomarenko, E. A.; Poverennaya, E. V.; Ilgisonis, E. V.; Pyatnitskiy, M. A.; Kopylov, A. T.; Zgoda, V. G.; Lisitsa, A. V.; Archakov, A. I., The Size of the Human Proteome: The Width and Depth. *Int. J. Anal. Chem.* **2016**, 7436849.

323. Becker, J. S.; Zoriy, M.; Becker, J. S.; Pickhardt, C.; Przybylski, M., Determination of Phosphorus and Metals in Human Brain Proteins after Isolation by Gel Electrophoresis by Laser Ablation Inductively Coupled Plasma Source Mass Spectrometry. *J. Anal. At. Spectrom.* **2004**, *19,* 149-152.

324. Becker, J. S.; Zoriy, M.; Pickhardt, C.; Przybylski, M.; Becker, J. S., Investigation of Cu-, Zn- and Fe-Containing Human Brain Proteins Using Isotopic-Enriched Tracers by LA-ICP-MS and Maldi-Ft-Icr-Ms. *Int. J. Mass Spectrom.* **2005**, *242,* 135-144.

325. Zoriy, M. V.; Becker, J. S., Imaging of Elements in Thin Cross Sections of Human Brain Samples by LA-ICP-MS: A Study on Reproducibility. *Int. J. Mass Spectrom.* **2007**, *264,* 175-180.

326. Lhermitte, J.; Kraus, W. M.; McAlpine, D., Original Papers: On the Occurrence of Abnormal Deposits of Iron in the Brain in Parkinsonism with Special Reference to Its Localisation. *J Neurol Psychopathol* **1924**, *5,* 195-208.

327. Hare, D. J.; Lei, P.; Ayton, S.; Roberts, B. R.; Grimm, R.; George, J. L.; Bishop, D. P.; Beavis, A. D.; Donovan, S. J.; McColl, G.; Volitakis, I.; Masters, C. L.; Adlard, P. A.; Cherny, R. A.; Bush, A. I.; Finkelstein, D. I.; Doble, P. A., An Iron–Dopamine Index Predicts Risk of Parkinsonian Neurodegeneration in the Substantia Nigra Pars Compacta. *Chem. Sci.* **2014**, *5,* 2160-2169.

328. Hare, D. J.; Double, K. L., Iron and Dopamine: A Toxic Couple. *Brain* **2016**, *139,* 1026-1035.

329. Dexter, D. T.; Wells, F. R.; Agid, F.; Agid, Y.; Lees, A. J.; Jenner, P.; Marsden, C. D., Increased Nigral Iron Content in Postmortem Parkinsonian Brain. *Lancet* **1987**, *2,* 1219-1220.

330. Dexter, D. T.; Wells, F. R.; Lees, A. J.; Agid, F.; Agid, Y.; Jenner, P.; Marsden, C. D., Increased Nigral Iron Content and Alterations in Other Metal Ions Occurring in Brain in Parkinson's Disease. *J Neurochem* **1989**, *52,* 1830-1836.

331. Hare, D.; Reedy, B.; Grimm, R.; Wilkins, S.; Volitakis, I.; George, J. L.; Cherny, R. A.; Bush, A. I.; Finkelstein, D. I.; Doble, P., Quantitative Elemental Bio-Imaging of Mn, Fe, Cu and Zn in 6-Hydroxydopamine Induced Parkinsonism Mouse Models. *Metallomics* **2009**, *1,* 53-58.

332. Matusch, A.; Fenn, L. S.; Depboylu, C.; Klietz, M.; Strohmer, S.; McLean, J. A.; Becker, S. J., Combined Elemental and Biomolecular Mass Spectrometry Imaging for Probing the Inventory of Tissue at a Micrometer Scale. *Anal. Chem.* **2012**, *84,* 3170-3178.

333. Matusch, A.; Depboylu, C.; Palm, C.; Wu, B.; Höglinger, G. U.; Schäfer, M. K.; Becker, S. J., Cerebral Bioimaging of Cu, Fe, Zn, and Mn in the Mptp Mouse Model of Parkinson's Disease Using Laser Ablation Inductively Coupled Plasma Mass Spectrometry (LA-ICP-MS). *J. Am. Soc. Mass Spectrom.* **2010**, *21,* 161-171.

334. Hare, D. J.; Adlard, P. A.; Doble, P. A.; Finkelstein, D. I., Metallobiology of 1-Methyl-4-Phenyl-1,2,3,6-Tetrahydropyridine Neurotoxicity. *Metallomics* **2013**, *5,* 91-109.

335. Wang, J. Y.; Zhuang, Q. Q.; Zhu, L. B.; Zhu, H.; Li, T.; Li, R.; Chen, S. F.; Huang, C. P.; Zhang, X.; Zhu, J. H., Meta-Analysis of Brain Iron Levels of Parkinson's Disease Patients Determined by Postmortem and Mri Measurements. *Sci. Rep.* **2016**, *6,* 36669.

336. Genoud, S.; Senior, A. M.; Hare, D. J.; Double, K. L., Meta-Analysis of Copper and Iron in Parkinson's Disease Brain and Biofluids. *Mov. Disord.* **2020**, *35,* 662-671.

337. Trist, B. G.; Hilton, J. B.; Hare, D. J.; Crouch, P. J.; Double, K. L., Superoxide Dismutase 1 in Health and Disease: How a Frontline Antioxidant Becomes Neurotoxic. *Angew. Chem. Int. Ed. Engl.* **2020**, *60,* 9215-9246.

338. Monzani, E.; Nicolis, S.; Dell'Acqua, S.; Capucciati, A.; Bacchella, C.; Zucca, F. A.; Mosharov, E. V.; Sulzer, D.; Zecca, L.; Casella, L., Dopamine, Oxidative Stress and Protein-Quinone Modifications in Parkinson's and Other Neurodegenerative Diseases. *Angew. Chem. Int. Ed. Engl.* **2019**, *58,* 6512-6527.

339. Sun, Y.; Pham, A. N.; Hider, R. C.; Zheng, H.; Waite, T. D., Effectiveness of the Iron Chelator Cn128 in Mitigating the Formation of Dopamine Oxidation Products Associated with the Progression of Parkinson's Disease. *ACS Chem. Neurosci.* **2020**, *11,* 3646-3657.

340. Kordower, J. H.; Olanow, C. W.; Dodiya, H. B.; Chu, Y.; Beach, T. G.; Adler, C. H.; Halliday, G. M.; Bartus, R. T., Disease Duration and the Integrity of the Nigrostriatal System in Parkinson's Disease. *Brain* **2013**, *136,* 2419-2431.

341. Neumann, B.; Hosl, S.; Schwab, K.; Theuring, F.; Jakubowski, N., Multiplex LA-ICP-MS Bio-Imaging of Brain Tissue of a Parkinsonian Mouse Model Stained with Metal-Coded Affinity-Tagged Antibodies and Coated with Indium-Spiked Commercial Inks as Internal Standards. *J. Neurosci. Methods* **2020**, *334,* 108591.

342. Olmedo-Diaz, S.; Estevez-Silva, H.; Oradd, G.; Af Bjerken, S.; Marcellino, D.; Virel, A., An Altered Blood-Brain Barrier Contributes to Brain Iron Accumulation and Neuroinflammation in the 6-OHDA Rat Model of Parkinson's Disease. *Neuroscience* **2017**, *362,* 141-151.

343. Billings, J. L.; Gordon, S. L.; Rawling, T.; Doble, P. A.; Bush, A. I.; Adlard, P. A.; Finkelstein, D. I.; Hare, D. J., L-3,4-Dihydroxyphenylalanine (L-Dopa) Modulates Brain Iron, Dopaminergic Neurodegeneration and Motor Dysfunction in Iron Overload and Mutant Alpha-Synuclein Mouse Models of Parkinson's Disease. *J. Neurochem* **2019**, *150,* 88-106.

344. Finkelstein, D. I.; Billings, J. L.; Adlard, P. A.; Ayton, S.; Sedjahtera, A.; Masters, C. L.; Wilkins, S.; Shackleford, D. M.; Charman, S. A.; Bal, W.; Zawisza, I. A.; Kurowska, E.; Gundlach, A. L.; Ma, S.; Bush, A. I.; Hare, D. J.; Doble, P. A.; Crawford, S.; Gautier, E. C.; Parsons, J.; Huggins, P.; Barnham, K. J.; Cherny, R. A., The Novel Compound PBT434 Prevents Iron Mediated Neurodegeneration and Alpha-Synuclein Toxicity in Multiple Models of Parkinson's Disease. *Acta Neuropathol. Commun.* **2017**, *5,* 53.

345. Burbulla, L. F.; Song, P.; Mazzulli, J. R.; Zampese, E.; Wong, Y. C.; Jeon, S.; Santos, D. P.; Blanz, J.; Obermaier, C. D.; Strojny, C.; Savas, J. N.; Kiskinis, E.; Zhuang, X.; Kruger, R.; Surmeier, D. J.; Krainc, D., Dopamine Oxidation Mediates Mitochondrial and Lysosomal Dysfunction in Parkinson's Disease. *Science* **2017**, *357,* 1255-1261.

346. Kawahara, M.; Kato-Negishi, M., Link between Aluminum and the Pathogenesis of Alzheimer's Disease: The Integration of the Aluminum and Amyloid Cascade Hypotheses. *International Journal of Alzheimer's Disease* **2011**, *2011,* 276393.

347. Cuajungco, M. P.; Goldstein, L. E.; Nunomura, A.; Smith, M. A.; Lim, J. T.; Atwood, C. S.; Huang, X.; Farrag, Y. W.; Perry, G.; Bush, A. I., Evidence That the B-Amyloid Plaques of Alzheimer's Disease Represent the Redox-Silencing and Entombment of Aβ by Zinc. *J. Biol. Chem.* **2000**, *275,* 19439-19442.

348. Stockwell, B. R.; Friedmann Angeli, J. P.; Bayir, H.; Bush, A. I.; Conrad, M.; Dixon, S. J.; Fulda, S.; Gascon, S.; Hatzios, S. K.; Kagan, V. E.; Noel, K.; Jiang, X.; Linkermann, A.; Murphy, M. E.; Overholtzer, M.; Oyagi, A.; Pagnussat, G. C.; Park, J.; Ran, Q.; Rosenfeld, C. S.; Salnikow, K.; Tang, D.; Torti, F. M.; Torti, S. V.; Toyokuni, S.; Woerpel, K. A.; Zhang, D. D., Ferroptosis: A Regulated Cell Death Nexus Linking Metabolism, Redox Biology, and Disease. *Cell* **2017**, *171,* 273-285.

349. Rembach, A.; Hare, D. J.; Doecke, J. D.; Burnham, S. C.; Volitakis, I.; Fowler, C. J.; Cherny, R. A.; McLean, C.; Grimm, R.; Martins, R.; Ames, D.; Masters, C. L.; Bush, A. I.; Roberts, B. R., Decreased Serum Zinc Is an Effect of Ageing and Not Alzheimer's Disease. *Metallomics* **2014**, *6,* 1216-1219.

350.   Hare, D. J.; Faux, N. G.; Roberts, B. R.; Volitakis, I.; Martins, R. N.; Bush, A. I., Lead and Manganese Levels in Serum and Erythrocytes in Alzheimer's Disease and Mild Cognitive Impairment: Results from the Australian Imaging, Biomarkers and Lifestyle Flagship Study of Ageing. *Metallomics* **2016**, *8,* 628-32.

351.   He, N.; Ling, H.; Ding, B.; Huang, J.; Zhang, Y.; Zhang, Z.; Liu, C.; Chen, K.; Yan, F., Region-Specific Disturbed Iron Distribution in Early Idiopathic Parkinson's Disease Measured by Quantitative Susceptibility Mapping: Magnetic Susceptibility Analysis in Early Pd. *Hum. Brain Mapp.* **2015**, *36,* 4407-4420.

352.   Schrag, M.; Mueller, C.; Oyoyo, U.; Smith, M. A.; Kirsch, W. M., Iron, Zinc and Copper in the Alzheimer's Disease Brain: A Quantitative Meta-Analysis. Some Insight on the Influence of Citation Bias on Scientific Opinion. *Prog. Neurobiol.* **2011**, *94,* 296-306.

353.   Majka, P.; Bai, S.; Bakola, S.; Bednarek, S.; Chan, J. M.; Jermakow, N.; Passarelli, L.; Reser, D. H.; Theodoni, P.; Worthy, K. H.; Wang, X. J.; Wojcik, D. K.; Mitra, P. P.; Rosa, M. G. P., Open Access Resource for Cellular-Resolution Analyses of Corticocortical Connectivity in the Marmoset Monkey. *Nat. Commun.* **2020**, *11,* 1133.

354.   Hare, D. J.; Raven, E. P.; Roberts, B. R.; Bogeski, M.; Portbury, S. D.; McLean, C. A.; Masters, C. L.; Connor, J. R.; Bush, A. I.; Crouch, P. J.; Doble, P. A., Laser Ablation-Inductively Coupled Plasma-Mass Spectrometry Imaging of White and Gray Matter Iron Distribution in Alzheimer's Disease Frontal Cortex. *Neuroimage* **2016**, *137,* 124-131.

355.   Stuber, C.; Morawski, M.; Schafer, A.; Labadie, C.; Wahnert, M.; Leuze, C.; Streicher, M.; Barapatre, N.; Reimann, K.; Geyer, S.; Spemann, D.; Turner, R., Myelin and Iron Concentration in the Human Brain: A Quantitative Study of Mri Contrast. *Neuroimage* **2014**, *93 Pt 1,* 95-106.

356.   Pugh, J. A.; Cox, A. G.; McLeod, C. W.; Bunch, J.; Writer, M. J.; Hart, S. L.; Bienemann, A.; White, E.; Bell, J., Elemental Imaging of Mri Contrast Agents: Benchmarking of LA-ICP-MS to Mri. *Anal. Bioanal. Chem.* **2012**, *403,* 1641-1649.

357.   Niehoff, A.-C.; Wachsmuth, L.; Schmid, F.; Sperling, M.; Faber, C.; Karst, U., Quantification of Manganese Enhanced Magnetic Resonance Imaging Based on Spatially Resolved Elemental Mass Spectrometry. *ChemistrySelect* **2016**, *1,* 264-266.

358.   McAllum, E. J.; Hare, D. J.; Volitakis, I.; McLean, C. A.; Bush, A. I.; Finkelstein, D. I.; Roberts, B. R., Regional Iron Distribution and Soluble Ferroprotein Profiles in the Healthy Human Brain. *Prog. Neurobiol.* **2020**, *186,* 101744.

359.   James, S. A.; Hare, D. J.; Jenkins, N. L.; Jonge, M. D. d.; Bush, A. I.; McColl, G., ΦXanes: In Vivo Imaging of Metal-Protein Coordination Environments. *Sci. Rep.* **2016**, *6,* 20350.

360.   Cheung, C. C.; D'Arrigo, C.; Dietel, M.; Francis, G. D.; Gilks, B. C.; Hall, J. A.; Hornick, J. L.; Ibrahim, M.; Marchetti, A.; Miller, K.; Krieken, H. J. v.; Nielsen, S.; Swanson, P. E.; Taylor, C. R.; Vyberg, M.; Zhou, X.; Torlakovic, E. E.; Path, F. t. f.; and, f., Evolution of Quality Assurance for Clinical Immunohistochemistry in the Era of Precision Medicine. *Applied Immunohistochemistry Molecular Morphology* **2017**, *25,* 4-11.

361.   Bishop, D. P.; Cole, N.; Zhang, T.; Doble, P. A.; Hare, D. J., A Guide to Integrating Immunohistochemistry and Chemical Imaging. *Chem. Soc. Rev.* **2018**, *47,* 3770-3787.

362.   Lores-Padin, A.; Menero-Valdes, P.; Fernandez, B.; Pereiro, R., Nanoparticles as Labels of Specific-Recognition Reactions for the Determination of Biomolecules by Inductively Coupled Plasma-Mass Spectrometry. *Anal. Chim. Acta* **2020**, *1128,* 251-268.

363. Waentig, L.; Jakubowski, N.; Hardt, S.; Scheler, C.; Roos, P. H.; Linscheid, M. W., Comparison of Different Chelates for Lanthanide Labeling of Antibodies and Application in a Western Blot Immunoassay Combined with Detection by Laser Ablation (La-)ICP-MS. *J. Anal. At. Spectrom.* **2012**, *27,* 1311-1320.

364. Lou, X.; Zhang, G.; Herrera, I.; Kinach, R.; Ornatsky, O.; Baranov, V.; Nitz, M.; Winnik, M. A., Polymer-Based Elemental Tags for Sensitive Bioassays. *Angew. Chem. Int. Ed. Engl.* **2007**, *46,* 6111-6114.

365. Hutchinson, R. W.; Cox, A. G.; McLeod, C. W.; Marshall, P. S.; Harper, A.; Dawson, E. L.; Howlett, D. R., Imaging and Spatial Distribution of Beta-Amyloid Peptide and Metal Ions in Alzheimer's Plaques by Laser Ablation-Inductively Coupled Plasma-Mass Spectrometry. *Anal. Biochem.* **2005**, *346,* 225-33.

366. Seuma, J.; Bunch, J.; Cox, A.; McLeod, C.; Bell, J.; Murray, C., Combination of Immunohistochemistry and Laser Ablation Icp Mass Spectrometry for Imaging of Cancer Biomarkers. *Proteomics* **2008**, *8,* 3775-3784.

367. Jakubowski, N.; Messerschmidt, J.; Añorbe, M. G.; Waentig, L.; Hayen, H.; Roos, P. H., Labelling of Proteins by Use of Iodination and Detection by ICP-MS. *J. Anal. At. Spectrom.* **2008**, *23,* 1487-1496.

368. Jakubowski, N.; Waentig, L.; Hayen, H.; Venkatachalam, A.; von Bohlen, A.; Roos, P. H.; Manz, A., Labelling of Proteins with 2-(4-Isothiocyanatobenzyl)-1,4,7,10-Tetraazacyclododecane-1,4,7,10-Tetraacetic Acid and Lanthanides and Detection by ICP-MS. *J. Anal. At. Spectrom.* **2008**, *23,* 1497-1507.

369. Waentig, L.; Roos, P. H.; Jakubowski, N., Labelling of Antibodies and Detection by Laser Ablation Inductively Coupled Plasma Mass Spectrometry : Part Iii. Optimization of Antibody Labelling for Application in a Western Blot Procedure. *J. Anal. At. Spectrom.* **2009**, *24,* 924-933.

370. Waentig, L.; Jakubowski, N.; Hayen, H.; Roos, P. H., Iodination of Proteins, Proteomes and Antibodies with Potassium Triodide for LA-ICP-MS Based Proteomic Analyses. *J. Anal. At. Spectrom.* **2011**, *26,* 1610-1618.

371. Giesen, C.; Waentig, L.; Mairinger, T.; Drescher, D.; Kneipp, J.; Roos, P. H.; Panne, U.; Jakubowski, N., Iodine as an Elemental Marker for Imaging of Single Cells and Tissue Sections by Laser Ablation Inductively Coupled Plasma Mass Spectrometry. *J. Anal. At. Spectrom.* **2011**, *26,* 2160-2165.

372. Giesen, C.; Mairinger, T.; Khoury, L.; Waentig, L.; Jakubowski, N.; Panne, U., Multiplexed Immunohistochemical Detection of Tumor Markers in Breast Cancer Tissue Using Laser Ablation Inductively Coupled Plasma Mass Spectrometry. *Anal. Chem.* **2011**, *83,* 8177-8183.

373. Bang, T. d.; Pedas, P.; Schjoerring, J.; Jensen, P.; Husted, S., Multiplexed Quantification of Plant Thylakoid Proteins on Western Blots Using Lanthanide-Labeled Antibodies and Laser Ablation Inductively Coupled Plasma Mass Spectrometry (LA-ICP-MS). *Anal. Chem.* **2013**, *85,* 5047-5054.

374. Reifschneider, O.; Wehe, C. A.; Diebold, K.; Becker, C.; Sperling, M.; Karst, U., Elemental Bioimaging of Haematoxylin and Eosin-Stained Tissues by Laser Ablation ICP-MS. *J. Anal. At. Spectrom.* **2013**, *28,* 989-993.

375. Hoesl, S.; Neumann, B.; Techritz, S.; Linscheid, M.; Theuring, F.; Scheler, C.; Jakubowski, N.; Mueller, L., Development of a Calibration and Standardization Procedure for LA-ICP-MS Using a Conventional Ink-Jet Printer for Quantification of

Proteins in Electro- and Western-Blot Assays. *J. Anal. At. Spectrom.* **2014**, *29,* 1282-1291.

376. Frick, D. A.; Giesen, C.; Hemmerle, T.; Bodenmiller, B.; Günther, D., An Internal Standardisation Strategy for Quantitative Immunoassay Tissue Imaging Using Laser Ablation Inductively Coupled Plasma Mass Spectrometry. *J. Anal. At. Spectrom.* **2015**, *30,* 254-259.

377. Managh, A. J.; Hutchinson, R. W.; Riquelme, P.; Broichhausen, C.; Wege, A. K.; Ritter, U.; Ahrens, N.; Koehl, G. E.; Walter, L.; Florian, C.; Schlitt, H. J.; Reid, H. J.; Geissler, E. K.; Sharp, B. L.; Hutchinson, J. A., Laser Ablation-Inductively Coupled Plasma Mass Spectrometry: An Emerging Technology for Detecting Rare Cells in Tissue Sections. *J. Immunol.* **2014**, *193,* 2600-2608.

378. Paul, B.; Hare, D. J.; Bishop, D. P.; Paton, C.; Nguyen, V. T.; Cole, N.; Niedwiecki, M. M.; Andreozzi, E.; Vais, A.; Billings, J. L.; Bray, L.; Bush, A. I.; McColl, G.; Roberts, B. R.; Adlard, P. A.; Finkelstein, D. I.; Hellstrom, J.; Hergt, J. M.; Woodhead, J. D.; Doble, P. A., Visualising Mouse Neuroanatomy and Function by Metal Distribution Using Laser Ablation-Inductively Coupled Plasma-Mass Spectrometry Imaging. *Chem. Sci.* **2015**, *6,* 5383-5393.

379. Mueller, L.; Herrmann, A. J.; Techritz, S.; Panne, U.; Jakubowski, N., Quantitative Characterization of Single Cells by Use of Immunocytochemistry Combined with Multiplex LA-ICP-MS. *Anal. Bioanal. Chem.* **2017**, *409,* 3667-3676.

380. Aljakna, A.; Lauer, E.; Lenglet, S.; Grabherr, S.; Fracasso, T.; Augsburger, M.; Sabatasso, S.; Thomas, A., Multiplex Quantitative Imaging of Human Myocardial Infarction by Mass Spectrometry-Immunohistochemistry. *Int. J. Legal Med.* **2018**, *132,* 1675-1684.

381. Cruz-Alonso, M.; Fernandez, B.; Álvarez, L.; González-Iglesias, H.; Traub, H.; Jakubowski, N.; Pereiro, R., Bioimaging of Metallothioneins in Ocular Tissue Sections by Laser Ablation-ICP-MS Using Bioconjugated Gold Nanoclusters as Specific Tags. *Microchim. Acta* **2017**, *185,* 64.

382. Cruz-Alonso, M.; Fernandez, B.; Navarro, A.; Junceda, S.; Astudillo, A.; Pereiro, R., Laser Ablation ICP-MS for Simultaneous Quantitative Imaging of Iron and Ferroportin in Hippocampus of Human Brain Tissues with Alzheimer's Disease. *Talanta* **2019**, *197,* 413-421.

383. Vaneckova, T.; Bezdekova, J.; Tvrdonova, M.; Vlcnovska, M.; Novotna, V.; Neuman, J.; Stossova, A.; Kanicky, V.; Adam, V.; Vaculovicova, M.; Vaculovic, T., Cds Quantum Dots-Based Immunoassay Combined with Particle Imprinted Polymer Technology and Laser Ablation ICP-MS as a Versatile Tool for Protein Detection. *Sci. Rep.* **2019**, *9,* 11840.

384. McInnes, L. E.; Noor, A.; Kysenius, K.; Cullinane, C.; Roselt, P.; McLean, C. A.; Chiu, F. C. K.; Powell, A. K.; Crouch, P. J.; White, J. M.; Donnelly, P. S., Potential Diagnostic Imaging of Alzheimer's Disease with Copper-64 Complexes That Bind to Amyloid-B Plaques. *Inorg. Chem.* **2019**, *58,* 3382-3395.

385. Lores-Padín, A.; Fernández, B.; Álvarez, L.; González-Iglesias, H.; Lengyel, I.; Pereiro, R., Multiplex Bioimaging of Proteins-Related to Neurodegenerative Diseases in Eye Sections by Laser Ablation - Inductively Coupled Plasma – Mass Spectrometry Using Metal Nanoclusters as Labels. *Talanta* **2020**, *221,* 121489.

386. Giesen, C.; Wang, H. A.; Schapiro, D.; Zivanovic, N.; Jacobs, A.; Hattendorf, B.; Schuffler, P. J.; Grolimund, D.; Buhmann, J. M.; Brandt, S.; Varga, Z.; Wild, P. J.;

Gunther, D.; Bodenmiller, B., Highly Multiplexed Imaging of Tumor Tissues with Subcellular Resolution by Mass Cytometry. *Nat Methods* **2014**, *11,* 417-22.

387.   Meyer, F., Topographic Distance and Watershed Lines. *Signal Processing* **1994**, *38,* 113-125.

388.   Schuffler, P. J.; Schapiro, D.; Giesen, C.; Wang, H. A.; Bodenmiller, B.; Buhmann, J. M., Automatic Single Cell Segmentation on Highly Multiplexed Tissue Images. *Cytometry A* **2015**, *87,* 936-42.

389.   Schapiro, D.; Jackson, H. W.; Raghuraman, S.; Fischer, J. R.; Zanotelli, V. R. T.; Schulz, D.; Giesen, C.; Catena, R.; Varga, Z.; Bodenmiller, B., Histocat: Analysis of Cell Phenotypes and Interactions in Multiplex Image Cytometry Data. *Nat Methods* **2017**, *14,* 873-876.

390.   Schulz, D.; Zanotelli, V. R. T.; Fischer, J. R.; Schapiro, D.; Engler, S.; Lun, X. K.; Jackson, H. W.; Bodenmiller, B., Simultaneous Multiplexed Imaging of Mrna and Proteins with Subcellular Resolution in Breast Cancer Tissue Samples by Mass Cytometry. *Cell Syst* **2018**, *6,* 25-36 e5.

391.   Straus, R. N.; Carew, A.; Sandkuijl, D.; Closson, T.; Baranov, V. I.; Loboda, A., Analytical Figures of Merit for a Novel Tissue Imaging System. *J. Anal. At. Spectrom.* **2017**, *32,* 1044-1051.

392.   Hötzel, K. J.; Havnar, C. A.; Ngu, H. V.; Rost, S.; Liu, S. D.; Rangell, L. K.; Peale, F. V., Synthetic Antigen Gels as Practical Controls for Standardized and Quantitative Immunohistochemistry. *J. Histochem. Cytochem.* **2019**, *67,* 309-334.

393.   Zhao, Y.; Uduman, M.; Siu, J. H. Y.; Tull, T. J.; Sanderson, J. D.; Wu, Y. B.; Zhou, J. Q.; Petrov, N.; Ellis, R.; Todd, K.; Chavele, K. M.; Guesdon, W.; Vossenkamper, A.; Jassem, W.; D'Cruz, D. P.; Fear, D. J.; John, S.; Scheel-Toellner, D.; Hopkins, C.; Moreno, E.; Woodman, N. L.; Ciccarelli, F.; Heck, S.; Kleinstein, S. H.; Bemark, M.; Spencer, J., Spatiotemporal Segregation of Human Marginal Zone and Memory B Cell Populations in Lymphoid Tissue. *Nat. Commun.* **2018**, *9,* 3857.

394.   Brahler, S.; Zinselmeyer, B. H.; Raju, S.; Nitschke, M.; Suleiman, H.; Saunders, B. T.; Johnson, M. W.; Bohner, A. M. C.; Viehmann, S. F.; Theisen, D. J.; Kretzer, N. M.; Briseno, C. G.; Zaitsev, K.; Ornatsky, O.; Chang, Q.; Carrero, J. A.; Kopp, J. B.; Artyomov, M. N.; Kurts, C.; Murphy, K. M.; Miner, J. H.; Shaw, A. S., Opposing Roles of Dendritic Cell Subsets in Experimental Gn. *J. Am. Soc. Nephrol.* **2018**, *29,* 138-154.

395.   Durand, M.; Walter, T.; Pirnay, T.; Naessens, T.; Gueguen, P.; Goudot, C.; Lameiras, S.; Chang, Q.; Talaei, N.; Ornatsky, O.; Vassilevskaia, T.; Baulande, S.; Amigorena, S.; Segura, E., Human Lymphoid Organ Cdc2 and Macrophages Play Complementary Roles in T Follicular Helper Responseshuman Cdc2 and Macrophages Induce Tfh Responses. *The Journal of experimental medicine* **2019**, *216,* 1561-1581.

396.   Li, N.; van Unen, V.; Guo, N.; Abdelaal, T.; Somarakis, A.; Eggermont, J.; Mahfouz, A.; Chuva de Sousa Lopes, S. M.; Lelieveldt, B. P. F.; Koning, F., Early-Life Compartmentalization of Immune Cells in Human Fetal Tissues Revealed by High-Dimensional Mass Cytometry. *Front Immunol* **2019**, *10,* 1932.

397.   Damond, N.; Engler, S.; Zanotelli, V. R. T.; Schapiro, D.; Wasserfall, C. H.; Kusmartseva, I.; Nick, H. S.; Thorel, F.; Herrera, P. L.; Atkinson, M. A.; Bodenmiller, B., A Map of Human Type 1 Diabetes Progression by Imaging Mass Cytometry. *Cell Metab.* **2019**, *29,* 755-768 e5.

398.   Park, C.; Ponath, G.; Levine-Ritterman, M.; Bull, E.; Swanson, E. C.; De Jager, P. L.; Segal, B. M.; Pitt, D., The Landscape of Myeloid and Astrocyte Phenotypes in Acute Multiple Sclerosis Lesions. *Acta Neuropathol. Commun.* **2019**, *7*, 130.

399.   Theil, D.; Smith, P.; Huck, C.; Gilbart, Y.; Kakarieka, A.; Leppert, D.; Rauld, C.; Schmid, C.; Baumgartner, R.; Stuber, N.; Cordoba, F.; Dubost, V.; Darribat, K.; Jivkov, M.; Frieauff, W.; Kneuer, R.; Stoeckli, M.; Reinker, S.; Mansfield, K.; Carballido, J. M.; Couttet, P.; Weckbecker, G., Imaging Mass Cytometry and Single-Cell Genomics Reveal Differential Depletion and Repletion of B-Cell Populations Following Ofatumumab Treatment in Cynomolgus Monkeys. *Front Immunol* **2019**, *10*, 1340.

400.   Aoki, T.; Chong, L. C.; Takata, K.; Milne, K.; Hav, M.; Colombo, A.; Chavez, E. A.; Nissen, M.; Wang, X.; Miyata-Takata, T.; Lam, V.; Vigano, E.; Woolcock, B. W.; Telenius, A.; Li, M. Y.; Healy, S.; Ghesquiere, C.; Kos, D.; Goodyear, T.; Veldman, J.; Zhang, A. W.; Kim, J.; Saberi, S.; Ding, J.; Farinha, P.; Weng, A. P.; Savage, K. J.; Scott, D. W.; Krystal, G.; Nelson, B. H.; Mottok, A.; Merchant, A.; Shah, S. P.; Steidl, C., Single-Cell Transcriptome Analysis Reveals Disease-Defining T-Cell Subsets in the Tumor Microenvironment of Classic Hodgkin Lymphoma. *Cancer Discov* **2020**, *10*, 406-421.

401.   Xiang, H.; Ramil, C. P.; Hai, J.; Zhang, C.; Wang, H.; Watkins, A. A.; Afshar, R.; Georgiev, P.; Sze, M. A.; Song, X. S.; Curran, P. J.; Cheng, M.; Miller, J. R.; Sun, D.; Loboda, A.; Jia, Y.; Moy, L. Y.; Chi, A.; Brandish, P. E., Cancer-Associated Fibroblasts Promote Immunosuppression by Inducing Ros-Generating Monocytic Mdscs in Lung Squamous Cell Carcinoma. *Cancer Immunol Res* **2020**, *8*, 436-450.

402.   Batth, I. S.; Meng, Q.; Wang, Q.; Torres, K. E.; Burks, J.; Wang, J.; Gorlick, R.; Li, S., Rare Osteosarcoma Cell Subpopulation Protein Array and Profiling Using Imaging Mass Cytometry and Bioinformatics Analysis. *BMC Cancer* **2020**, *20*, 715.

403.   Ali, H. R.; Jackson, H. W.; Zanotelli, V. R. T.; Danenberg, E.; Fischer, J. R.; Bardwell, H.; Provenzano, E.; Rueda, O. M.; Chin, S.-F.; Aparicio, S.; Caldas, C.; Bodenmiller, B., Imaging Mass Cytometry and Multiplatform Genomics Define the Phenogenomic Landscape of Breast Cancer. *Nature Cancer* **2020**, *1*, 163-175.

404.   Jackson, H. W.; Fischer, J. R.; Zanotelli, V. R. T.; Ali, H. R.; Mechera, R.; Soysal, S. D.; Moch, H.; Muenst, S.; Varga, Z.; Weber, W. P.; Bodenmiller, B., The Single-Cell Pathology Landscape of Breast Cancer. *Nature* **2020**, *578*, 615-620.

405.   Guo, N.; van Unen, V.; Ijsselsteijn, M. E.; Ouboter, L. F.; van der Meulen, A. E.; Chuva de Sousa Lopes, S. M.; de Miranda, N.; Koning, F.; Li, N., A 34-Marker Panel for Imaging Mass Cytometric Analysis of Human Snap-Frozen Tissue. *Front Immunol* **2020**, *11*, 1466.

406.   Flint, L. E.; Hamm, G.; Ready, J. D.; Ling, S.; Duckett, C. J.; Cross, N. A.; Cole, L. M.; Smith, D. P.; Goodwin, R. J. A.; Clench, M. R., Characterization of an Aggregated Three-Dimensional Cell Culture Model by Multimodal Mass Spectrometry Imaging. *Anal. Chem.* **2020**, *92*, 12538-12547.

407.   Bouzekri, A.; Esch, A.; Ornatsky, O., Multidimensional Profiling of Drug-Treated Cells by Imaging Mass Cytometry. *FEBS Open Bio* **2019**, *9*, 1652-1669.

408.   Carvajal-Hausdorf, D. E.; Patsenker, J.; Stanton, K. P.; Villarroel-Espindola, F.; Esch, A.; Montgomery, R. R.; Psyrri, A.; Kalogeras, K. T.; Kotoula, V.; Foutzilas, G.; Schalper, K. A.; Kluger, Y.; Rimm, D. L., Multiplexed Measurement of Signaling Targets and Cytotoxic T Cells in Trastuzumab-Treated Patients Using Imaging Mass Cytometry. *Clin. Cancer Res.* **2019**, *25*, 3054-3062.

145

409. Bassan, J.; Willis, L. M.; Vellanki, R. N.; Nguyen, A.; Edgar, L. J.; Wouters, B. G.; Nitz, M., Tephe, a Tellurium-Containing Phenylalanine Mimic, Allows Monitoring of Protein Synthesis in Vivo with Mass Cytometry. *Proc. Natl. Acad. Sci.* **2019**, *116,* 8155-8160.

410. Bassan, J.; Nitz, M., Methods for Analyzing Tellurium Imaging Mass Cytometry Data. *PLoS One* **2019**, *14,* e0221714.

411. Rana, R.; Gomez-Biagi, R. F.; Bassan, J.; Nitz, M., Signal Amplification for Imaging Mass Cytometry. *Bioconjug. Chem.* **2019**, *30,* 2805-2810.

412. Yu, Y.; Dang, J.; Liu, X.; Wang, L.; Li, S.; Zhang, T.; Ding, X., Metal-Labeled Aptamers as Novel Nanoprobes for Imaging Mass Cytometry Analysis. *Anal. Chem.* **2020**, *92,* 6312-6320.

413. Singh, N.; Avigan, Z. M.; Kliegel, J. A.; Shuch, B. M.; Montgomery, R. R.; Moeckel, G. W.; Cantley, L. G., Development of a 2-Dimensional Atlas of the Human Kidney with Imaging Mass Cytometry. *JCI Insight* **2019**, *4,* e129477.

414. Warren, C.; McDonald, D.; Capaldi, R.; Deehan, D.; Taylor, R. W.; Filby, A.; Turnbull, D. M.; Lawless, C.; Vincent, A. E., Decoding Mitochondrial Heterogeneity in Single Muscle Fibres by Imaging Mass Cytometry. *Sci. Rep.* **2020**, *10,* 15336.

415. Weiskirchen, R.; Weiskirchen, S.; Kim, P.; Winkler, R., Software Solutions for Evaluation and Visualization of Laser Ablation Inductively Coupled Plasma Mass Spectrometry Imaging (LA-ICP-MSi) Data: A Short Overview. *J. Cheminform.* **2019**, *11,* 16.

416. Lein, E. S.; Hawrylycz, M. J.; Ao, N.; Ayres, M.; Bensinger, A.; Bernard, A.; Boe, A. F.; Boguski, M. S.; Brockway, K. S.; Byrnes, E. J.; Chen, L.; Chen, L.; Chen, T. M.; Chin, M. C.; Chong, J.; Crook, B. E.; Czaplinska, A.; Dang, C. N.; Datta, S.; Dee, N. R.; Desaki, A. L.; Desta, T.; Diep, E.; Dolbeare, T. A.; Donelan, M. J.; Dong, H. W.; Dougherty, J. G.; Duncan, B. J.; Ebbert, A. J.; Eichele, G.; Estin, L. K.; Faber, C.; Facer, B. A.; Fields, R.; Fischer, S. R.; Fliss, T. P.; Frensley, C.; Gates, S. N.; Glattfelder, K. J.; Halverson, K. R.; Hart, M. R.; Hohmann, J. G.; Howell, M. P.; Jeung, D. P.; Johnson, R. A.; Karr, P. T.; Kawal, R.; Kidney, J. M.; Knapik, R. H.; Kuan, C. L.; Lake, J. H.; Laramee, A. R.; Larsen, K. D.; Lau, C.; Lemon, T. A.; Liang, A. J.; Liu, Y.; Luong, L. T.; Michaels, J.; Morgan, J. J.; Morgan, R. J.; Mortrud, M. T.; Mosqueda, N. F.; Ng, L. L.; Ng, R.; Orta, G. J.; Overly, C. C.; Pak, T. H.; Parry, S. E.; Pathak, S. D.; Pearson, O. C.; Puchalski, R. B.; Riley, Z. L.; Rockett, H. R.; Rowland, S. A.; Royall, J. J.; Ruiz, M. J.; Sarno, N. R.; Schaffnit, K.; Shapovalova, N. V.; Sivisay, T.; Slaughterbeck, C. R.; Smith, S. C.; Smith, K. A.; Smith, B. I.; Sodt, A. J.; Stewart, N. N.; Stumpf, K. R.; Sunkin, S. M.; Sutram, M.; Tam, A.; Teemer, C. D.; Thaller, C.; Thompson, C. L.; Varnam, L. R.; Visel, A.; Whitlock, R. M.; Wohnoutka, P. E.; Wolkey, C. K.; Wong, V. Y.; Wood, M.; Yaylaoglu, M. B.; Young, R. C.; Youngstrom, B. L.; Yuan, X. F.; Zhang, B.; Zwingman, T. A.; Jones, A. R., Genome-Wide Atlas of Gene Expression in the Adult Mouse Brain. *Nature* **2007**, *445,* 168-176.

417. Hare, D. J.; Lee, J. K.; Beavis, A. D.; van Gramberg, A.; George, J.; Adlard, P. A.; Finkelstein, D. I.; Doble, P. A., Three-Dimensional Atlas of Iron, Copper, and Zinc in the Mouse Cerebrum and Brainstem. *Anal. Chem.* **2012**, *84,* 3990-3997.

418. Bala, A.; Sharma, A. K., Image Segmentation: Automatic Cluster Number Generation in K-Means. *2019 Fifth International Conference on Image Information Processing (ICIIP)* **2019**, *00,* 199-204.

419. Kundu, A., Local Segmentation of Biomedical Images. *Comput. Med. Imaging Graph.* **1990**, *14,* 173-83.

420. Verveer, P. J.; Squire, A.; Bastiaens, P. I., Global Analysis of Fluorescence Lifetime Imaging Microscopy Data. *Biophys. J.* **2000**, *78,* 2127-2137.

421. Oros-Peusquens, A. M.; Matusch, A.; Becker, J. S.; Shah, N. J., Automatic Segmentation of Tissue Sections Using the Multielement Information Provided by LA-ICP-MS Imaging and K-Means Cluster Analysis. *Int. J. Mass Spectrom.* **2011**, *307,* 245-252.

422. Bishop, D. P.; Westerhausen, M. T.; Barthelemy, F.; Lockwood, T.; Cole, N.; Gibbs, E. M.; Crosbie, R. H.; Nelson, S. F.; Miceli, M. C.; Doble, P. A.; Wanagat, J., Quantitative Immuno-Mass Spectrometry Imaging of Skeletal Muscle Dystrophin. *Sci. Rep.* **2021**, *11,* 1128.

423. Sauvola, J.; Pietikäinen, M., Adaptive Document Image Binarization. *Pattern Recogn.* **2000**, *33,* 225-236.

424. Phansalkar, N.; More, S.; Sabale, A.; Joshi, M., Adaptive Local Thresholding for Detection of Nuclei in Diversity Stained Cytology Images. *2011 International Conference on Communications and Signal Processing* **2011**, *1,* 218-220.

425. Otsu, N., A Threshold Selection Method from Gray-Level Histograms. *IEEE Transactions on Systems, Man, and Cybernetics* **1979**, *9,* 62-66.

426. Paton, C.; Hellstrom, J.; Paul, B.; Woodhead, J.; Hergt, J., Iolite: Freeware for the Visualisation and Processing of Mass Spectrometric Data. *J. Anal. At. Spectrom.* **2011**, *26,* 2508-2518.

427. Westerhausen, M. T.; Bishop, D. P.; Dowd, A.; Wanagat, J.; Cole, N.; Doble, P. A., Super-Resolution Reconstruction for Two- and Three-Dimensional LA-ICP-MS Bioimaging. *Anal. Chem.* **2019**, *91,* 14879-14886.

428. Hare, D. J.; New, E. J.; de Jonge, M. D.; McColl, G., Imaging Metals in Biology: Balancing Sensitivity, Selectivity and Spatial Resolution. *Chem. Soc. Rev.* **2015**, *44,* 5941-5958.

429. Wagner, B.; Kępa, L.; Donten, M.; Wrzosek, B.; Żukowska, G. Z.; Lewandowska, A., Laser Ablation Inductively Coupled Plasma Mass Spectrometry Appointed to Subserve Pigment Identification. *Microchem. J.* **2019**, *146,* 279-285.

430. Balbekova, A.; Lohninger, H.; van Tilborg, G. A. F.; Dijkhuizen, R. M.; Bonta, M.; Limbeck, A.; Lendl, B.; Al-Saad, K. A.; Ali, M.; Celikic, M.; Ofner, J., Fourier Transform Infrared (FT-IR) and Laser Ablation Inductively Coupled Plasma-Mass Spectrometry (LA-ICP-MS) Imaging of Cerebral Ischemia: Combined Analysis of Rat Brain Thin Cuts toward Improved Tissue Classification. *Appl. Spectrosc.* **2018**, *72,* 241-250.

431. Wu, M.; Shu, J., Multimodal Molecular Imaging: Current Status and Future Directions. *Contrast Media Mol Imaging* **2018**, *2018,* 1382183.

432. Bulk, M.; Abdelmoula, W. M.; Geut, H.; Wiarda, W.; Ronen, I.; Dijkstra, J.; van der Weerd, L., Quantitative MRI and Laser Ablation-Inductively Coupled Plasma-Mass Spectrometry Imaging of Iron in the Frontal Cortex of Healthy Controls and Alzheimer's Disease Patients. *Neuroimage* **2020**, *215,* 116808.

433. Marillo-Sialer, E.; Black, J. R.; Paul, B.; Kysenius, K.; Crouch, P. J.; Hergt, J. M.; Woodhead, J. D.; Hare, D. J., Construction of 3d Native Elemental Maps for Large Biological Specimens Using LA-ICP-MS Coupled with X-Ray Tomography. *J. Anal. At. Spectrom.* **2020**, *35,* 671-678.

434. Malderen, S. J. V.; Laforce, B.; Acker, T. V.; Nys, C.; Rijcke, M. D.; Rycke, R. d.; Bruyne, M. D.; Boone, M. N.; Schamphelaere, K. D.; Borovinskaya, O.; Samber, B. D.; Vincze, L.; Vanhaecke, F., Three-Dimensional Reconstruction of the Tissue-Specific Multielemental Distribution within Ceriodaphnia Dubia Via Multimodal Registration

Using Laser Ablation Icp-Mass Spectrometry and X-Ray Spectroscopic Techniques. *Anal. Chem.* **2017**, *89,* 4161-4168.

435. Kevadiya, B. D.; Ottemann, B.; Mukadam, I. Z.; Castellanos, L.; Sikora, K.; Hilaire, J. R.; Machhi, J.; Herskovitz, J.; Soni, D.; Hasan, M.; Zhang, W.; Anandakumar, S.; Garrison, J.; McMillan, J.; Edagwa, B.; Mosley, R. L.; Vachet, R. W.; Gendelman, H. E., Rod-Shape Theranostic Nanoparticles Facilitate Antiretroviral Drug Biodistribution and Activity in Human Immunodeficiency Virus Susceptible Cells and Tissues. *Theranostics* **2020**, *10,* 630-656.

436. Mangarova, D. B.; Brangsch, J.; Mohtashamdolatshahi, A.; Kosch, O.; Paysen, H.; Wiekhorst, F.; Klopfleisch, R.; Buchholz, R.; Karst, U.; Taupitz, M.; Schnorr, J.; Hamm, B.; Makowski, M. R., Ex Vivo Magnetic Particle Imaging of Vascular Inflammation in Abdominal Aortic Aneurysm in a Murine Model. *Sci. Rep.* **2020**, *10,* 12410.

437. Spengler, B.; Hubert, M.; Kaufmann, R. 42nd Annual Conference on Mass Spectrometry and Allied Topics, Lennon, J. J.; Brown, R. S., Eds. ASMS: 1994.

438. Caprioli, R. M.; Farmer, T. B.; Gile, J., Molecular Imaging of Biological Samples: Localization of Peptides and Proteins Using Maldi-Tof Ms. *Anal. Chem.* **1997**, *69,* 4751-4760.

439. Kriegsmann, J.; Kriegsmann, M.; Casadonte, R., Maldi Tof Imaging Mass Spectrometry in Clinical Pathology: A Valuable Tool for Cancer Diagnostics (Review). *Int. J. Oncol.* **2015**, *46,* 893-906.

440. Van de Plas, R.; Yang, J.; Spraggins, J.; Caprioli, R. M., Image Fusion of Mass Spectrometry and Microscopy: A Multimodality Paradigm for Molecular Tissue Mapping. *Nat Methods* **2015**, *12,* 366-372.

441. Angel, P. M.; Baldwin, H. S.; Gottlieb Sen, D.; Su, Y. R.; Mayer, J. E.; Bichell, D.; Drake, R. R., Advances in Maldi Imaging Mass Spectrometry of Proteins in Cardiac Tissue, Including the Heart Valve. *Biochim Biophys Acta Proteins Proteom* **2017**, *1865,* 927-935.

442. Stoeckli, M.; Chaurand, P.; Hallahan, D. E.; Caprioli, R. M., Imaging Mass Spectrometry: A New Technology for the Analysis of Protein Expression in Mammalian Tissues. *Nat Med* **2001**, *7,* 493-496.

443. Garikapati, V.; Karnati, S.; Bhandari, D. R.; Baumgart-Vogt, E.; Spengler, B., High-Resolution Atmospheric-Pressure Maldi Mass Spectrometry Imaging Workflow for Lipidomic Analysis of Late Fetal Mouse Lungs. *Sci. Rep.* **2019**, *9,* 3192.

444. Hart, P. J.; Clench, M. R., Imaging Mass Spectrometry, Methods and Protocols. *Methods in molecular biology (Clifton, N.J.)* **2017**, *1618,* 29-36.

445. Norris, J. L.; Caprioli, R. M., Analysis of Tissue Specimens by Matrix-Assisted Laser Desorption/Ionization Imaging Mass Spectrometry in Biological and Clinical Research. *Chem. Rev.* **2013**, *113,* 2309-2342.

446. Tang, W.; Chen, J.; Zhou, J.; Ge, J.; Zhang, Y.; Li, P.; Li, B., Quantitative Maldi Imaging of Spatial Distributions and Dynamic Changes of Tetrandrine in Multiple Organs of Rats. *Theranostics* **2019**, *9,* 932-944.

447. Mittal, P.; Price, Z. K.; Lokman, N. A.; Ricciardelli, C.; Oehler, M. K.; Klingler-Hoffmann, M.; Hoffmann, P., Matrix Assisted Laser Desorption/Ionization Mass Spectrometry Imaging (Maldi Msi) for Monitoring of Drug Response in Primary Cancer Spheroids. *Proteomics* **2019**, *19,* e1900146.

448. Machalkova, M.; Pavlatovska, B.; Michalek, J.; Pruska, A.; Stepka, K.; Necasova, T.; Radaszkiewicz, K. A.; Kozubek, M.; Smarda, J.; Preisler, J.; Navratilova, J., Drug

Penetration Analysis in 3d Cell Cultures Using Fiducial-Based Semiautomatic Coregistration of Maldi Msi and Immunofluorescence Images. *Anal. Chem.* **2019**, *91,* 13475-13484.

449. Leopold, J.; Popkova, Y.; Engel, K. M.; Schiller, J., Recent Developments of Useful Maldi Matrices for the Mass Spectrometric Characterization of Lipids. *Biomol* **2018**, *8,* 173.

450. de Vega, R. G.; Sanchez, M. L. F.; Eiro, N.; Vizoso, F. J.; Sperling, M.; Karst, U.; Medel, A. S., Multimodal Laser Ablation/Desorption Imaging Analysis of Zn and Mmp-11 in Breast Tissues. *Anal. Bioanal. Chem.* **2018**, *410,* 913-922.

451. Holzlechner, M.; Bonta, M.; Lohninger, H.; Limbeck, A.; Marchetti-Deschmann, M., Multi-Sensor Imaging - from Sample Preparation to Integrated Multimodal Interpretation of LA-ICP-MS and Maldi Ms Imaging Data. *Anal. Chem.* **2018**, *90,* 8831-8837.

452. Lohofer, F.; Buchholz, R.; Glinzer, A.; Huber, K.; Haas, H.; Kaissis, G.; Feuchtinger, A.; Aichler, M.; Sporns, P. B.; Holtke, C.; Stolting, M.; Schilling, F.; Botnar, R. M.; Kimm, M. A.; Faber, C.; Walch, A. K.; Zernecke, A.; Karst, U.; Wildgruber, M., Mass Spectrometry Imaging of Atherosclerosis-Affine Gadofluorine Following Magnetic Resonance Imaging. *Sci. Rep.* **2020**, *10,* 79.

453. Liebl, H., Ion Microprobe Mass Analyzer. *J. Appl. Phys.* **1967**, *38,* 5277-5283.

454. Benninghoven, A., Untersuchungen Zum Spektrum Und Den Anfangsenergien Negativer Sekundärionen. *Zeitschrift für Physik* **1967**, *199,* 141-156.

455. Benninghoven, A., Die Analyse Monomolekularer Festkörperoberflächenschichten Mit Hilfe Der Sekundärionenemission. *Zeitschrift für Physik A Hadrons and nuclei* **1970**, *230,* 403-417.

456. Benninghoven, A., Static Sims Applications—from Silicon Single Crystal Oxidation to DNA Sequencing. *Journal of Vacuum Science & Technology A: Vacuum, Surfaces, and Films* **1985**, *3,* 451-460.

457. Vickerman, J. C., Secondary Ion Mass Spectrometry-Basic Concepts, Instrumental Aspects, Applications and Trends. A. Benninghoven, F. G. Rudenauer and H. W. Werner, Wiley, New York, 1987, 1277 Pages. *Surf. Interface Anal.* **1987**, *10,* 435-435.

458. Boxer, S. G.; Kraft, M. L.; Weber, P. K., Advances in Imaging Secondary Ion Mass Spectrometry for Biological Samples. *Annu Rev Biophys* **2009**, *38,* 53-74.

459. Schaltegger, U.; Schmitt, A. K.; Horstwood, M. S. A., U–Th–Pb Zircon Geochronology by ID-TIMS, SIMS, and Laser Ablation ICP-MS: Recipes, Interpretations, and Opportunities. *Chem. Geol.* **2015**, *402,* 89-110.

460. Legin, A. A.; Theiner, S.; Schintlmeister, A.; Reipert, S.; Heffeter, P.; Jakupec, M. A.; Mayr, J.; Varbanov, H. P.; Kowol, C. R.; Galanski, M.; Berger, W.; Wagner, M.; Keppler, B. K., Multi-Scale Imaging of Anticancer Platinum(Iv) Compounds in Murine Tumor and Kidney. *Chem. Sci.* **2016**, *7,* 3052-3061.

461. Ackerman, C. M.; Weber, P. K.; Xiao, T.; Thai, B.; Kuo, T. J.; Zhang, E.; Pett-Ridge, J.; Chang, C. J., Multimodal LA-ICP-MS and Nanosims Imaging Enables Copper Mapping within Photoreceptor Megamitochondria in a Zebrafish Model of Menkes Disease. *Metallomics* **2018**, *10,* 474-485.

462. Jolivet, L.; Leprince, M.; Moncayo, S.; Sorbier, L.; Lienemann, C. P.; Motto-Ros, V., Review of the Recent Advances and Applications of Libs-Based Imaging. *Spectrochim. Acta Part B At. Spectrosc.* **2019**, *151,* 41-53.

463. de Oliveira, A. P.; de Oliveira Leme, F.; Nomura, C. S.; Naozuka, J., Elemental Imaging by Laser-Induced Breakdown Spectroscopy to Evaluate Selenium Enrichment Effects in Edible Mushrooms. *Sci. Rep.* **2019**, *9,* 10827.

464. Chirinos, J. R.; Oropeza, D. D.; Gonzalez, J. J.; Hou, H.; Morey, M.; Zorba, V.; Russo, R. E., Simultaneous 3-Dimensional Elemental Imaging with Libs and LA-ICP-MS. *J. Anal. At. Spectrom.* **2014**, *29,* 1292-1298.

465. Bonta, M.; Gonzalez, J. J.; Quarles, C. D.; Russo, R. E.; Hegedus, B.; Limbeck, A., Elemental Mapping of Biological Samples by the Combined Use of Libs and LA-ICP-MS. *J. Anal. At. Spectrom.* **2016**, *31,* 252-258.

466. Carvalho, M. L.; Magalhães, T.; Becker, M.; von Bohlen, A., Trace Elements in Human Cancerous and Healthy Tissues: A Comparative Study by Edxrf, Txrf, Synchrotron Radiation and Pixe. *Spectrochim. Acta Part B At. Spectrosc.* **2007**, *62,* 1004-1011.

467. Wang, H.-J.; Wang, M.; Wang, B.; Meng, X.-Y.; Wang, Y.; Li, M.; Feng, W.-Y.; Zhao, Y.-L.; Chai, Z.-F., Quantitative Imaging of Element Spatial Distribution in the Brain Section of a Mouse Model of Alzheimer's Disease Using Synchrotron Radiation X-Ray Fluorescence Analysis. *J. Anal. At. Spectrom.* **2010**, *25,* 328-333.

468. Blaske, F.; Reifschneider, O.; Gosheger, G.; Wehe, C. A.; Sperling, M.; Karst, U.; Hauschild, G.; Höll, S., Elemental Bioimaging of Nanosilver-Coated Prostheses Using X-Ray Fluorescence Spectroscopy and Laser Ablation-Inductively Coupled Plasma-Mass Spectrometry. *Anal. Chem.* **2013**, *86,* 615-620.

469. Norris, C. A.; Danyushevsky, L.; Olin, P.; West, N. R., Elimination of Aliasing in LA-ICP-MS by Alignment of Laser and Mass Spectrometer. *J. Anal. At. Spectrom.* **2021**, *4,* 733-739.